MEASUREMENT OF ABSORBED DOSE TO WATER FOR MEDIUM ENERGY X-RAYS.

A Thesis submitted to the University of London
for the Degree of
Doctor of Philosophy.

by

Karen Elizabeth Rosser

University College London
University of London.

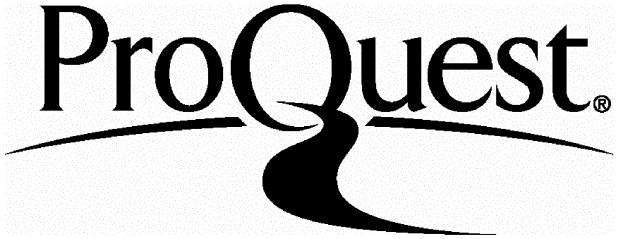

This thesis is dedicated to

my family,

especially my husband G. Christaki

and

my father T.A Rosser

ABSTRACT

The aim of this thesis is to determine the factors required to convert the air kerma measured using an ionization chamber to absorbed dose to water when irradiated with medium energy X-rays. This principally involved the determination of the ratio of the mass energy absorption coefficients of water to air and the chamber correction factor for an NE2561 ionization chamber.

The ratio of mass energy absorption coefficients of water to air was calculated by averaging the monoenergetic values over the photon fluence spectrum at 2 cm deep in water. The photon fluence spectrum was calculated using the EGS4 Monte Carlo code based on measured spectra in air.

The chamber correction factor for a NE2561 chamber was determined using two methods. First the absorbed dose to water was measured using a NE2561 chamber and compared with that using a NE2571 chamber. The chamber correction factor varied from (1.022 ± 0.03) to (1.016 ± 0.01) for HVL between 0.15 and 4 mmCu. Secondly the air kerma in water was measured using the NE2561 chamber and compared with the absorbed dose to water determined using a calorimeter. Initial measurements revealed that the water calorimeter was too insensitive when using medium energy X-rays. An ice calorimeter was built to overcome this problem.

The validity of the absorbed dose to water measured using the ice calorimeter was checked by comparison with the primary standard graphite calorimeter irradiated with ^{60}Co gamma rays. The resultant calibration factor for a NE2561 chamber determined using the ice calorimeter was less than that using the graphite calorimeter by (1.8 ± 0.08)%. The ice calorimeter was then used to determine the chamber correction factor for the NE2561 chamber when irradiated with X-rays generated at 134 kV. The chamber correction factor was (0.98 ± 0.05).

ACKNOWLEDGEMENT

The whole is more than the sum of the parts.

Aristotle.

I would like to thank my supervisors throughout this project Dr B Planskoy and B. Owen for their help, insight and inspiration. I wish them both a long and happy retirement. I would also like to thank Dr S Duane who was my supervisor at NPL after B. Owen retired.

I am indebted to all of the members of the dosimetry branch at NPL for giving me the opportunity to carry out this project. In particular Dr J Hunt the head of the dosimetry branch at NPL for allowing me to do the work for this thesis at NPL. J. Heaton for maintaining the medium energy X-ray facility. D. Crossley and K. Rajendran for advising in the use of Fricke solution, providing triple distilled water and clean glassware. Dr P. Sharpe for his advice in calculating the heat defect in water. M McEwen for advice on calibrating thermistors. I Stoker for helping with the AC wheatstone bridge. Dr D. Burns for giving useful comments on the manuscript of this thesis. The glassblower at the Laboratory of the Government Chemist, F. Gargini.

CONTENTS

CHAPTER 1 INTRODUCTION. 11

1.1 OUTLINE OF THE THESIS 11

CHAPTER 2 MEASUREMENT OF ABSORBED DOSE WATER USING MEDIUM ENERGY X-RAYS. 14

2.1 DETERMINATION OF ABSORBED DOSE TO WATER USING IAEA TRS 277. 14

2.2 COMPARISON OF THE MEASUREMENT OF ABSORBED DOSE TO WATER DETERMINED USING IAEA TRS 277 TO THAT USING ICRU REPORT 23. 15

2.2.1 THE ENERGY REQUIRED TO PRODUCE AN ION PAIR IN AIR. 15

2.2.2 THE RATIO OF MASS ENERGY ABSORPTION COEFFICIENT OF WATER TO AIR. 15

2.2.3 PERTURBATION CORRECTION. 17

2.3 LITERATURE SEARCH TO DETERMINE THE VALUE OF THE CHAMBER CORRECTION FACTOR. 18

2.3.1 DETERMINATION OF THE CHAMBER CORRECTION FACTOR USING THE INDIVIDUAL COMPONENT METHOD 18

2.3.1.1 REPLACEMENT CORRECTION. 18

2.3.1.2 REMAINING COMPONENTS OF THE CHAMBER CORRECTION FACTOR. 21

2.3.2 DETERMINATION OF THE CHAMBER CORRECTION FACTOR BASED ON A DIRECT METHOD OF DETERMINING ABSORBED DOSE TO WATER 21

2.3.3 DETERMINATION OF THE CHAMBER CORRECTION FACTOR USING MEASUREMENT AND CALCULATIONS. 21

2.4 DISCUSSION. 23

CHAPTER 3 DETERMINATION OF ABSORBED DOSE TO WATER USING AN IONIZATION CHAMBER. 24

3.1 INTRODUCTION. 24

3.2 SUITABLE IONIZATION CHAMBERS TO MEASURE ABSORBED DOSE TO WATER USING MEDIUM ENERGY X-RAYS. 24

3.2.1 METHOD 25

3.2.2 DISCUSSION 28

3.3 DETERMINATION OF ABSORBED DOSE TO WATER USING A SUITABLE IONIZATION CHAMBER 29

3.3.1 THE READING OF AN IONIZATION CHAMBER (M). . . 30

3.3.2 MEASUREMENT OF AIR KERMA USING A PRIMARY STANDARD FREE AIR CHAMBER 30

3.4 ESTIMATION OF THE CHAMBER CORRECTION FACTOR FOR A NE2571 IONIZATION CHAMBER 33

3.5 COMPARISON OF THE CHAMBER CORRECTION FACTOR FOR A NE2561 CHAMBER WITH THAT FOR A NE2571 CHAMBER. 33

3.5.1 METHOD 33

3.5.2 DISCUSSION 35

3.5.3 ESTIMATION OF THE CHAMBER CORRECTION FACTOR FOR A NE2561 IONIZATION CHAMBER 36

3.6 DETERMINATION OF THE COMPONENTS OF THE CHAMBER CORRECTION FACTOR FOR A NE2561 IONIZATION CHAMBER. 38

3.6.1 STEM CORRECTION FOR A NE2561 IONIZATION CHAMBER 38

3.6.1.1 METHOD 39

3.6.1.2 DISCUSSION 39

3.6.2 EFFECTS OF WATERPROOF SLEEVES. 41

3.6.2.1 METHOD 41

3.6.2.2 DISCUSSION 43

3.6.3 REPLACEMENT CORRECTION. 43

3.6.4 SUMMARY OF THE COMPONENTS OF THE

CHAMBER CORRECTION FACTOR FOR A NE2561 CHAMBER 45

CHAPTER 4 INVESTIGATION OF THE RATIO OF MASS ENERGY ABSORPTION COEFFICIENTS OF WATER TO AIR AND THE DETERMINATION OF A BEAM QUALITY INDEX FOR MEDIUM ENERGY X-RAYS. 47

4.1 INTRODUCTION. 47

4.2 METHOD OF DETERMINING THE RATIO OF MASS ENERGY ABSORPTION COEFFICIENTS OF WATER TO AIR. 50

4.2.1 DETERMINATION OF THE PHOTON FLUENCE SPECTRUM AT A DEPTH IN WATER 50

4.2.1.1 MEASUREMENT OF THE IN AIR SPECTRA FOR THE NPL THERAPY LEVEL MEDIUM ENERGY QUALITIES 50

4.2.1.2 STRIPPING PROCEDURE 52

4.2.2 COMPARISON OF THE MEASURED SPECTRA WITH THAT PROPOSED BY BIRCH AND MARSHALL 53

4.2.2.1 DISCUSSION 57

4.2.3 DETERMINATION OF THE SPECTRA AT A DEPTH IN WATER 57

4.2.3.1 RESULTS 59

4.2.3.2 UNCERTAINTY FOR $(\mu_{en}/\rho)_{w,a}$ 59

4.2.3.3 DISCUSSION 59

4.3 CALCULATION OF A DEPTH DOSE CURVE IN WATER 60

4.3.1 DISCUSSION 62

4.4 BEAM QUALITY INDEX FOR MEDIUM ENERGY X-RAYS. 62

4.4.1 A BEAM QUALITY INDEX FOR MEDIUM ENERGY X-RAYS 64

4.4.1.1 DETERMINATION OF A QUALITY INDEX FOR MEDIUM ENERGY X-RAYS 66

4.4.1.2 CALCULATION OF THE PHOTON FLUENCE SPECTRUM AT A DEPTH IN WATER 67

4.4.1.3 DISCUSSION 70
CHAPTER 5 WATER CALORIMETRY. 71
5.1 INTRODUCTION. 71
5.1.1 BASIC PRINCIPLES OF WATER CALORIMETRY. 71
5.1.2 DESIGN OF WATER CALORIMETERS. 74
5.1.2.1 INTRODUCTION. 74
5.1.2.2 HEAT FLOW IN A WATER CALORIMETER. 75
5.1.3.3 CONVECTION IN A WATER CALORIMETER. ... 76
5.2 HEAT DEFECT FOR A WATER CALORIMETER 77
5.2.1 INTRODUCTION. 77
5.2.2 REVIEW OF THE LITERATURE. 79
5.2.3 CALCULATION OF THE HEAT DEFECT 81
5.2.3.1 RADIOLYSIS OF WATER 81
5.2.4 CALCULATION OF THE HEAT DEFECT 82
5.2.5 COMPARISON WITH KLASSEN AND ROSS ET AL 82
5.2.6 HEAT DEFECT FOR MEDIUM ENERGY X-RAYS 83
5.3 DESIGN OF THE WATER CALORIMETER USED IN THIS THESIS. 86
5.4 INTRODUCTION TO THERMISTORS. 88
5.4.1 MEASUREMENT OF TEMPERATURE USING A THERMISTOR CONNECTED TO A WHEATSTONE BRIDGE. 90
5.4.2 CALIBRATION OF THE THERMISTOR USED IN THE WATER CALORIMETER 90
5.5 INITIAL MEASUREMENTS USING A WATER CALORIMETER 91
CHAPTER 6 MEASUREMENT OF ABSORBED DOSE TO WATER USING AN ICE CALORIMETER. 93
6.1 INTRODUCTION. 93
6.1.1 COMPARISON OF WATER AND ICE CALORIMETRY. . 93
6.1.1.1 ADVANTAGES OF ICE CALORIMETRY. 93
6.1.1.1.1 TEMPERATURE RISE. 93

6.1.1.1.2 THE EFFECTS OF MATERIALS IN CONTACT WITH WATER. 94
6.1.1.2 DISADVANTAGES OF ICE CALORIMETRY 95
6.1.1.2.1 PHASE BEHAVIOUR IN ICE 95
6.1.1.2.2 THERMAL DIFFUSIVITY OF ICE. . . 95
6.1.1.2.3 HEAT DEFECT. 95
6.2. MEASUREMENTS OF THE ABSORBED DOSE TO WATER USING AN ICE CALORIMETER. 97
6.2.1 CONSTRUCTION OF THE ICE CALORIMETER. 97
6.2.2 MEASURING ELECTRONICS. 97
6.2.2.1 CIRCUIT SHIELDING. 99
6.3 EFFECTS OF FILM ON THE PURITY OF WATER 100
6.4 MEASUREMENT OF THE TEMPERATURE RISE USING A THERMISTOR. 101
6.4.1 CALIBRATION OF A PLATINUM RESISTANCE THERMOMETER. 101
6.4.2 CALIBRATION OF THERMISTORS. 101
6.5 COMPARISON OF THE ABSORBED DOSE TO WATER MEASURED USING THE ICE CALORIMETER TO THAT USING THE PRIMARY STANDARD GRAPHITE CALORIMETER USING ^{60}CO GAMMA RAYS. 102
6.5.1 IRRADIATION OF THE ICE CALORIMETER. 102
6.5.2 IRRADIATION OF A NE2561 IONIZATION CHAMBER 104
6.5.3 CALIBRATION OF A NE2561 IONIZATION CHAMBER BY DIRECT COMPARISON WITH THE PRIMARY STANDARD GRAPHITE CALORIMETER IN ^{60}Co 104
6.5.4 RESULTS 105
6.5.5 UNCERTAINTIES 108
6.6 DETERMINATION OF THE CHAMBER CORRECTION FACTOR FOR A NE2561 IONIZATION CHAMBER IRRADIATED WITH X-RAYS GENERATED AT 134 KV 109

6.6.1 IRRADIATION OF THE ICE CALORIMETER. 109
6.6.2 ABSORBED DOSE TO WATER MEASURED USING AN IONIZATION CHAMBER. 109
6.6.3 RESULTS 111
6.6.4 UNCERTAINTIES 112
CHAPTER 7 CONCLUSIONS 113
7.1 FUTURE WORK 114
8. REFERENCES. 116
APPENDIX 1 MEDIUM ENERGY X-RAY QUALITIES AT NPL. 127
APPENDIX 2 PHYSICS OF MEDIUM ENERGY X-RAYS. 128
A2.1 INTERACTIONS OF MEDIUM ENERGY X-RAYS WITH MATTER 128
A2.2 RADIATION QUANTITIES. 129
A2.2.1 FLUENCE. 129
A2.2.2 ENERGY FLUENCE. 129
A2.2.3 MASS ENERGY TRANSFER COEFFICIENT. 129
A2.2.4 MASS ENERGY ABSORPTION COEFFICIENT. 130
A2.2.5 ABSORBED DOSE AND AIR KERMA. 130
A2.2.5.1 KERMA. 130
A2.2.5.2 ABSORBED DOSE. 131
A2.3 DETERMINATION OF ABSORBED DOSE TO WATER USING MEDIUM ENERGY X-RAYS. 132
APPENDIX 3 PARAMETERS USED TO CALCULATE THE HEAT DEFECT 134
APPENDIX 4 CONDUCTION OF HEAT IN THE ICE CALORIMETER 137
A4.1 INTRODUCTION. 137
A4.2 GENERAL CONDUCTION. 137
A4.3 RADIAL AND AXIAL FLOW OF HEAT IN THE ICE CALORIMETER. 138
A4.4 THERMISTOR OVERSHOOT. 138
A4.5 TOTAL CORRECTION DUE TO HEAT CONDUCTION. 139

CHAPTER 1

INTRODUCTION.

In the United Kingdom, radiotherapy with external photon beams is performed mainly with beam energies equal to or greater than that of ^{60}Co. However, medium energy X-rays are routinely used for treating tumours close to the surface of the skin and for palliation. In England [1] from 1992-1993, 89,898 radiotherapy exposures were administered using medium energy X-rays.

Presently in the UK [2], dosimetry using medium energy X-rays for radiotherapy is based on ICRU Report 23 [3]. In 1987 the International Atomic Energy Agency [4] published a Code of Practice (IAEA TRS 277). This resulted in the absorbed dose to water determined using IAEA TRS 277 being greater than that using ICRU Report 23 by a maximum of 12.5% at 0.15 mm Cu HVL (see figure 1.1). A second set of factors have recently been published by the IAEA [5] resulting in the maximum difference between the two codes being halved. The initial aim of this project is to measure the absorbed dose to water accurately using medium energy X-rays and therefore resolve the discrepancy among the three sets of data.

In the UK the secondary standard therapy level chamber is a NE2561. The second aim of this project was to determine the factors to convert the air kerma measured using a NE2561 chamber to absorbed dose to water.

1.1 OUTLINE OF THE THESIS

This thesis is divided into seven chapters, the first four chapters investigate the measurement of absorbed dose to water using ionization chambers, while the final three chapters explore calorimeters. Chapter 2 describes the measurement of absorbed dose to water using an ionization chamber and analyses the difference between IAEA TRS 277 and ICRU Report 23.

In Chapter 3 a suitable ionization chamber to measure absorbed dose to water in the medium energy X-ray range is investigated. The chamber correction factor (k_{ch}) for the U.K secondary standard chamber (NE2561) is determined and the constituent

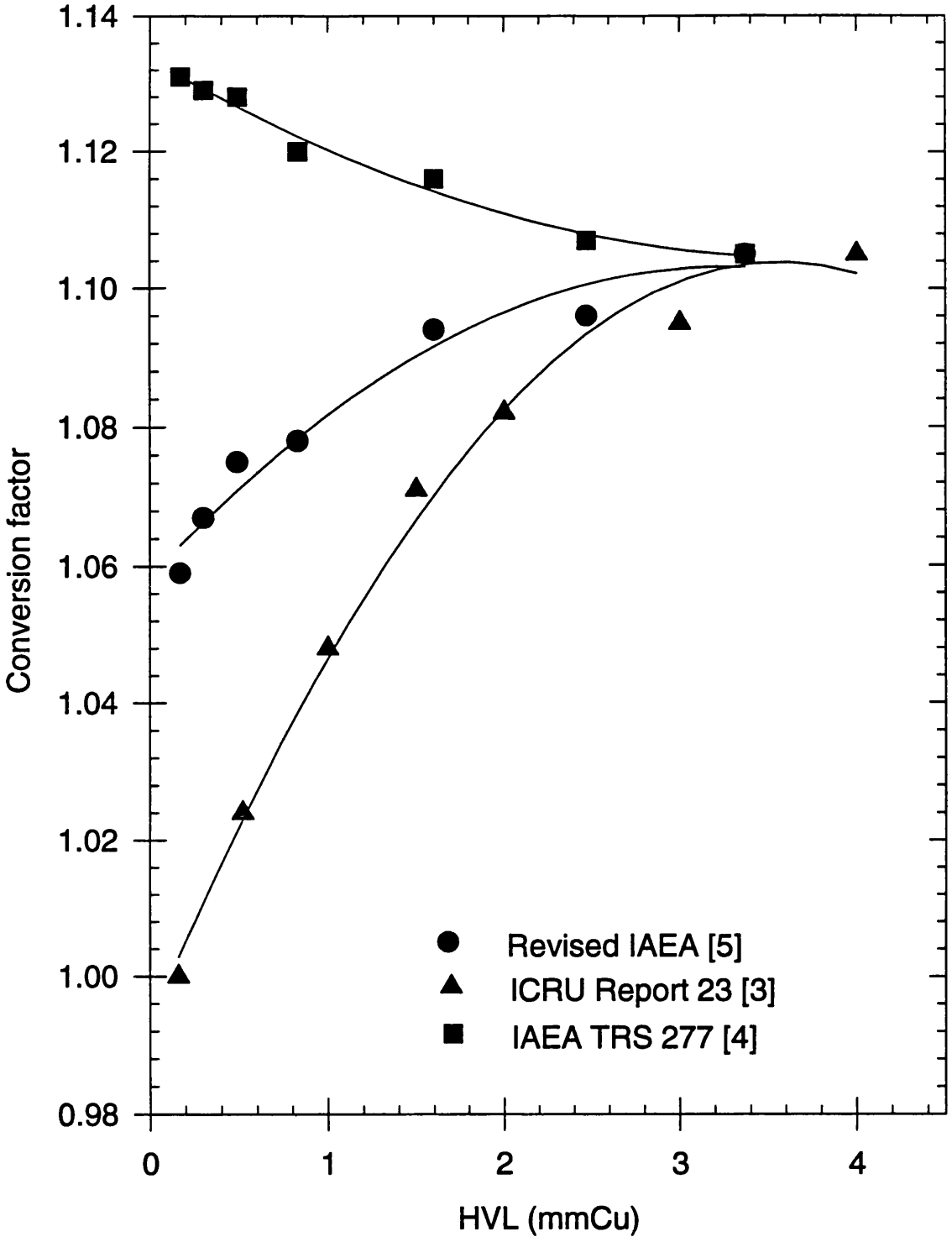

Figure 1.1 Comparison of the factors to convert the air kerma measured using an ionization chamber to absorbed dose to water at 5 cm deep in water

parts of k_{ch} are analysed.

In Chapter 4 the ratio of mass energy absorption coefficients of water to air over the medium energy X-ray range are calculated using Monte Carlo techniques based on measured primary spectra. In the second half of the chapter a suitable beam quality index for medium energy X-rays is investigated. The results of a survey of the quality index used by medium energy radiotherapy centres in the UK are presented.

Chapter 5 describes calculations of the heat defect for water when irradiated with medium energy X-rays and shows initial measurements with a water calorimeter.

Chapter 6 describes the design and construction of an ice calorimeter. The measurements of absorbed dose to water using the ice calorimeter, irradiated with ^{60}Co gamma rays is compared with the primary standard graphite calorimeter using an ionization chamber as the transfer method. The absorbed dose to water measured using the ice calorimeter irradiated with 134 kV X-rays is compared with a NE2561 ionization chamber and its chamber correction factor found.

The final chapter summarises the results obtained in this project and makes suggestions for future improvements to the ice calorimeter.

CHAPTER 2

MEASUREMENT OF ABSORBED DOSE WATER USING MEDIUM ENERGY X-RAYS.

2.1 DETERMINATION OF ABSORBED DOSE TO WATER USING IAEA TRS 277.

For X-ray beams between 0.17 and 3.37 mm Cu HVL (100 kV and 280 kV generating potential), the IAEA code [4] recommends that the absorbed dose to water is measured using a calibrated ionization chamber. If the ionization chamber is on the beam axis, with its centre at 5 cm deep in a water phantom and irradiated with a 10 x 10 cm^2 field, the absorbed dose to water is given by:

$$D_w = M \cdot N_k \cdot k_u \cdot \left(\frac{\bar{\mu}_{en}}{\rho} \right)_{w,a} \cdot P_u \qquad (1)$$

where:

D_w is the absorbed dose to water in grays at the position of the centre of the chamber, with the chamber replaced by water,

M is the instrument reading corrected to the same ambient conditions as the calibration factor,

N_k is the air kerma calibration factor of the instrument for standard ambient conditions and for the radiation quality of the incident beam in air,

k_u is a correction factor allowing for the change in response of the ionization chamber due to the change in the spectral distributions between the 'in air' calibration and the measurement at the reference depth in water,

$(\bar{\mu}_{en}/\rho)_{w,a}$ is the ratio of the mass energy absorption coefficients of water to air averaged over the photon spectrum at the point of measurement,

P_u is the perturbation correction factor for the replacement of water by the ionization chamber.

2.2 COMPARISON OF THE MEASUREMENT OF ABSORBED DOSE TO WATER DETERMINED USING IAEA TRS 277 TO THAT USING ICRU REPORT 23.

ICRU Report 23 [3] recommends the same experimental technique as that given in IAEA TRS 277 [4] for determining absorbed dose to water using a calibrated ionization chamber. However, ICRU Report 23 recommends that the calibration factor for an ionization chamber be in the old units of exposure the Röntgen. The equation for determining absorbed dose to water in the two codes is essentially the same except that ICRU Report 23 combines P_u, $(\bar{\mu}/\rho)_{w,a}$, $(W/e)_a$ and k_u to form a F-factor. Values for $(W/e)_a$, $(\bar{\mu}/\rho)_{w,a}$ and P_u will now be discussed.

2.2.1 THE ENERGY REQUIRED TO PRODUCE AN ION PAIR IN AIR.

At the time of the publication of ICRU Report 23 the accepted value of the energy required to produce an ion pair in air, $(W/e)_a$ was 33.7 JC^{-1}. The IAEA code does not require a value of $(W/e)_a$ but it is used by the standards laboratory to convert the exposure measured using the primary standard free air chamber to air kerma. The latest value recommended by CCEMRI [6] is 33.97 JC^{-1}. This change in the value of $(W/e)_a$ results in an increase of only 0.8% in the determination of absorbed dose to water and is trivial compared to the maximum difference between the two codes.

2.2.2 THE RATIO OF MASS ENERGY ABSORPTION COEFFICIENT OF WATER TO AIR.

Values of the ratio of mass energy absorption coefficient of water to air averaged over the photon fluence spectrum at the point of measurement $(\bar{\mu}_{en}/\rho)_{w,a}$ are given in IAEA TRS 277. ICRU Report 23 does not distinguish this ratio from the F-factor, but it can be derived if the replacement correction is taken to be unity. Figure 2.1 shows that the maximum difference, between the values of $(\bar{\mu}_{en}/\rho)_{w,a}$ given in the two codes is 2.5% at 0.17 mm Cu HVL. This will be discussed in more detail in chapter 4.

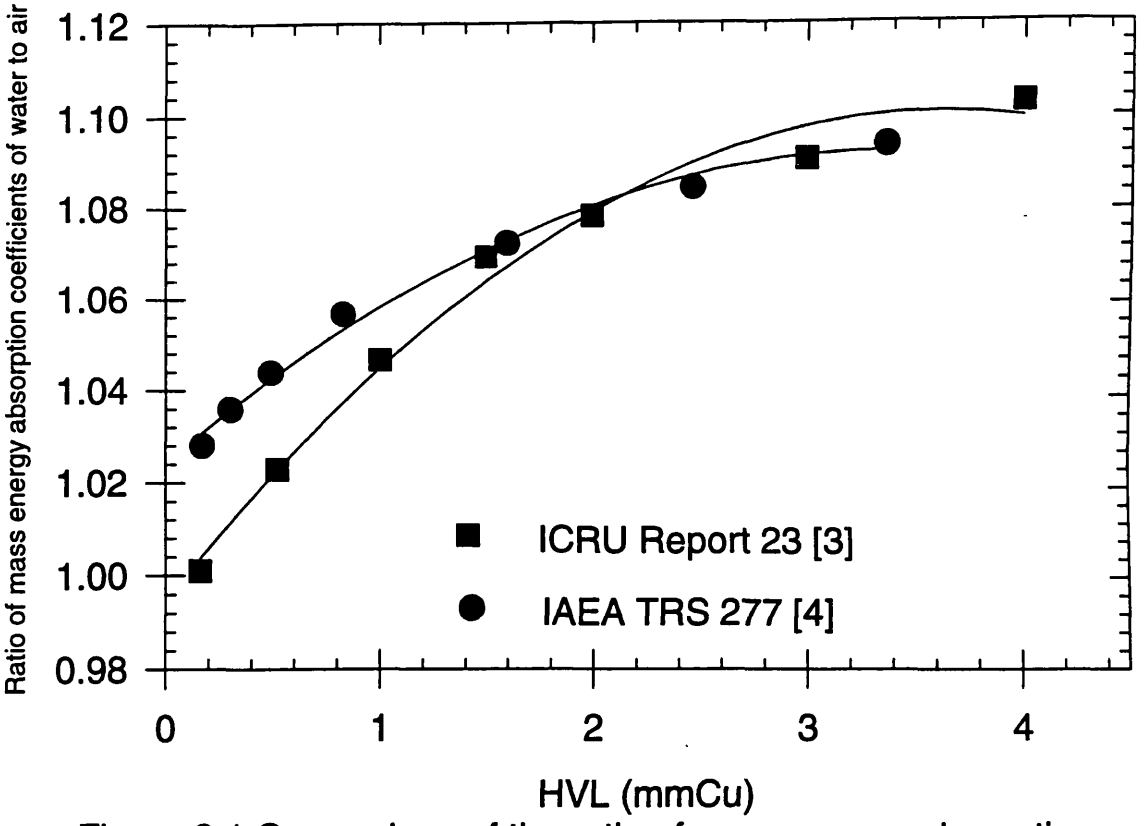

Figure 2.1 Comparison of the ratio of mass energy absorption coefficients of water to air given in the two codes.

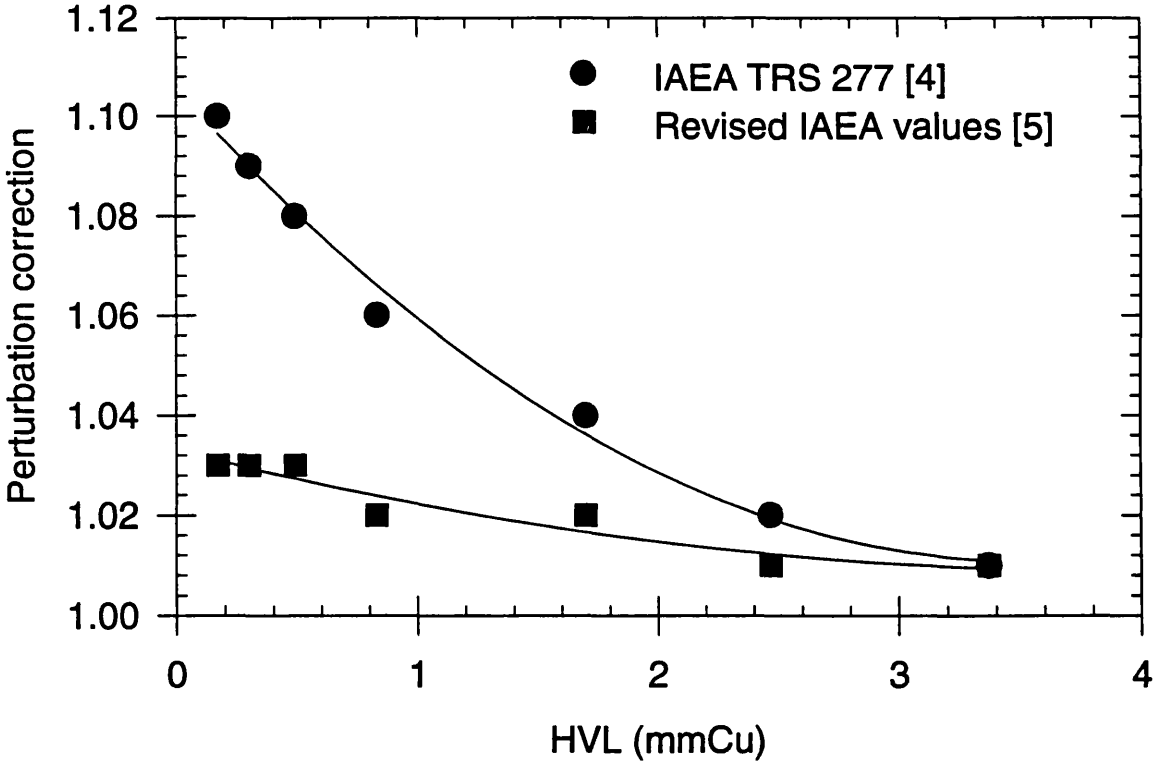

Figure 2.2 Comparison of the perturbation correction given in IAEA TRS 277 and the revised IAEA values.

2.2.3 PERTURBATION CORRECTION.

When an ionization chamber is calibrated in air, the effective point of measurement is taken as geometrical centre of the chamber. Inside a phantom the effective point of measurement is displaced due to the change in attenuation and scatter of the beam, when the phantom material is replaced by the chamber cavity and chamber materials. IAEA TRS 277 and ICRU Report 23 recommend that in a phantom the geometric centre of the ionization chamber should be placed at the point of measurement and a correction applied. In the literature several terms are used for the correction due to the air cavity such as perturbation, displacement and replacement correction. In this thesis the correction for the cavity will be called the replacement correction (p_{rep}).

The value of this correction given in ICRU Report 23 and IAEA TRS 277 is very different. Figure 2.2 shows the value of the correction given in IAEA TRS 277 decreases from 10 to 1% between 0.17 and 3.37 mmCu HVL respectively, whereas ICRU Report 23 adopts a value 'much less than 1%'. There is some confusion in the literature about the definition of the perturbation correction, IAEA TRS 277 state that the values quoted for the perturbation correction are due to the replacement effect solely. Whereas the review of the data [5]states that the values account for any difference in the response of the chamber when calibrated in air and used in a water phantom. To save additional confusion, in this thesis the revised definition will be adopted and called the chamber correction factor (k_{ch}), defined as:

$$k_{ch} = k_{\alpha} \cdot k_{st} \cdot p_{rep} \cdot k_{sleeve} \qquad (2)$$

where

k_{α} allows for the energy and angular dependence on the response of the ionization chamber in the water phantom compared to when the chamber is calibrated in air,

k_{st} accounts for the influence of the stem on the response of the ionization chamber free in air and in water,

p_{rep} is the replacement correction,

k_{sleeve} accounts for the effect of the waterproof sleeve on the response of the ionization chamber in water.

2.3 LITERATURE SEARCH TO DETERMINE THE VALUE OF THE CHAMBER CORRECTION FACTOR.

There are three possible methods of determining the value of the chamber correction factor. Firstly the individual elements of the chamber correction factor can be found experimentally or using Monte Carlo methods. Secondly the absorbed dose to water can be measured using a water calorimeter or an extrapolation chamber. This is then compared with the absorbed dose to water determined using an ionization chamber with an air kerma calibration. The difference between the two methods is usually attributed to the chamber correction factor. Thirdly the chamber correction factor can be found by a combination of experimental and Monte Carlo techniques. This literature search will examine the chamber correction factor derived using three methods.

2.3.1 DETERMINATION OF THE CHAMBER CORRECTION FACTOR USING THE INDIVIDUAL COMPONENT METHOD.

2.3.1.1 REPLACEMENT CORRECTION.

There have been more investigations of the replacement correction than any of the other components of the chamber correction factor. The value of the perturbation correction given in IAEA TRS 277 is inconsistent with that given in ICRU Report 23 for two main reasons. Firstly the large value adopted in IAEA TRS 277 and secondly the correction is greater than unity. Initially the sign of the replacement correction will be investigated.

Liden [7] considered that the replacement effect would be due to a combination of three effects namely:

a) The decreased filtration of the primary beam,

b) The decreased filtration of the scattered radiation,

c) The elimination of scattering from the displaced volume.

The first two effects are important at very low energies (less than 30 keV) while the last effect plays an increasing role at higher energies. Over the medium energy X-ray range one would expect the first two factors to increase the photon fluence in the cavity and the third to decrease it. These effects partly cancel but will probably result in the photon fluence at the centre of the chamber being too high and so the replacement correction is expected to be less than unity.

Harrison [8] has confirmed this visually by sandwiching a sheet of water equivalent Gafchromic radiation sensitive film between two blocks of solid water equivalent material. Each block contained half a cavity corresponding to the outer dimensions of a NE2571 chamber. The phantom was then irradiated with a 10 x 10 cm^2 field at SSD 100 cm at 60, 90, 140 kVp (2.2, 3.3 and 5.2 mm Al HVL respectively). Harrison found that the cavity showed a higher optical density than its surroundings, showing a replacement correction less than unity. Table 2.1 shows the replacement correction for ionization chambers with different volumes.

TABLE 2.1 VALUE OF THE REPLACEMENT CORRECTION

Author	Rakov and Will [9]	Rakov and Will [9]	Zoetelief et al[10]	Zoetelief et al[10]
Type of ionization chamber	Homemade of diameter 20 mm	Homemade of diameter 20 mm	Homemade spherical chambers of radius 6-16 mm	Homemade spherical chambers of radius 6-16 mm
X-ray Radiation	HVL= 0.5 mmCu	HVL= 2 mmCu	220 kV	300 kV
Replacement correction	0.95	0.96	1.006±0.006	1.015±0.006

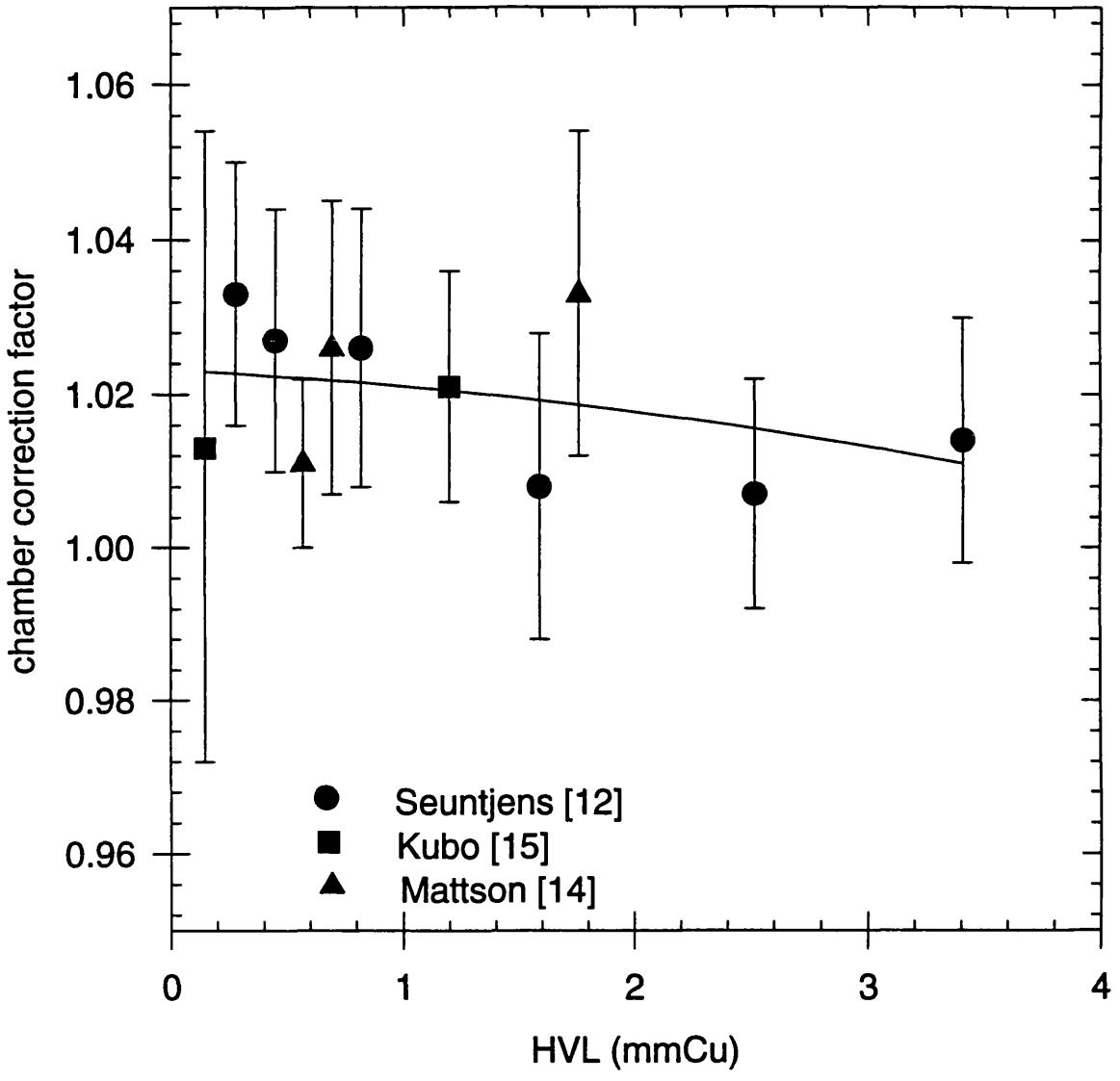

Figure 2.3 Chamber correction factor for a Farmer ionization chamber determined using water calorimetry.

2.3.1.2 REMAINING COMPONENTS OF THE CHAMBER CORRECTION FACTOR.

The replacement, stem correction factor and k_α for the ionization chambers commonly used in the UK are given in Chapter 3, as determined by Ma [11] and Seuntjens [12]. Rakov and Will [13] investigated the stem correction for ionization chambers not widely available in the UK and found that the stem correction varied from 1.007 to 1.07. Unfortunately there is no data available on the effect of the waterproof sleeve on the response of an ionization chamber.

2.3.2 DETERMINATION OF THE CHAMBER CORRECTION FACTOR BASED ON A DIRECT METHOD OF DETERMINING ABSORBED DOSE TO WATER.

Figure 2.3 compares the chamber correction factor for a Farmer type chamber based on water calorimetry using medium energy X-rays. The results given by Mattson [14] and Kubo [15] have been reevaluated in this thesis by initially adopting the ratio of mass energy absorption coefficients of water to air recommended in IAEA TRS 277. A correction due to the heat defect of water, assumed to be 3.5% [49] was then applied to the calorimetry measurements.

Figure 2.4 shows the chamber correction factor for a 1 cm^3 PTW chamber presented by Schneider et al [16] based on the method of determining the absorbed dose to water using a graphite extrapolation chamber.

2.3.3 DETERMINATION OF THE CHAMBER CORRECTION FACTOR USING MEASUREMENT AND CALCULATIONS.

The chamber correction factor can be derived from the response of a chamber in air (M_a) and at the reference depth in water (M_w) in the same radiation field. This can then be compared with the calculated ratio of air kerma in air (K_a) and at the reference depth in a phantom (K^w_a)

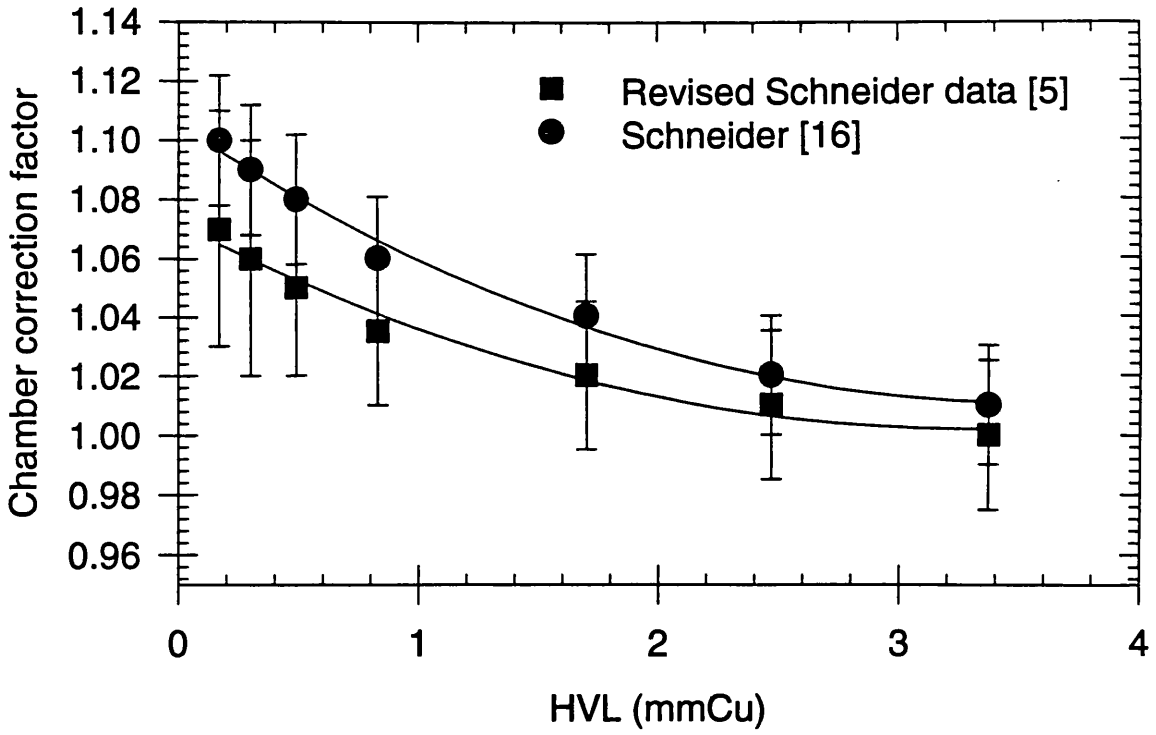

Figure 2.4 Chamber correction factors determined using a graphite extrapolation chamber.

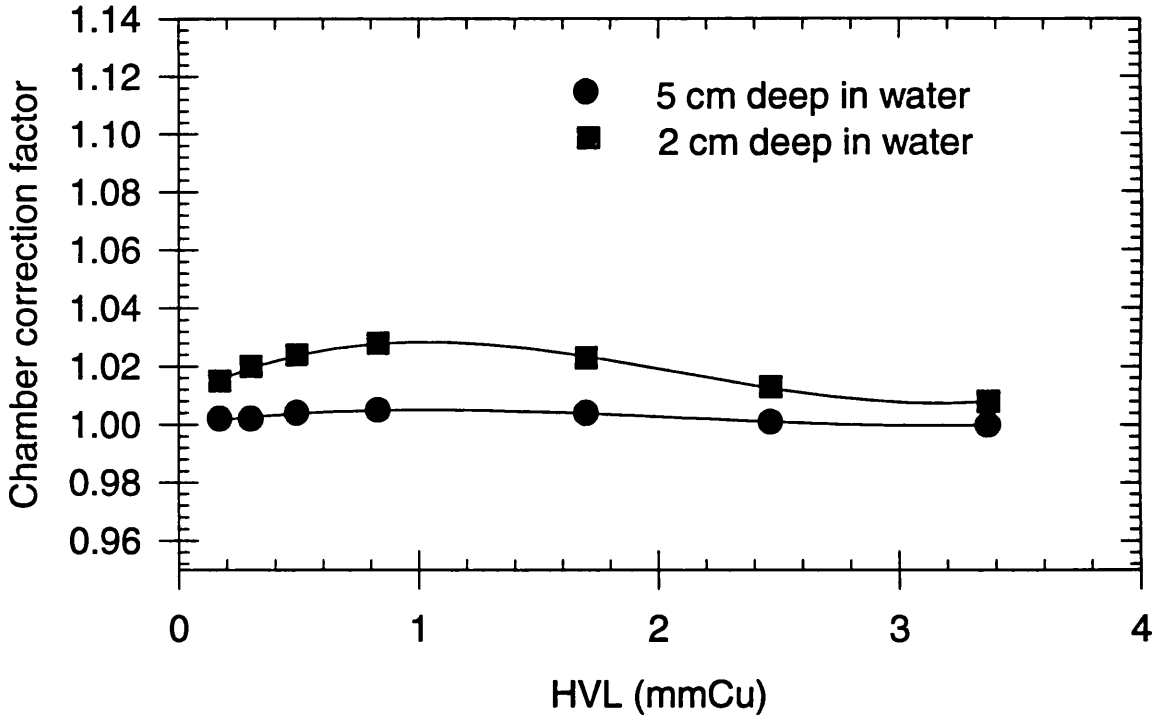

Figure 2.5 Chamber correction factor determined using the calculation and experimental method presented by Schneider et al [16]

$$k_{ch} = \frac{K_a^w}{K_a} \cdot \frac{M_a}{M_w} \qquad (3)$$

Figure 2.5 shows the value of the chamber correction factor found by Schneider et al [16] for a 1 cm^3 PTW ionization chamber.

2.4 DISCUSSION.

The review of the literature shows that the values of k_{ch} determined using a graphite extrapolation chamber are inconsistent with the other methods.

The components of the chamber correction factor are dependent on the construction, size of the ionization chamber and on the irradiation conditions. IAEA TRS 277 and ICRU Report 23 have ignored this dependence and simply quote a single factor for all recommended chambers. In the UK the designated secondary standard is the NE2561 or the modern version the NE2611. There is sparse information in the literature on the chamber correction factor for a NE2561, only Ma [11] has calculated it using Monte Carlo methods. Therefore, one aim of this thesis is to determine the chamber correction factor for a NE2561 chamber over the medium energy X-ray range.

CHAPTER 3

DETERMINATION OF ABSORBED DOSE TO WATER USING AN IONIZATION CHAMBER.

3.1 INTRODUCTION.

In this chapter the suitability of an ionization chamber used to measure absorbed dose to water when irradiated with medium energy X-rays will be studied. Four different types of cylindrical chambers were initially investigated. However cylindrical chambers are not ideal for this energy range as they measure an average dose over steep depth dose curves. To improve the spatial resolution three parallel plate chambers were investigated for their suitability in this energy range.

The chamber correction factors for a NE2561 chamber will then be determined. Finally the components of the chamber correction factor for a NE2561 chamber will be explored.

3.2 SUITABLE IONIZATION CHAMBERS TO MEASURE ABSORBED DOSE TO WATER USING MEDIUM ENERGY X-RAYS.

According to ICRU Report 23 [3] the desirable features of an ionization chamber for the measurement of absorbed dose to water are:

1. The variation in response of the chamber in air should not exceed 5% over the medium energy X-ray range.
2. The internal diameter should be about 5 mm and length 15 mm, dimensions twice as great as these should never be exceeded.
3. The stem of the chamber should not significantly affect the response of the chamber.
4. The wall thickness should be greater than the range of the secondary electrons to ensure that the electrons entering the cavity originate in the wall and not in the surrounding medium.
5. The polarizing potential should be high enough so that ion recombination is negligible in the chamber.

Initially the energy response of several ionization chambers will be investigated.

3.2.1 METHOD

Three types of parallel-plate and four types of cylindrical ionization chambers were calibrated in air over the medium energy X-ray range by direct comparison with the primary standard free air chamber (see figure 3.1). The details of the ionization chambers are given in Table 3.1.

The thin window of the PTW Grenz chamber was not thick enough to stop the secondary electrons produced in the surrounding medium entering the chamber cavity. It was therefore calibrated with a 1 mm thick Perspex plate over its window.

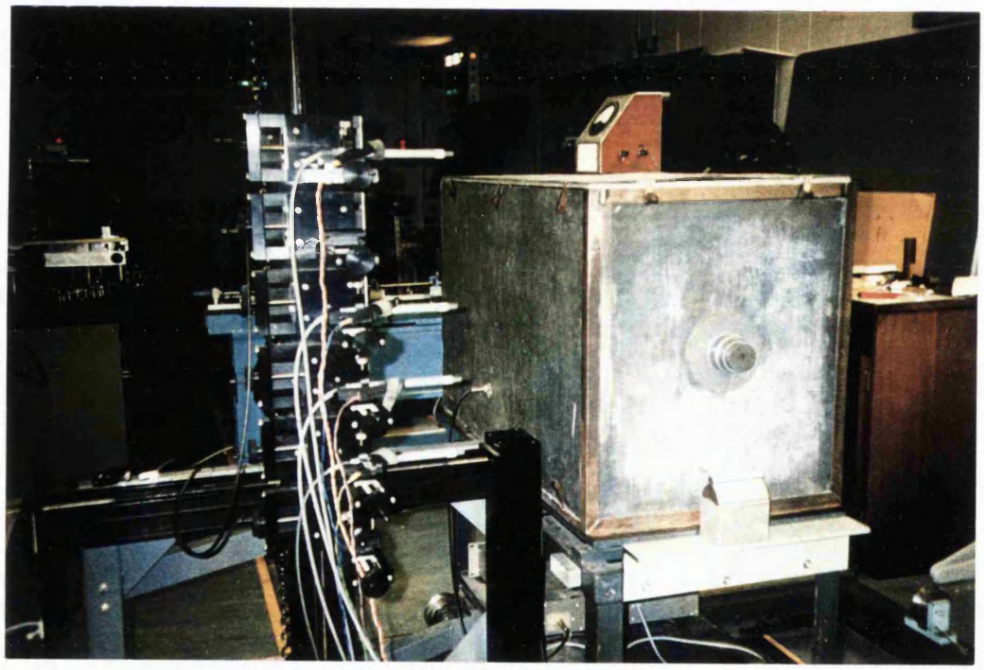

Figure 3.1: Calibration of NE2561 chambers by direct comparison with the primary standard free air chamber.

TABLE 3.1 IONIZATION CHAMBERS CALIBRATED IN AIR

Type	Producer	Sensitive volume	Chamber wall	Polarizing potential
		(cm^3)		(V)
Parallel plate chambers				
Grenz	PTW	0.2	0.03 mm CH_3	-200
NPL electron chamber (E5)	NPL	0.3	35 μm Cu on 1 mm Perspex	-200
NACP electron chamber	Scanditronix	0.16	0.5 mm graphite + 0.1 mm Melinex	-200
Cylindrical chambers				
Farmer type 2505/3	N E Technology	0.6	approx 0.5 mm graphite	-200
Farmer type 2515/1	N E Technology	0.22	0.3 mm graphite	-200
NE2561 (NPL secondary standard)	N E Technology	0.3	0.5 mm graphite	-200
NE2561 (modified)	NPL	0.3	approx. 0.5 mm Al	-200

Comparison of the response of ionization chambers in air.

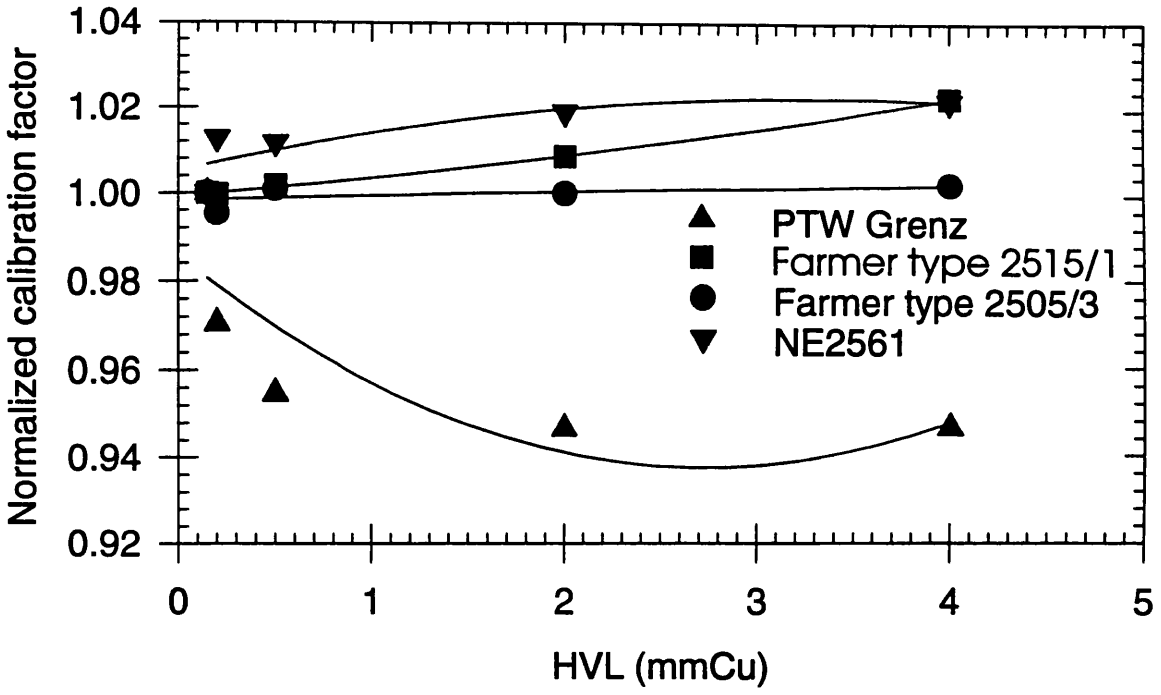

Figure 3.2a

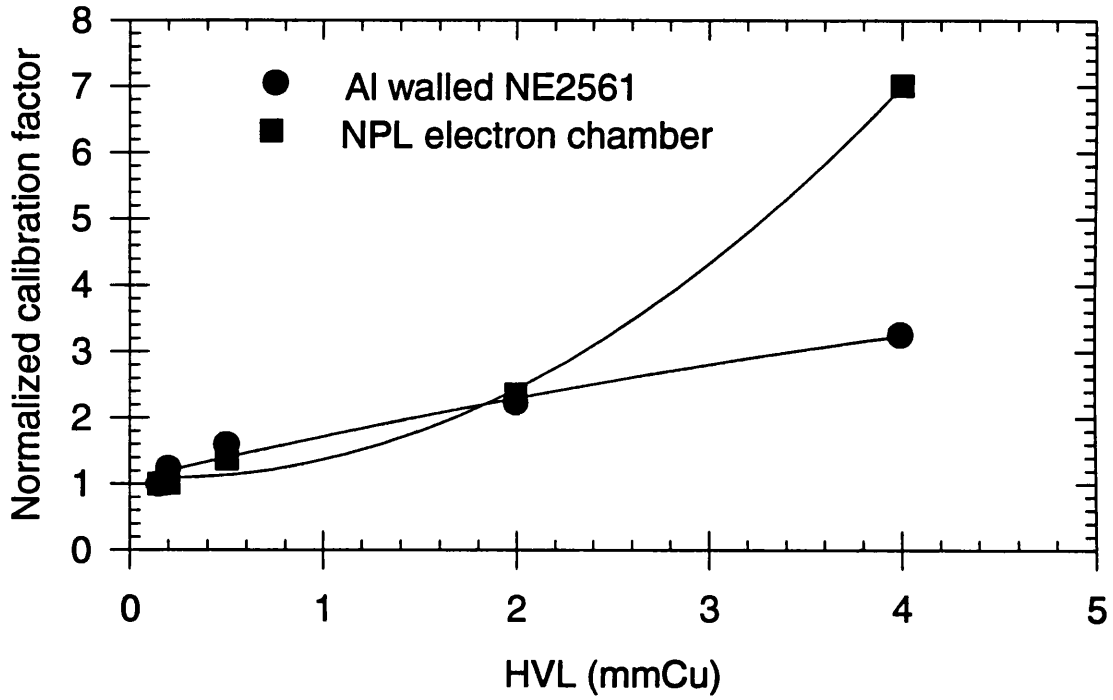

Figure 3.2b

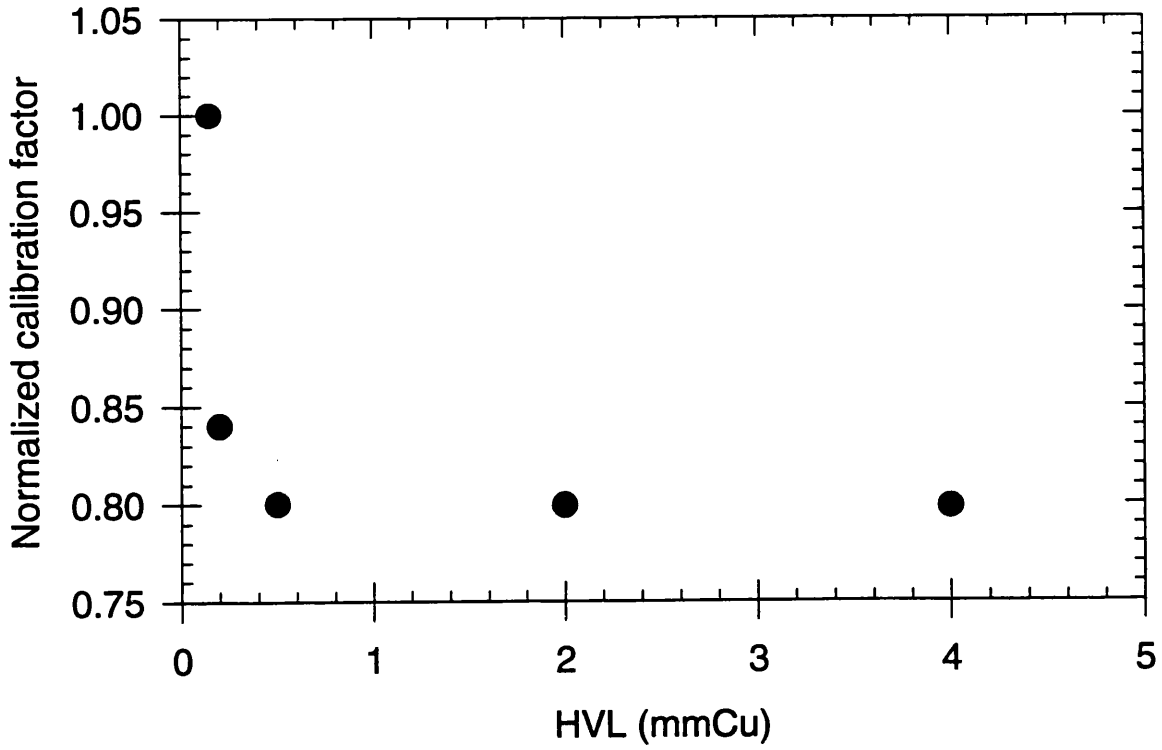

Figure 3.2c Response of a NACP electron chamber in air.

3.2.2 DISCUSSION

Figure 3.2a shows that the NE2561, the two Farmer type chambers and the PTW Grenz chamber have a response in air that does not vary by more than 5% over the medium energy X-ray range. There are two design features of an ionization chamber that can be altered to achieve a response that is independent of energy. The material and thickness of the wall must be chosen to achieve charged particle equilibrium. This creates problems at the lower photon energies because the incident photons will be attenuated by the wall. To compensate for this effect the central electrode can be made of a high-atomic number material such as aluminum that emits photo-electrons at low energies. This is the case for the cylindrical graphite walled chambers used in this thesis. For the PTW Grenz chamber the compensation is provided by backscatter from its Perspex housing.

Figures 3.2b and 3.2c show that the NACP electron chamber, the NPL electron

chamber and the NE2561 chamber with an Al wall are unacceptable for use in a medium energy X-ray beam, as their energy responses vary by more than 5%. The NACP electron chamber does not contain any high atomic number materials and therefore its response falls at low energies due to attenuation of the primary beam. The large variation in response of the NPL electron chamber and modified NE2561 chamber is due to the wall of the chambers made of high atomic number material.

3.3 DETERMINATION OF ABSORBED DOSE TO WATER USING A SUITABLE IONIZATION CHAMBER.

The absorbed dose to water can be determined using an ionization chamber by:

$$D_w = M \cdot N_k \cdot k_{ch} \cdot \left(\frac{\bar{\mu}_{en}}{\rho} \right)_{w,a} \qquad (4)$$

where:

D_w is the absorbed dose to water in Grays at the position of the centre of the chamber, with the chamber replaced by water,

M is the instrument reading corrected to the same ambient conditions as the calibration factor,

N_k is the air kerma calibration factor of the instrument for standard ambient conditions and for the radiation quality of the incident beam in air,

$(\bar{\mu}/\rho)_{w,a}$ is the ratio of the mass energy absorption coefficients of water to air averaged over the photon spectrum at the points of measurement,

k_{ch} is the chamber correction factor.

Now that suitable ionization chambers have been found for the determination of absorbed dose to water each component of equation 4 will be discussed, except $(\bar{\mu}/\rho)_{w,a}$.

3.3.1 THE READING OF AN IONIZATION CHAMBER (M).

The reading of the ionization chamber should be corrected to the same conditions as when the chamber was calibrated at the national standards laboratory, i.e. temperature and pressure, humidity and ion recombination. Table 3.2 give the corrections that should be applied to the reading of a NE2561 chamber when irradiated using medium energy X-rays.

TABLE 3.2 CORRECTIONS TO THE READING OF A N2561 IONIZATION CHAMBER.

Correction	Determination of correction	Comments
Temperature (°C) and pressure (kPa)	$\frac{273.15 + T}{293.15} \cdot \frac{101.325}{P}$ T and P is the temperature and pressure of the air in the chamber respectively.	Burns et al [17] have shown that this equation is only valid in the range 20 to 70% RH for temperatures between 15 to 25 °C
Humidity [18]		Negligible 20 to 70% RH
Ion recombination (F_{ion}) [19]	F_{ion}= 1.0014	For an ionization chamber calibrated in terms of air kerma no correction is required.

3.3.2 MEASUREMENT OF AIR KERMA USING A PRIMARY STANDARD FREE AIR CHAMBER.

There is consensus in Europe for the measurement of air kerma using a free air chamber. Marsh et al [20] summarized a comparison of the determination of exposure using ten free air chambers. He found that nine of the chambers agreed within 1.8% when irradiated with X-rays generated between 100 and 250 kV.

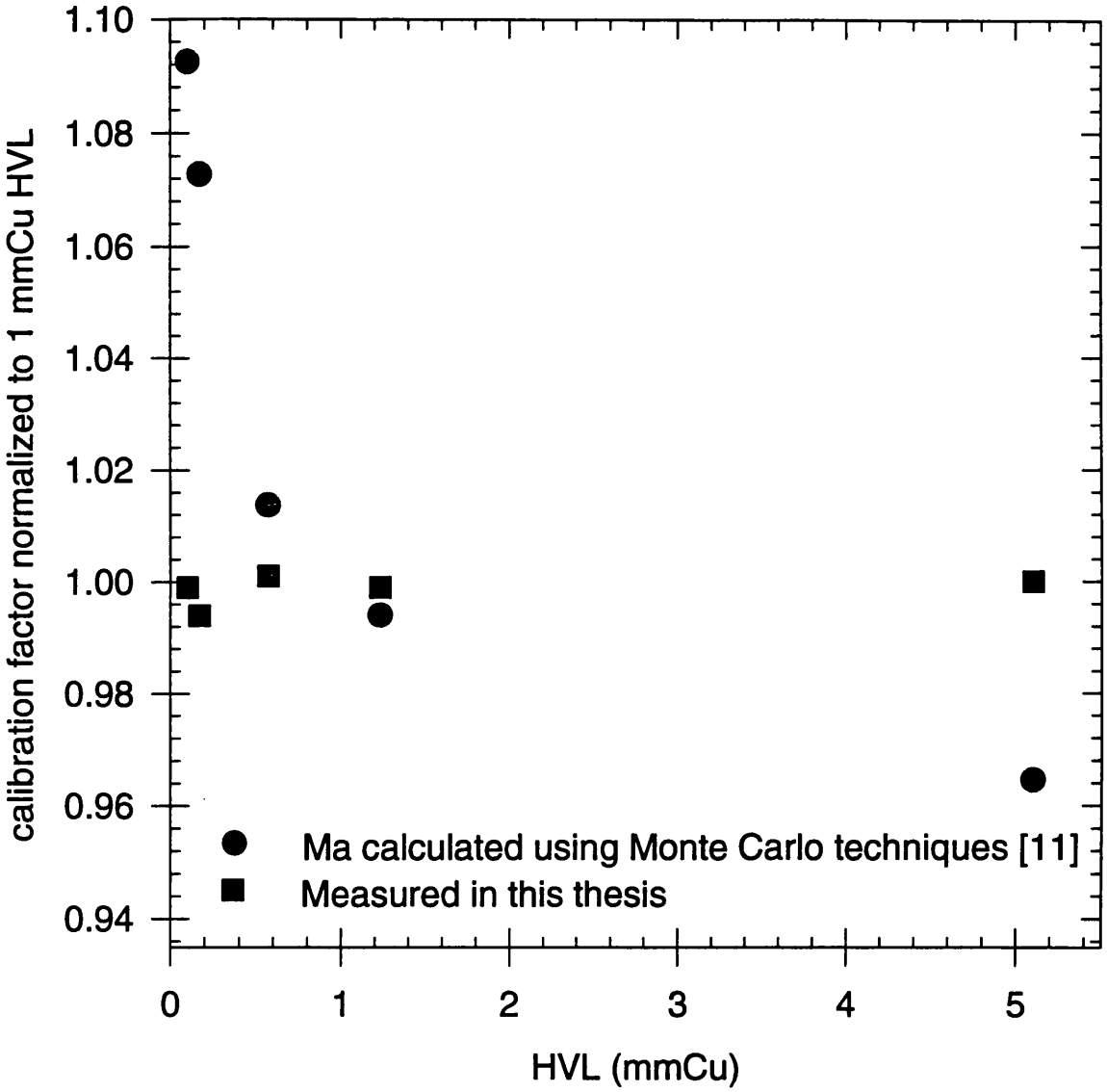

Figure 3.3 Calibration curve for a Farmer type ionization chamber.

However, Ma[11] calculated the calibration curve for a NE2571 ionization chamber over the medium energy X-ray range (see figure 3.3) using Monte Carlo techniques. Ma found that the energy response of a NE2571 chamber varied by 13% between 0.1 and 5.1 mmCu HVL. Whereas the measurements presented in figure 3.3 show that the calibration factor should not vary by more than 0.6 % over this energy range. Ma suggested that the large difference between experiment and Monte Carlo calculation maybe due a systematic error in the measurement of air kerma using a free air chamber. This is due to free air chambers having similar constructions and apply similar corrections factors. This could have serious consequences in the determination of air kerma worldwide.

Bernard at al [21] measured the calibration factor for a graphite cavity chamber by direct comparison with the primary standard free air chamber. This was then compared with the calibration factor calculated using Bragg-Gray cavity theory and found that they differed by 0.6% for X-rays generated at 250 kV. Unfortunately this experiment was done at a quality that is no longer used at NPL for calibrations and there was some uncertainty in the spectrum used for the calculations.

In this thesis the same graphite cavity chamber as used by Bernard et al was calibrated using X-rays generated at 220 and 280 kV. Shipley [22] calculated the calibration factor for the graphite cavity chamber at 220 and 280 kV using the EGS4 Monte Carlo code and DOSRZ. Shipley used the spectra measured in this thesis (see Chapter 4) as the basis for the calculations. The effect of the chamber was calculated by taking the ratio of the dose to the cavity with and without the chamber present. The difference between the calibration factor calculated by Shipley [22] and those measured agree within 0.5%. This suggests that the primary standard free air chamber is measuring exposure correctly and there is a problem with the calculations given by Ma.

3.4 ESTIMATION OF THE CHAMBER CORRECTION FACTOR FOR A NE2571 IONIZATION CHAMBER.

Seuntjens [12] and Ma et al [11] have investigated the chamber correction factor for a NE2571 Farmer chamber with a graphite wall. Unfortunately figure 3.4 shows that the chamber correction factors given by Ma and Seuntjens differ by a maximum of 3.6% at 0.2 mm Cu HVL. Therefore, the chamber correction factor for a NE2571 was taken as the mean of these factors.

3.5 COMPARISON OF THE CHAMBER CORRECTION FACTOR FOR A NE2561 CHAMBER WITH THAT FOR A NE2571 CHAMBER.

The chamber correction factor for an ionization chamber can be found by comparison of the absorbed dose to water with that measured using a chamber with a known chamber correction factor.

$$\frac{(D_w)_1}{(D_w)_2} = \frac{\left(M \cdot N_k \cdot \left(\frac{\bar{\mu}_{en}}{\rho} \right)_{w,a} \cdot k_{ch} \right)_1}{\left(M \cdot N_k \cdot \left(\frac{\bar{\mu}_{en}}{\rho} \right)_{w,a} \cdot k_{ch} \right)_2} \qquad (6)$$

Hence:

$$\frac{(k_{ch})_1}{(k_{ch})_2} = \frac{(M\ N_k)_2}{(M\ N_k)_1} \qquad (7)$$

The subscript 1 and 2 refer to the different types of ionization chambers. The chamber correction factor for a Farmer type NE2571 ionization chamber is known therefore this will be taken as chamber 2. The construction of a Farmer type NE2571 chamber and type 2505/3 is identical.

3.5.1 METHOD

The responses of the Farmer type 2515/1, the PTW Grenz, the Al walled NE2561 and the NE2561 chambers were compared with the response of the Farmer type 2505/3 chamber in air and at 2 cm deep in water. The measurements in water were

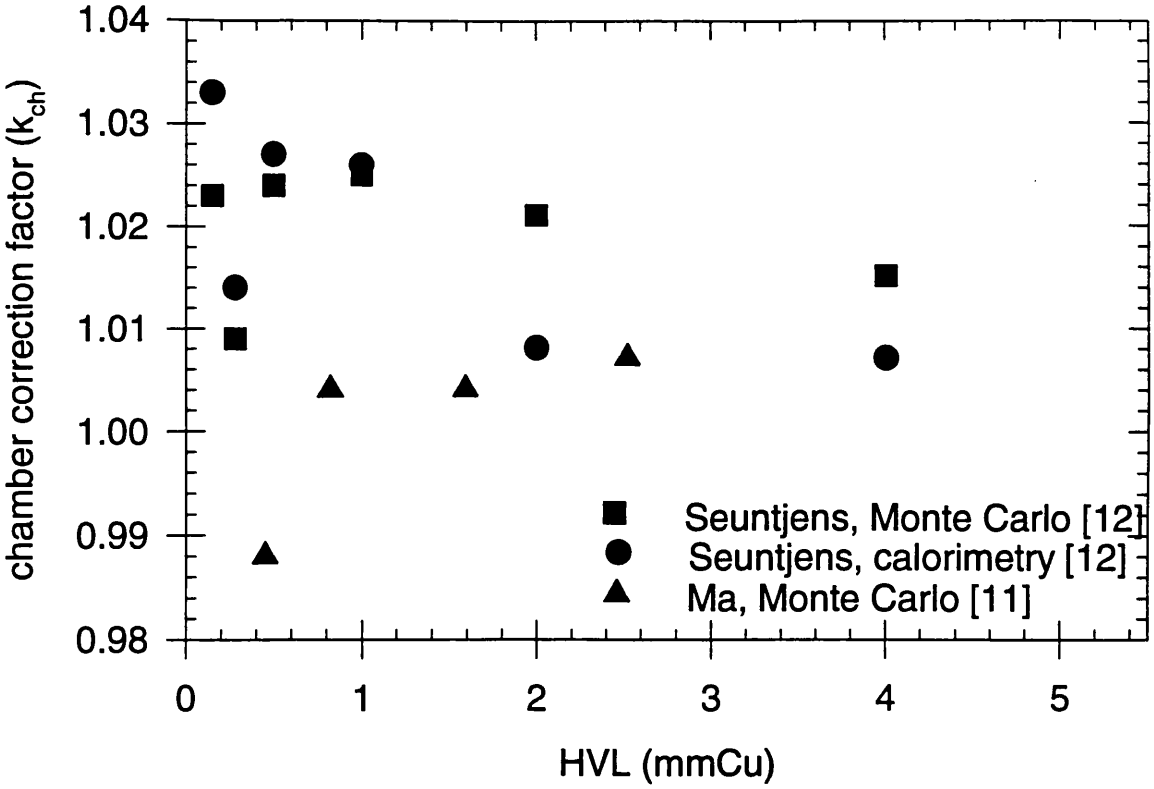

Figure 3.4: Comparison of the chamber correction factor for a Farmer type chamber.

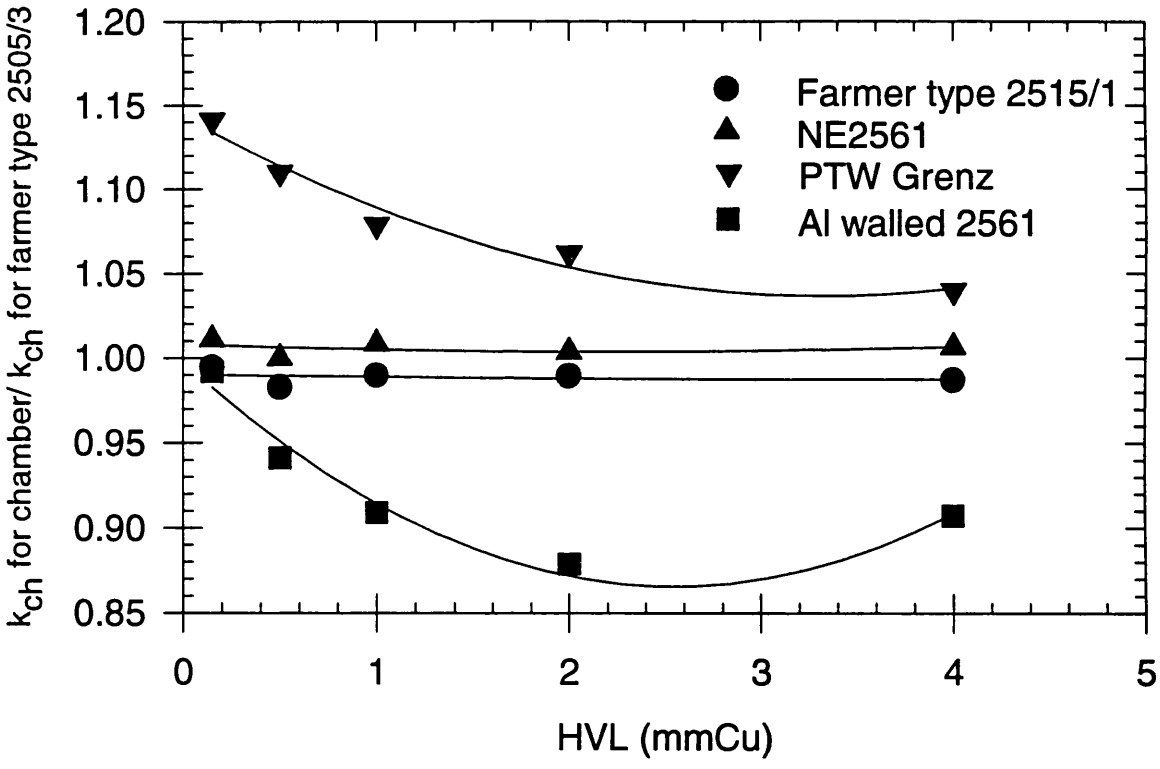

Figure 3.5: Comparison of chamber correction factors.

carried out using the same primary beam qualities that were used for the calibration in air (see Appendix 1). The measurements in air (see section 3.2.1) and in water were done at 75 cm source to surface distance (SSD), with a beam diameter of 6 cm. The water phantom had a cross-sectional area of 31 x 41 cm and was 31 cm deep.

3.5.2 DISCUSSION

Figure 3.5, shows that the graphite walled chambers have similar chamber correction factors. The aluminum walled NE2561 chamber shows a maximum deviation from unity of 14% at 2 mm Cu HVL and is due to its large energy response in air. This should set a limit on the value of the chamber correction factor. As a chamber whose response varies by a factor of three in air (see figure 3.2b), has a chamber correction factor that varies by only 14% over the medium energy X-ray range.

The difference between the chamber correction factor for each of the graphite walled cylindrical chambers and the PTW Grenz chamber is due to backscatter from the 1.5 cm thick Perspex housing of the PTW Grenz chamber. The backscatter from the Perspex housing is incorporated in the air kerma calibration factor. Therefore at a depth in water the chamber is approximately measuring air kerma in air and not the required air kerma in water. The backscatter factor [2] for a 4 x 4 cm^2 field decreases by 10% between 0.15 and 4 mm Cu HVL. Figure 3.5 shows that the variation of the chamber correction factor for the PTW Grenz chamber compared with the chamber correction factor for the Farmer chamber varies by 8% between 0.15 and 4 mm Cu HVL. The difference between measurement and the published backscatter factors may be due to the measurements being performed in water, as the backscatter factors were determined at the surface of the phantom. This shows that an ionization chamber with a housing that provides backscatter is not a suitable chamber for measuring absorbed dose to water using medium energy X-rays.

3.5.3 ESTIMATION OF THE CHAMBER CORRECTION FACTOR FOR A NE2561 CHAMBER.

The data quoted by Ma and Seuntjens was for a chamber irradiated with a 10 x 10 cm field, whereas the comparison in this thesis was done using a 6 x 6 cm field. The chamber correction factors for a NE2571 were converted to a 6 x 6 cm field by assuming that the variation of the stem correction with field size is the same for a NE2561 chamber as for a NE2571 (see section 3.6.1).

Figure 3.6a and 3.6b shows the resulting chamber correction factor for a NE2561 chamber irradiated with two different field sizes.

TABLE 3.3 UNCERTAINTIES FOR THE CHAMBER CORRECTION FACTOR FOR A NE2561 CHAMBER.

	Uncertainty (1σ) (%)			
HVL (mm Cu)	Mean value of k_{ch} for a Farmer NE2571	$\frac{k_{ch}\ NE2561}{k_{ch}\ NE2571}$	converting stem correction from 10 x 10cm to 6 x 6 cm field	Overall uncertainty
0.15	3	0.2	0.1	3
0.20	2	0.2	0.1	2
0.5	1.3	0.3	0.1	1.7
1.0	1.5	0.1	0.1	1.5
2.0	1.5	0.1	0.1	1.5
4.0	0.1	0.1	0.1	0.1

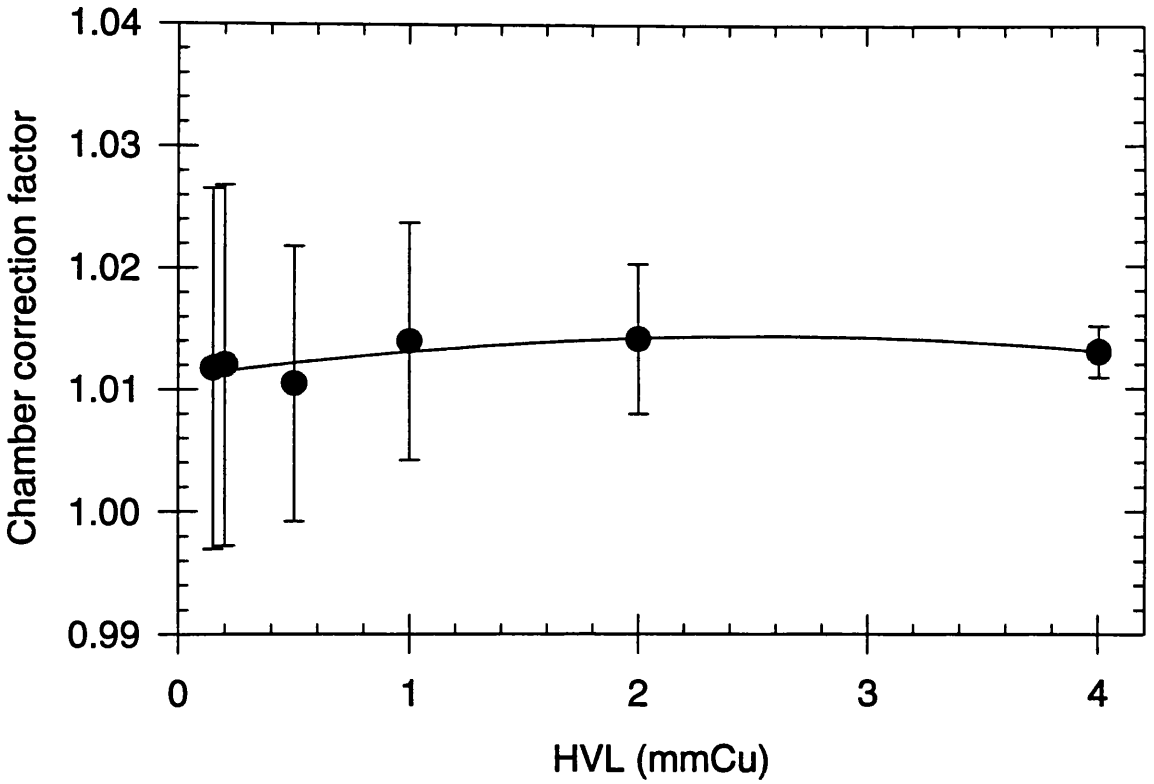

Figure 3.6a: Derived chamber correction factor for a NE2561 chamber irradated with a 6 x 6 cm field.

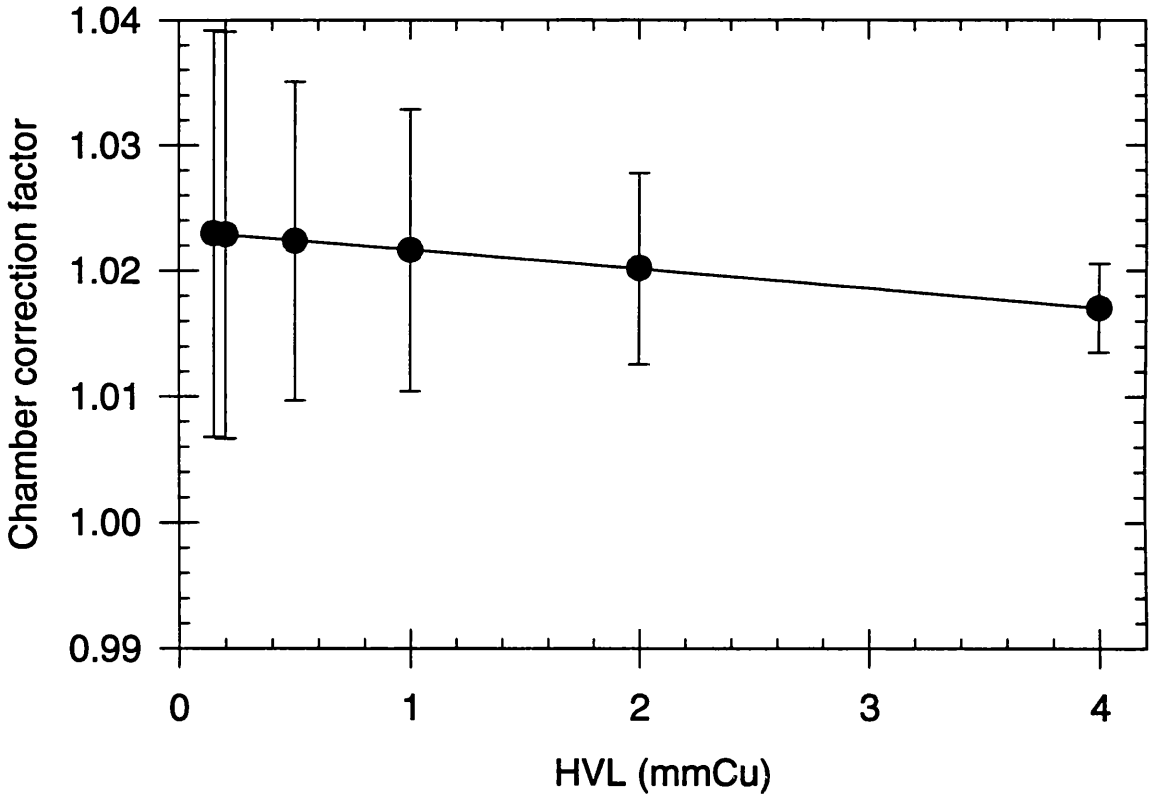

Figure 3.6b: Derived chamber correction factor for a NE2561 chamber irradiated with a 10 x 10 cm field.

3.6 DETERMINATION OF THE COMPONENTS OF THE CHAMBER CORRECTION FACTOR FOR A NE2561 IONIZATION CHAMBER.

The individual components of the chamber correction factor will now be estimated for a NE2561 ionization chamber. This may indicate where the large value of the chamber correction factor given in IAEA TRS 277 originated.

3.6.1 STEM CORRECTION FOR A NE2561 IONIZATION CHAMBER

The absorbed dose to water is required at a point in a water phantom without an ionization cavity and stem. The presence on the stem will alter the photon fluence spectrum at the chamber. Partly because of radiation scattered by the stem and partly due to replacement of the phantom material by the chamber stem. The stem correction is dependent on the stem material, stem diameter, field size and phantom material.

For a chamber calibrated in terms of air kerma the effect of stem scatter (k_{scat}) is incorporated in the calibration factor. To determine the absorbed dose to water using a calibrated ionization chamber only a correction due to the replacement of the phantom material by the stem should be incorporated into the chamber correction.

The 'dummy stem' method of determining the stem correction is where a stem of identical construction to the chambers stem is placed adjacent to the original stem on the opposite side of the chamber. The stem correction is the ratio of the chamber response with and without the 'dummy' stem. This method measures (k_{meas}) the stem effects due to scatter (k_{scat}) and replacement (k_{rep}) of the phantom material.

$$k_{meas} = k_{scat} \cdot k_{rep} \qquad (8)$$

The correction due to the replacement of the phantom material by the stem can

be calculated by dividing the 'in air' scatter correction by the measured factor in a phantom. This assumes that the stem scatter 'in air' and 'in phantom' are identical and is valid if the field size and spectra are identical 'in air' and 'in phantom'. The 'in air' stem scatter (k_{scat}) corrections were taken from Burns [23].

3.6.1.1 METHOD

The stem scatter correction in a phantom was measured using the dummy stem method. These measurements were done in a 26 x 26 x 23 cm^3 polystyrene phantom, at 3 cm deep for 5.8 cm and 11.3 cm field diameters. The distance from the X-ray target to the front face of the phantom was 50 cm and 97.4 cm for beam diameters 5.8 cm and 11.3 cm respectively. The stem scatter correction was the mean of a series of three measurements with and without the dummy stem. The difference between the maximum and minimum stem correction in any set did not exceed 0.15%.

The variation of the stem correction with HVL is shown in figures 3.7a and 3.7b for 5.8 cm and 11.3 cm diameter fields.

3.6.1.2 DISCUSSION

In air, the stem scatter increases the response of the chamber, whereas in a water phantom the replacement of the water by the stem reduces the response of the chamber. Figures 3.7a and 3.7b show that the stem replacement correction ranges from 2.8% to 0.8% for a 5.8 cm diameter beam and 3.9% to 1.2% or a 11.3 cm diameter beam for HVLs between 0.15 and 4.00 mm Cu. In practice an ionization chamber is calibrated in air using a 7 cm diameter field and the codes of practice recommend that the measurement in a phantom be made using a 10 x 10 cm^2 field. This change in field size is negligible for the in air calibration.

This method of determining the stem scatter correction may not be strictly valid due to the asymmetrical construction of the ionization chamber. So the dummy stem on the opposite side of the chamber from the chamber stem may not have the same effect as the stem itself. However Ma et al [24] calculated the stem correction for a

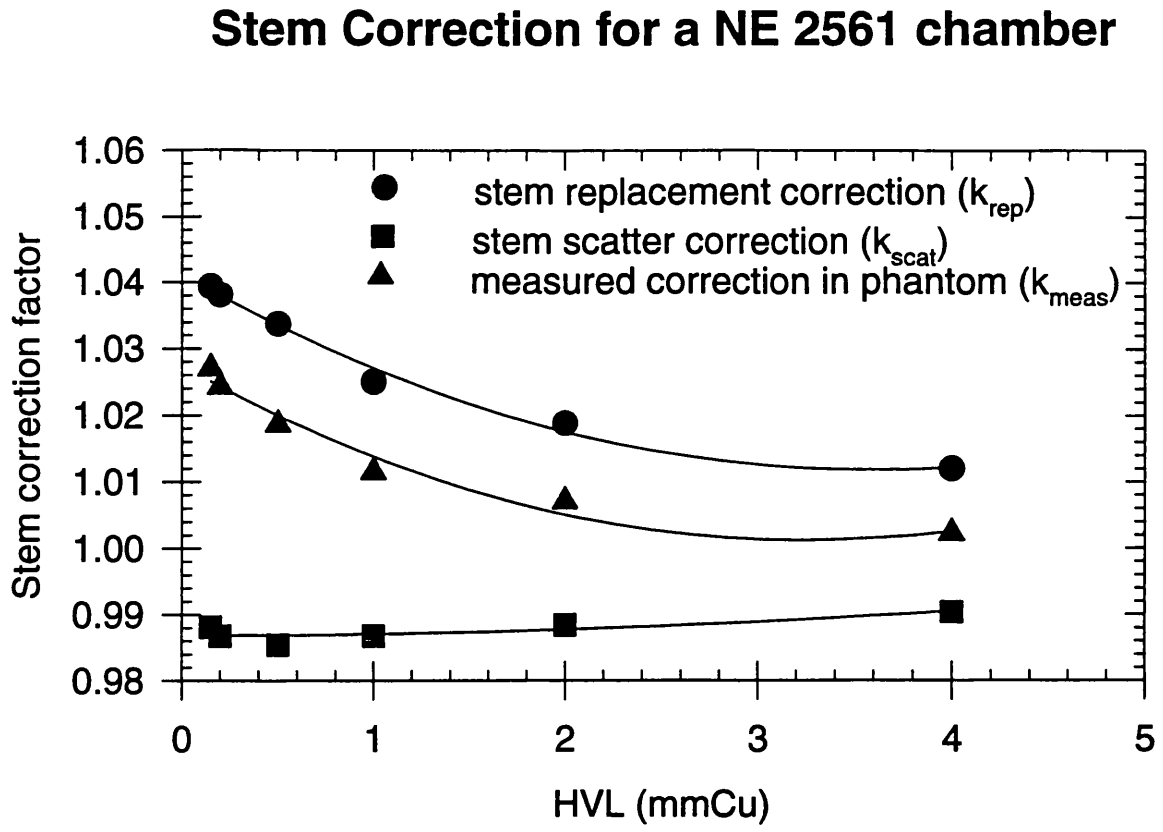

Figure 3.7a: Stem correction for a 11.3 cm diameter field.

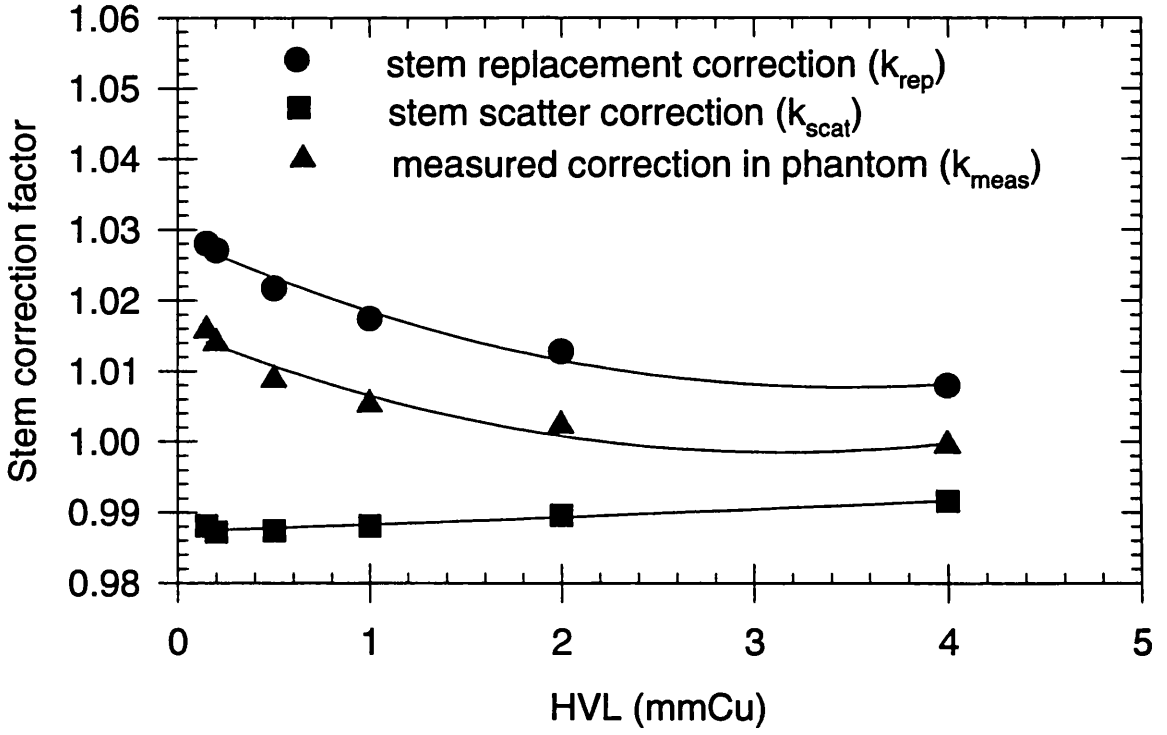

Figure 3.7b: Stem correction for a 5.8 cm diameter field.

NE2561 chamber using Monte Carlo techniques. Figure 3.8 shows a comparison between the factors given by Ma and those reported in this thesis. The stem correction factors agree within the stated uncertainty.

The stem correction for a NE2561 ionization chamber is greater than that determined by Seuntjens [12] and Ma [11] for a NE2571 ionization chamber by a maximum of 1.4% at 0.5 mmCu HVL. This difference may be due to the dimensions of the stems, as the NE2561 chamber has a stem 12.5 mm in diameter whereas the diameter of the stem of a NE2571 is 8.5 mm.

3.6.2 EFFECTS OF WATERPROOF SLEEVES.

To waterproof an ionization chamber when it is used in a water phantom, it is placed in a sleeve. Neither IAEA TRS 277 nor ICRU Report 23 mention the need for a waterproof sleeve when using medium energy X-rays. Therefore the recommendations given in the IPSM [25] high energy code of practice were adopted. That is:

(1) The wall of the sleeve is sufficiently thin to allow the chamber to achieve thermal equilibrium in about five minutes.

(2) The sleeve should be vented to the atmosphere to allow the air pressure in the chamber to reach ambient air pressure quickly.

The material of the sleeve could affect the chamber correction factor. This is dependent on the effective atomic number and the amount of backscattered radiation from the sleeve.

3.6.2.1 METHOD

Three sleeves of identical dimensions were investigated made of Perspex, polystyrene and tissue equivalent material. The response of a NE2561 chamber was compared in each sleeve at 2 cm deep in water. The NE2561 ionization chamber was then calibrated in air over the medium energy X-ray range with each sleeve placed over the chamber and then without the sleeve. The measurements in water were carried out using the same primary beam qualities as were used for the calibration

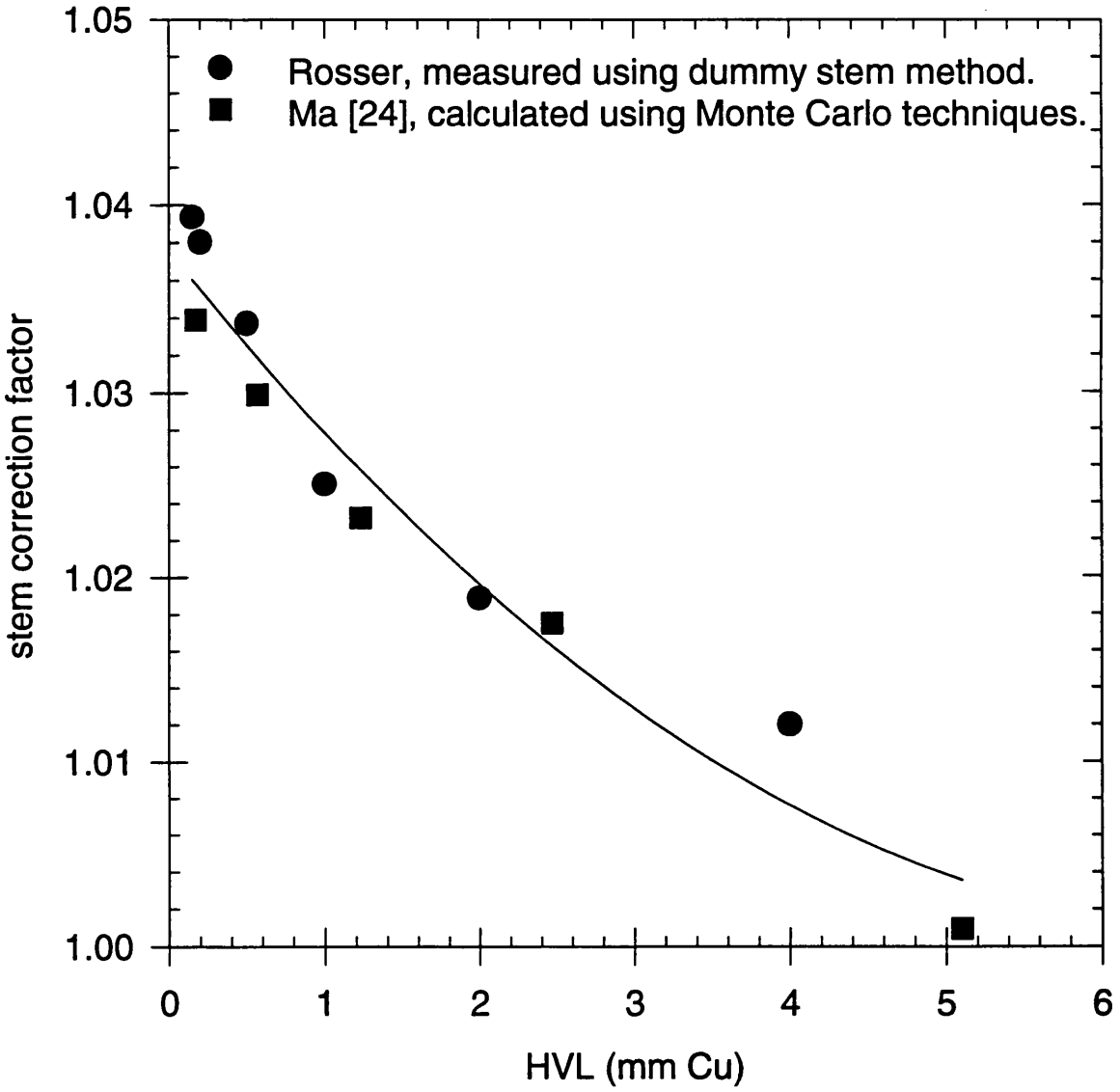

Figure 3.8: Comaprison of the stem correction factor for a NE2561 chamber in a 10 x 10 cm field.

in air. The measurements in air (see section 3.2.1) and in water were done at 75 cm source to surface distance (SSD), with a beam diameter of 6 cm. The water phantom had a cross-sectional area of 31 x 41 cm and was 31 cm deep.

The chamber correction factor for each sleeve compared to that for the tissue equivalent plastic sleeve $[(k_{ch})_{te}/(k_{ch})_s]$ is given by:

$$\frac{(k_{ch})_s}{(k_{ch})_{te}} = \frac{M_{te}N_{te}}{M_sN_s} \qquad (9)$$

where:

M is the response of the ionization chamber at 2 cm deep in water,

N is the calibration factor in air in terms of air kerma.

3.6.2.2 DISCUSSION

In practice an ionization chamber is calibrated in air without a sleeve. Figures 3.9a and 3.9b show that this could result in a change in the chamber correction factor of up to 2% for a polystyrene sleeve at the lowest energy. This could be significantly reduced if the chamber is calibrated in air in its waterproof sleeve.

3.6.3 REPLACEMENT CORRECTION.

Unfortunately there is very little data on the value of the replacement correction for a NE2561 ionization chamber. Ma [11] calculated the correction using an attenuation and scattering method similar to that used by Cunningham and Sontag [26].

Figure 3.10 compares the replacement correction for a NE2561 with that for a NE2571 chamber. It can be seen that the factors given by Ma and Seuntjens for a NE2571 agree within 0.2%. This good agreement is not surprising as both authors calculated the correction using the EGS4 Monte Carlo code. The replacement correction for a NE2561 is less than that for a NE2571 by a maximum of 1.4% at the lowest energy.

Effect of sleeve material on k_{ch} for a NE2561.

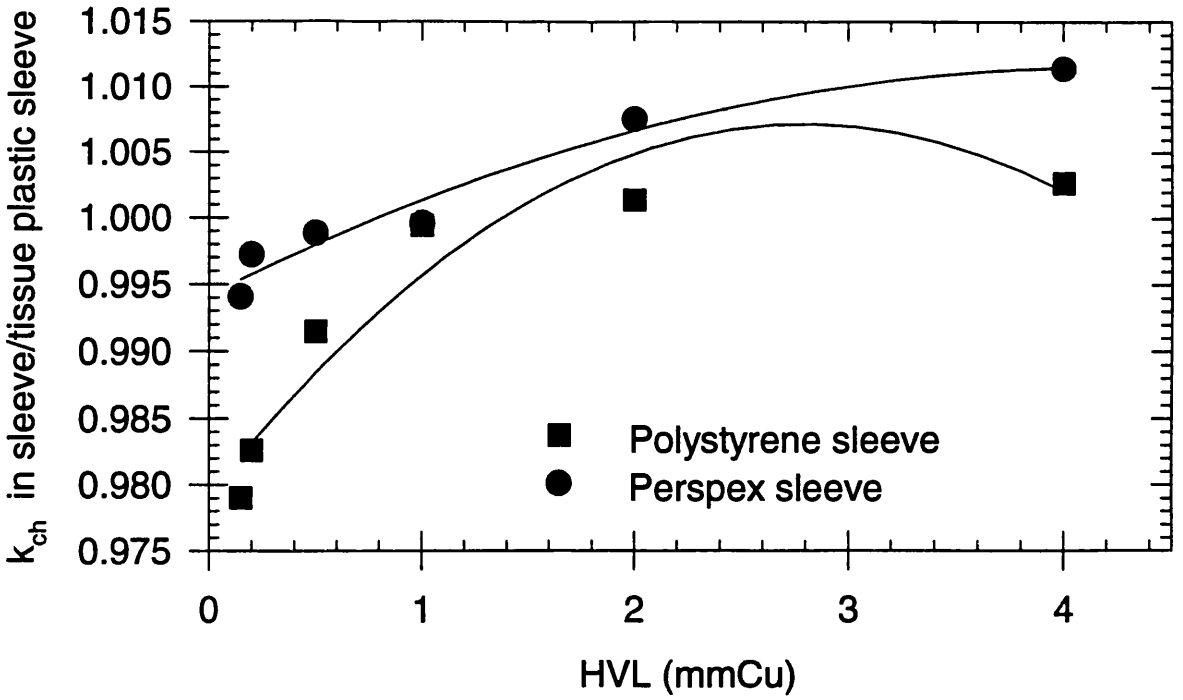

Figure 3.9a: Comparison of sleeves when a NE2561 is calibrated in air without a sleeve.

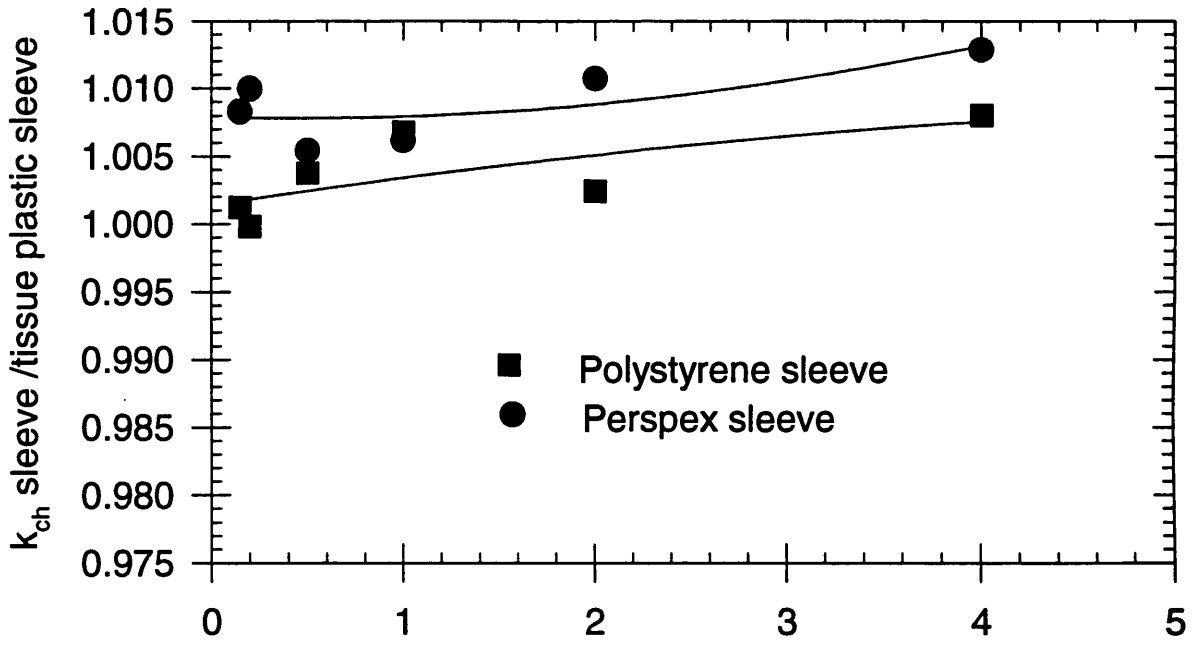

Figure 3.9b: Comparison of sleeves when a NE 2561 is calibrated in air with a sleeve.

This is due to the difference in dimensions of the two chambers, the outer diameter of the NE2561 is 8.4 mm and length is 10 mm. Whereas a NE2571 is 26 mm long and outer diameter 7.4 mm. This agrees with Ma [11] who showed that for a chamber irradiated with 70 kV X-rays the replacement correction will increase by 2% when its length is increased by from 10 to 26 mm. Also the replacement correction will increase by 0.6% when the outer diameter is decreased by from 8.5 to 7.5 mm.

3.6.4 SUMMARY OF THE COMPONENTS OF THE CHAMBER CORRECTION FACTOR FOR A NE2561 CHAMBER.

A summary of the components of the chamber correction factor for a NE2561 chamber is given in Figure 3.11. Where $k_{\alpha}k_{sleeve}$ was calculated by dividing the measured chamber correction factor by the stem and replacement correction.

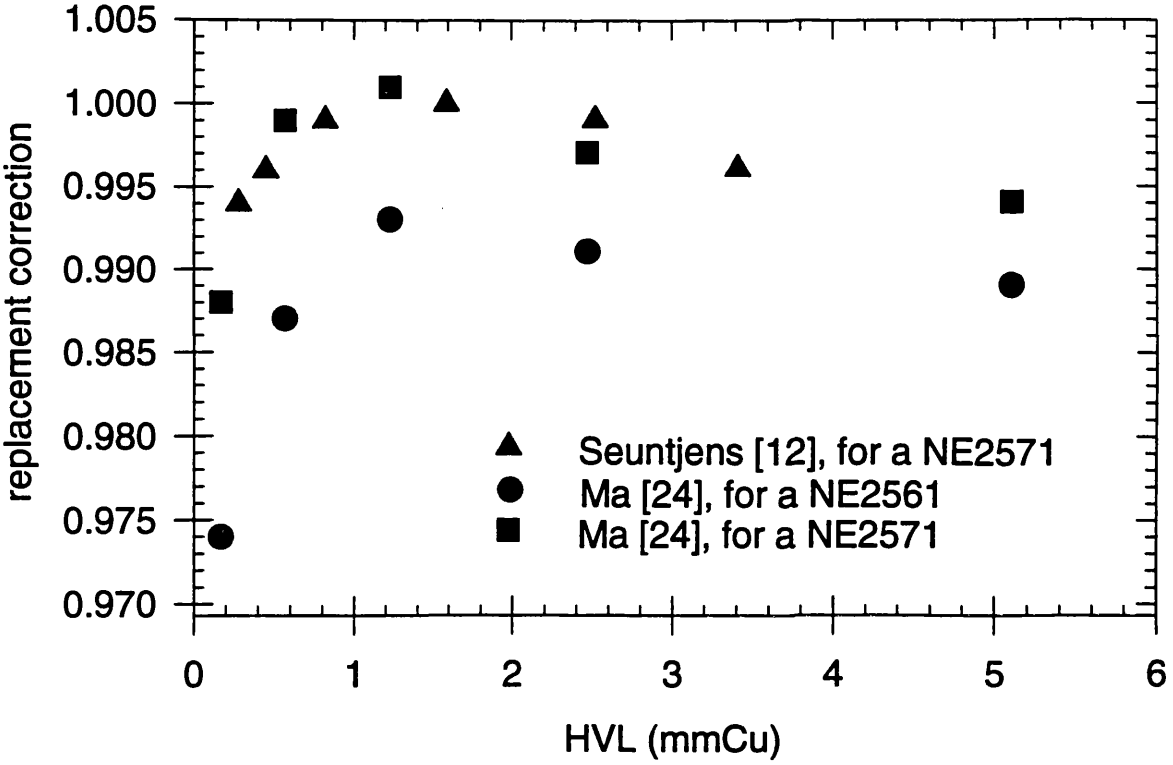

Figure 3.10: Comparison of the replacement correction for a NE2561 and NE2571 ionization chambers.

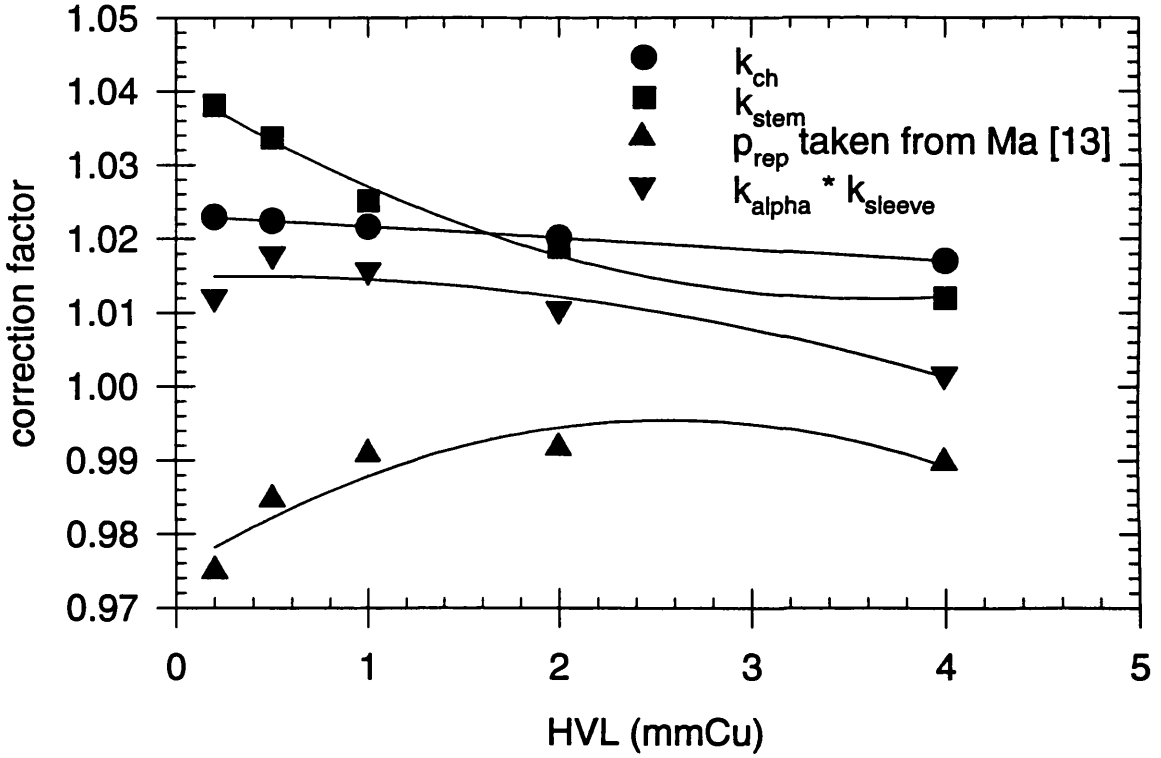

Figure 3.11: Components of k_{ch} for a NE2561 chamber, irradiated with a 10 x 10 cm field.

CHAPTER 4

INVESTIGATION OF THE RATIO OF MASS ENERGY ABSORPTION COEFFICIENTS OF WATER TO AIR AND THE DETERMINATION OF A BEAM QUALITY INDEX FOR MEDIUM ENERGY X-RAYS.

4.1 INTRODUCTION.

Most of the difference between the measurement of absorbed dose to water measured using ICRU Report 23 and IAEA TRS 277 is due to the value of the chamber correction factor recommended in the two codes. The remainder of the difference is due to the value of ratio of mass energy absorption coefficients of water to air $(\bar{\mu}_{en}/\rho)_{w,a}$. Figure 4.1 shows that the values of $(\bar{\mu}_{en}/\rho)_{w,a}$ given in IAEA TRS 277 [4] are greater than those in ICRU Report 23 [3] by a maximum of 2.5% at 0.17 mmCu HVL.

The difference between the values of $(\bar{\mu}_{en}/\rho)_{w,a}$ given in the two codes is mainly due to the method of averaging the monoenergetic values of the mass energy absorption coefficient over the spectrum at the point of measurement in water. ICRU Report 23 obtained $(\bar{\mu}_{en}/\rho)_{w,a}$ by using an equivalent photon energy. This was defined as the energy of a monoenergetic beam that had the same half value layer (HVL) as the radiation being considered. The effect on the equivalent photon energy due to scattering and filtration at a depth in the water phantom was allowed for using factors given in ICRU Report 10b [28]. The values of $(\bar{\mu}_{en}/\rho)_{w,a}$ given in IAEA TRS 277 were calculated in a two step process. Firstly, the photon fluence spectrum at the reference depth in the phantom was calculated using Monte Carlo techniques based on a typical clinical 'in air' spectrum. Then the monoenergetic values of the mass energy absorption coefficients were averaged over the photon fluence spectrum at the reference depth in water.

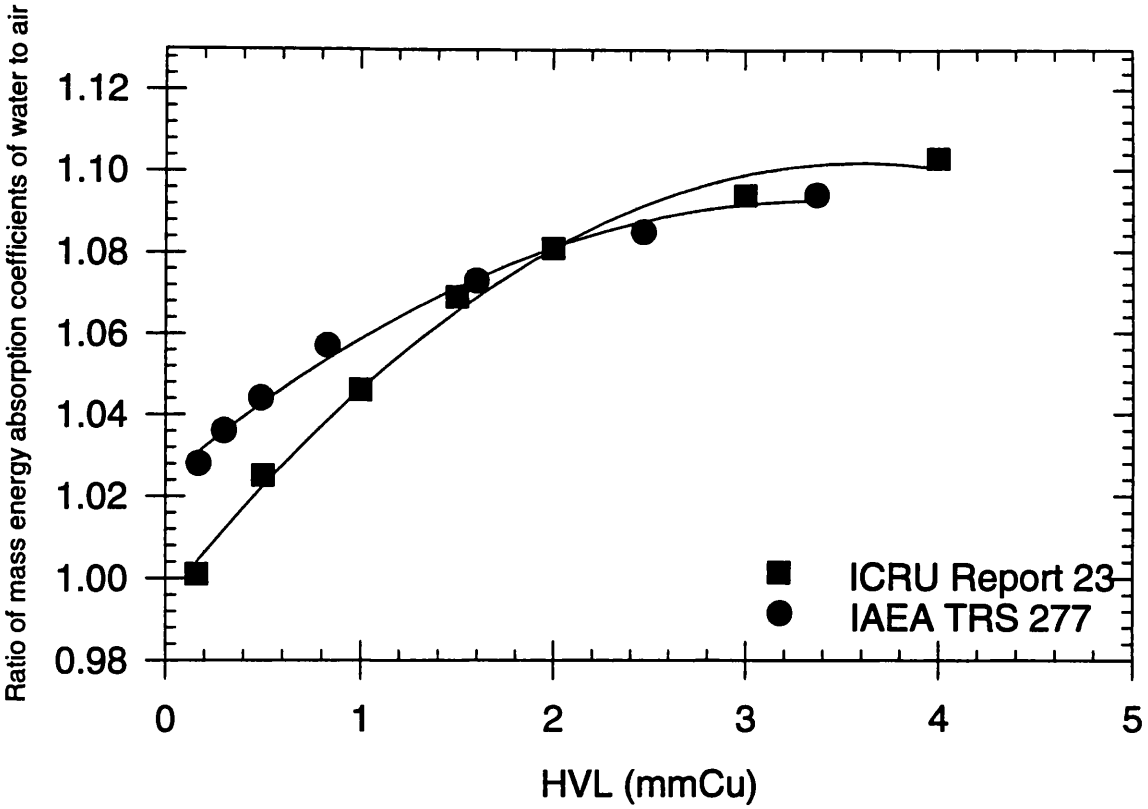

Figure 4.1: Comparison of the ratio of mass energy absorption coefficients of water to air given in ICRU Report 23 and IAEA TRS 277.

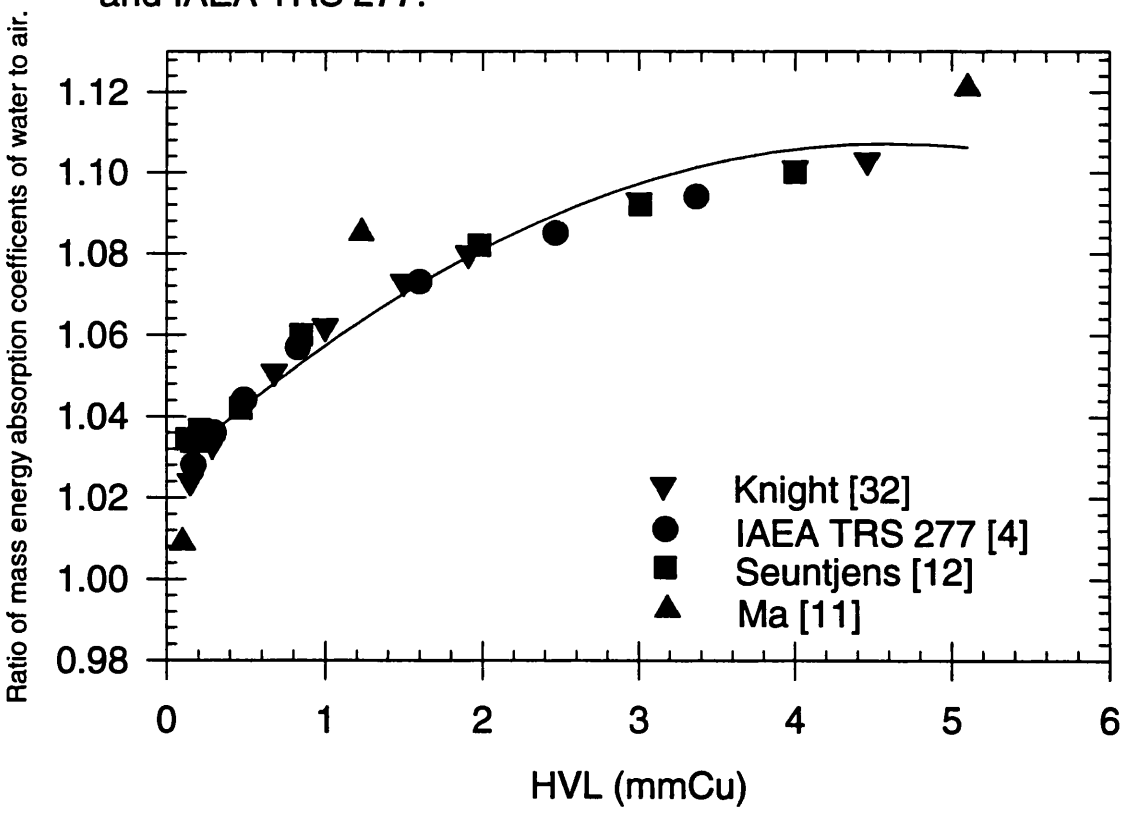

Figure 4.2: Comparison of the ratio of mass energy absorption coefficients of water to air calculated using Monte Carlo techniques.

Another minor difference between the two codes is the values adopted for the monoenergetic mass energy absorption coefficient. IAEA TRS 277 [29] used values given by Hubbell [30] whereas ICRU Report 23 used values given by Berger [31]. The maximum difference between the two sets of monoenergetic values is 1% for energies between 10 keV and 300 keV.

Figure 4.2 shows that recent values of $(\bar{\mu}_{en}/\rho)_{w,a}$ published in the literature support the values given in IAEA TRS 277, except Ma [11] whose value at the lowest energy is closer to that given in ICRU Report 23.

TABLE 4.1 TO SHOW THE DEPENDENCE OF $(\bar{\mu}_{en}/\rho)_{w,a}$ WITH FIELD SIZE AND DEPTH IN A PHANTOM.

Author	Field size	depth in water	comment
ICRU Report 23			for field sizes greater than 10 x 10 cm^2 the difference will be less than 2%.
IAEA TRS 277	11.3 cm diameter	0 to 5 cm	maximum difference 0.5% at 280 kV
Knight and Nahum [34]	0 to 22 cm radius	2 cm	maximum difference 2% at 3 mm Cu HVL
Knight and Nahum [34]	11 cm diameter	0 to 10 cm	maximum difference 0.5% at 3 mm Cu HVL.

The aim of this work is to calculate $(\bar{\mu}_{en}/\rho)_{w,a}$ for the conditions that the ice calorimeter (2 cm deep, in a cylindrical phantom 5.6 cm diameter and 10 cm long) will be used (see chapter 6).

4.2 METHOD OF DETERMINING THE RATIO OF MASS ENERGY ABSORPTION COEFFICIENTS OF WATER TO AIR.

The method adopted in this thesis is similar to that used in IAEA TRS 277 where the ratio of the mean mass energy absorption coefficients of water to air was calculated using:

$$\left(\frac{\bar{\mu}_{en}}{\rho}\right)_{w,a} = \frac{\int_0^E \frac{d\phi}{dE}\left(\frac{\mu_{en}}{\rho}\right)_w E\,dE}{\int_0^E \frac{d\phi}{dE}\left(\frac{\mu_{en}}{\rho}\right)_a E\,dE} \qquad (10)$$

where:

$d\Phi/dE$ is the photon fluence spectrum at a depth in water.

$(\mu_{en}/\rho)_w$ is the monoenergetic value of the mass energy absorption coefficient for water at energy E.

$(\mu_{en}/\rho)_a$ is the monoenergetic value of the mass energy absorption coefficient for air at energy E.

4.2.1 DETERMINATION OF THE PHOTON FLUENCE SPECTRUM AT A DEPTH IN WATER.

The photon fluence spectrum at a depth in water was determined in two stages: Firstly the spectrum in air was measured and then Monte Carlo techniques were used to convert the primary spectrum to that at 2 cm deep in water.

4.2.1.1 MEASUREMENT OF THE IN AIR SPECTRA FOR THE NPL THERAPY LEVEL, MEDIUM ENERGY QUALITIES.

Two X-ray tubes were employed, a Philips 150 tube that operated between 50 and 150 kV, and a Muller tube that operated between 180 and 300 kV. The photon spectra were measured for the six NPL qualities (see Appendix 1) generated between 100 and 280 kV. The intrinsic Ge detector employed in these studies was cylindrical with an active volume of 1500 mm^3 and a thickness of 20 mm, with a 10^{-3} mm thick beryllium window (see figure 4.3). This choice of detector dimensions

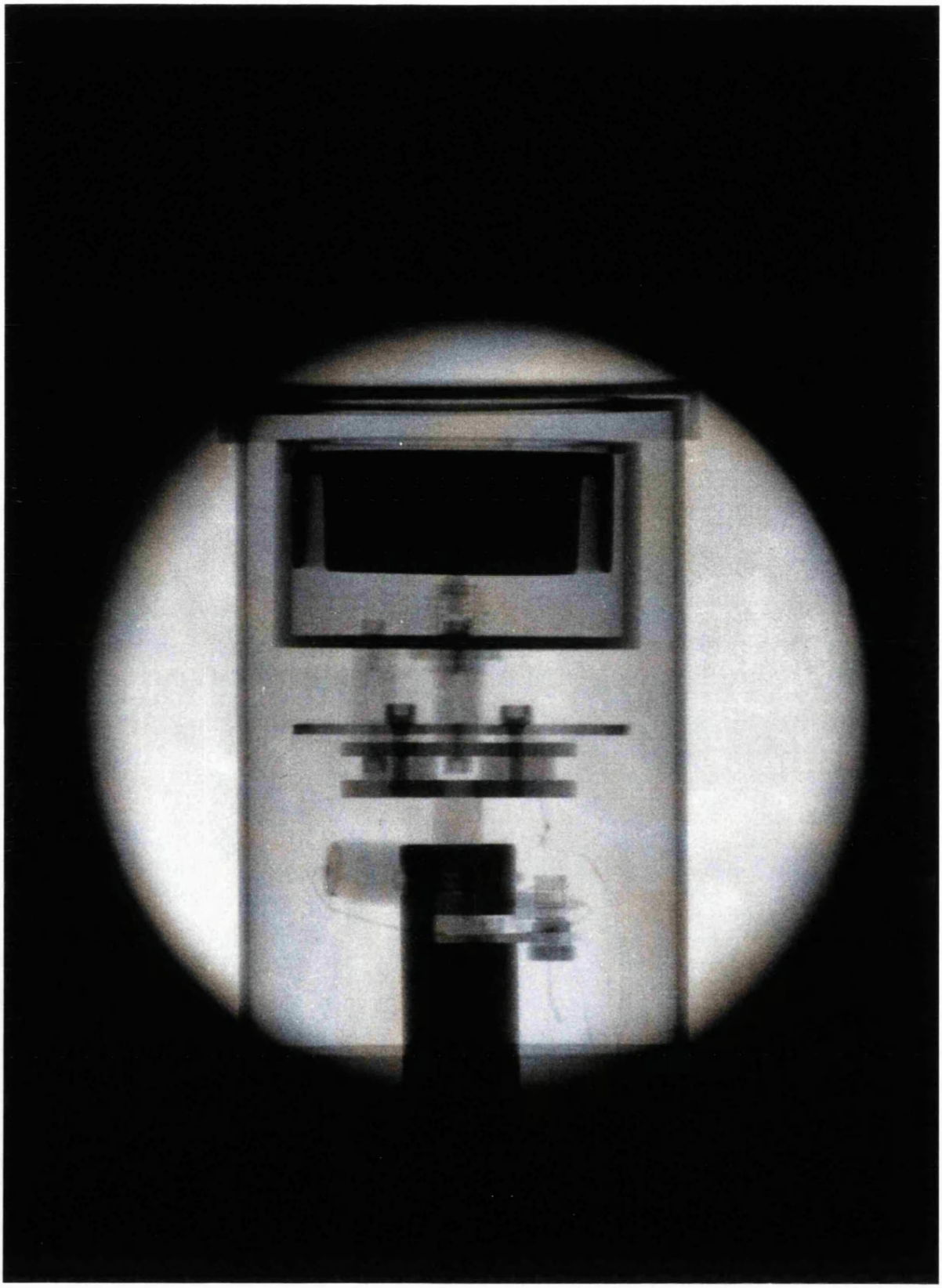

Figure 4.3 Radiograph of the Ge detector.

ensured that most of the collimated energetic photons entering the detector were totally absorbed. The detector output was connected to a multichannel analyser and microcomputer for storage of the measured spectra. The channel number of the spectrometer was calibrated in terms of energy before each measurement by attaching a small radioactive source to the cap of the detector and accumulating the line spectra until the major peak contained 10^4 counts. For X-ray qualities generated up to 180 kV, Co-57 and Am-241 sources were used, for generating potentials greater than 180 kV, the Am-241 was replaced by a Ba-133 source.

The X-ray beam was collimated onto the centre of the Ge detector to reduce pulse pile-up and to ensure maximum energy absorption. Collimation was achieved using three tungsten collimators with apertures 0.75 cm, 1 mm and 2 mm in diameter. All three collimators were mounted on an optical bench with the 0.75 cm aperture nearest the X-ray target and the 2 mm aperture nearest the Ge detector. The Ge detector and collimators were aligned on the beam axis using a telescope and light source. The pulse pile-up was further reduced by operating the X-ray tube at the lowest possible current, approximately 7 μA. The distance from the X-ray target to the Ge detector was 2.3 m for X-ray qualities generated up to 180 kV, for higher energies this distance was increased to approximately 5 m to reduce the pulse pile-up.

4.2.1.2 STRIPPING PROCEDURE

The measured pulse height distributions do not represent the photon spectra due to the effects of K-escape, Compton scattering and inefficient photon absorption. The pulse height spectrum was therefore converted to the radiation spectrum by a process known as stripping. This was performed using the NSTRIP program [33] on a Micro Vax 2 computer. In this program the pulse height distribution may be represented by a matrix P, where each element indicates the number of pulses within a certain pulse height interval. The unknown radiation spectrum may in an analogous way be represented as another matrix N, where the relationship between P and N is:

$$P = N \times M \quad (11)$$

Where M is the response matrix of the detector, which is dependent on energy. Therefore, the unknown radiation spectrum can be found by:

$$N = M^{-1} \times P \quad (12)$$

The response function of the intrinsic Ge detector was found using EGS4 Monte Carlo techniques that consisted of a monoenergetic pencil beam of gamma rays impinging on the Ge detector.

In the Monte Carlo calculation of the detector response the photoelectric effect with characteristic x-radiation and Compton scatter was allowed for, while there was no electron transport. The calculation was performed for a total of thirty-two monoenergetic energies between 5 and 500 kV.

4.2.2 COMPARISON OF THE MEASURED SPECTRA WITH THAT PROPOSED BY BIRCH AND MARSHALL.

In 1979 Birch and Marshall [34] proposed a method of computing theoretical X-ray spectra in the range 30-150 kV generating potential. Spectra may be computed by this method for any desired filtration, target angle and generating potential.

The spectra were calculated for the conditions at NPL (see Appendix 1) where the target angle was 22°.

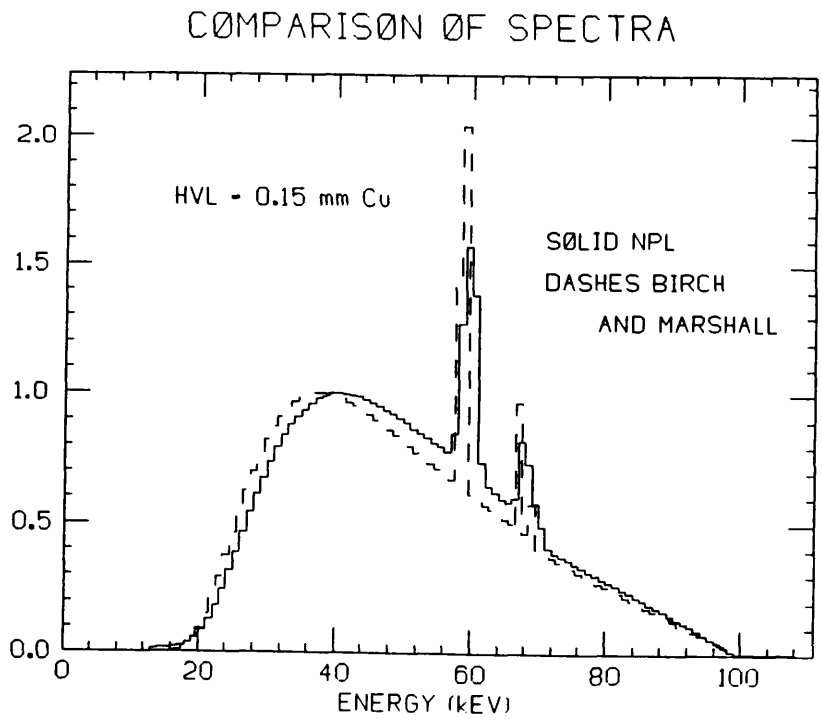

Figure 4.4a Comparison of measured NPL and computed Birch and Marshall spectra for X-rays generated at 100 kV.

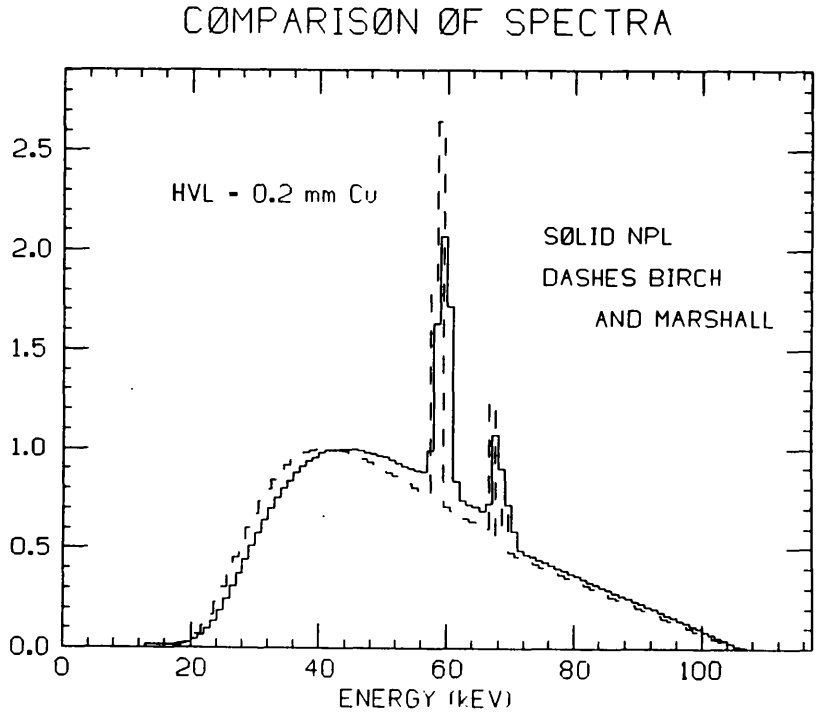

Figure 4.4b Comparison of measured NPL and computed Birch and Marshall spectra for X-rays generated at 105 kV.

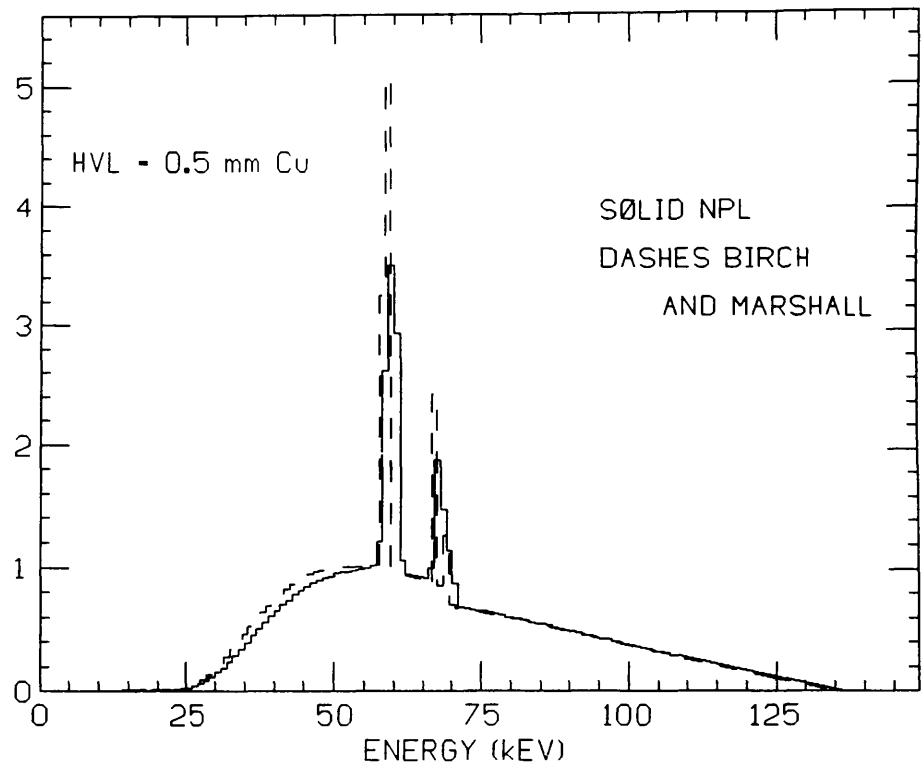

Figure 4.4c Comparison of measured NPL and computed Birch and Marshall spectra for X-rays generated at 135 kV.

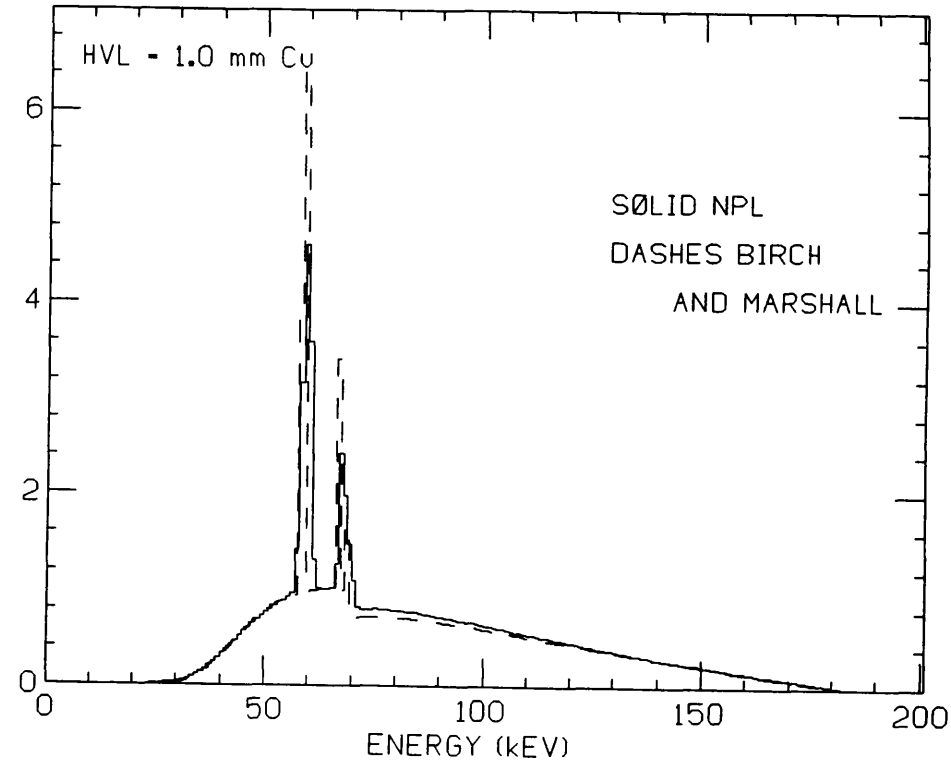

Figure 4.4d Comparison of measured NPL and computed Birch and Marshall spectra for X-rays generated at 180 kV.

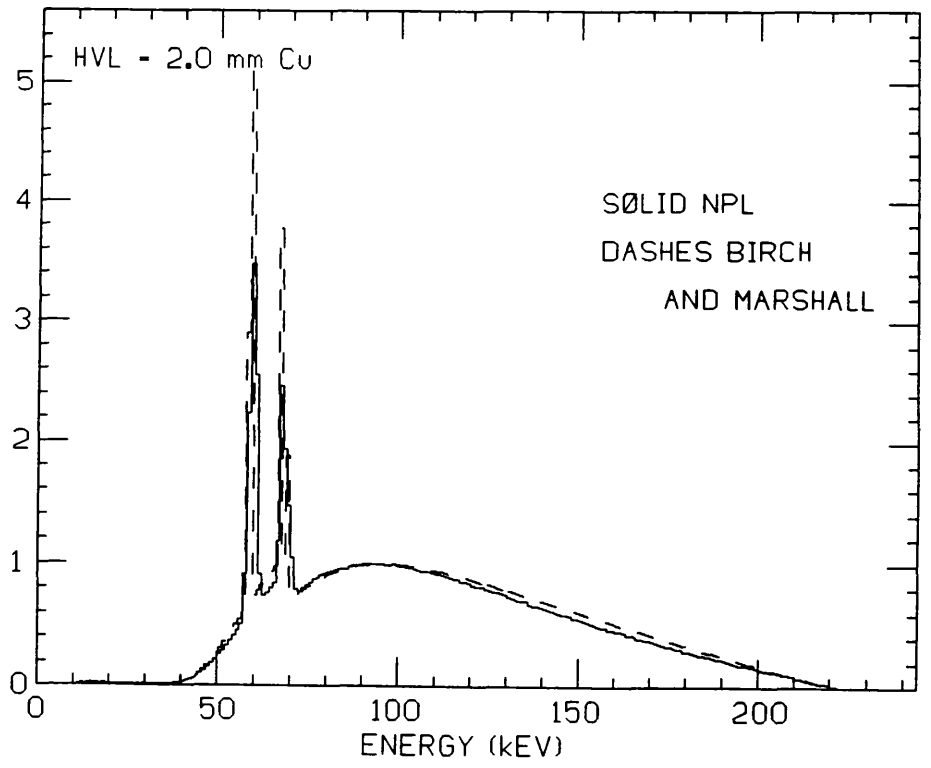

Figure 4.4e Comparison of measured NPL and computed Birch and Marshall spectra for X-rays generated at 220 kV.

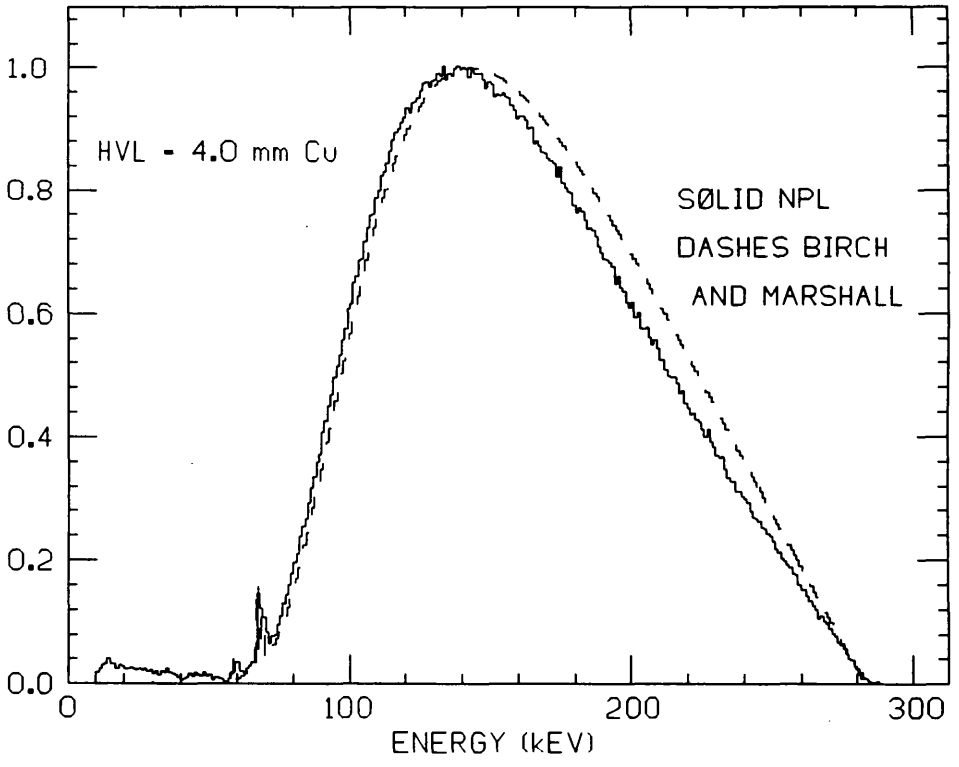

Figure 4.4f Comparison of measured NPL and computed Birch and Marshall spectra for X-rays generated at 280 kV.

4.2.2.1 DISCUSSION

In figures 4.4a to 4.4f the spectra have been calculated for the medium energy X-ray qualities at NPL and are normalized to the peak of the bremsstrahlung spectrum. In general the measured and calculated spectra agree; however, there are some features to be noted. For HVLs below 0.5 mm Cu the Birch and Marshall intensity is greater than the measured intensity below the peak of the bremsstrahlung spectra and less than the measured above the peak. This trend is reversed at 4 mm Cu HVL.The HVLs calculated from the NPL measured spectra and Birch and Marshall spectra agree within the experimental uncertainty except at 4 mm Cu HVL where they differ by 2.5%.

4.2.3 DETERMINATION OF THE SPECTRA AT A DEPTH IN WATER

The photon fluence spectra at a depth in a water phantom were calculated on a Meiko computing surface that consists of 23 floating point transputers. The Monte Carlo computer code system 'Electron Gamma Shower' version 4 (EGS4 [35]) was employed. This Monte Carlo code transports photons and charged particles in random steps until they fall below a cut off energy (ECUT and/or PCUT) or reach a boundary where they may be transported across or discarded. EGS4 Monte Carlo code takes into account the photoelectric effect and Compton scatter; there is also an option to include Rayleigh scatter for medium energy X-rays. The transport of electrons or photons can be simulated in any element, compound or mixture, using the data preparation package PEGS4. The fluence calculations were performed with EGS4 user code FLURZ. FLURZ scores the electron and photon fluence as the sum of track lengths divided by the volume in energy bins, in right cylindrical geometry [36].

As an initial check of the methodology used in this thesis, the geometry given in IAEA TRS 277 (see Table 4.2) was simulated for X-rays generated at 100 kV, for 10^7 histories. The electron transport in EGS4 was turned off by setting ECUT (electron cut off energy) to 1.511 MeV and the photon cut off energy (PCUT) was set to 1 keV.

TABLE 4.2 GEOMETRY USED IN IAEA TRS 277.

Condition	Value
field size at the detector	10 x 10 cm
depth in water	5 cm
phantom size	30 x 30 cm
source to surface distance	1 m

The IAEA 'in air' spectrum was not available so the Birch and Marshall [34] model was employed to generate the appropriate spectrum. This was done by fixing the X-ray generating potential and added filtration to match those given in IAEA TRS 277 and adjusting the target angle to give the required HVL. The resulting spectrum was then used as the input to the Monte Carlo code. The calculated value of $(\bar{\mu}_{en}/\rho)_{w,a}$ agreed with that given in IAEA TRS 277 within 0.1%.

The values of $(\bar{\mu}_{en}/\rho)_{w,a}$ were then calculated for the NPL ice calorimeter geometry and NPL spectra (see Appendix 1), for approximately 10^7 histories.

4.2.3.1 RESULTS

TABLE 4.3 CALCULATION OF THE RATIO OF MASS ENERGY ABSORPTION COEFFICIENTS OF WATER TO AIR FOR MEDIUM ENERGY X-RAYS.

generating potential	HVL	$(\bar{\mu}_{en}/\rho)_{w,a}$		NPLvalue IAEA value
(kV)	(mmCu)	ice calorimeter geometry	IAEA	
100	0.15	1.030 ± 0.15%	1.028	1.002
105	0.20	1.035 ± 0.17%	1.030	1.005
135	0.50	1.051 ± 0.16%	1.044	1.007
180	1.0	1.069 ± 0.14%	1.061	1.008
220	2.0	1.087 ± 0.06%	1.079	1.007
280	4.0	1.104 ± 0.04%	difficult to extrapolate	-

4.2.3.2 UNCERTAINTY FOR $(\bar{\mu}_{en}/\rho)_{w,a}$

The uncertainties associated with the value of $(\bar{\mu}_{en}/\rho)_{w,a}$ given in Table 4.3, were calculated following recommendations given by Duane [37]. Where 100 spectra were simulated, each spectrum was calculated using a random number generator to pick a number within the uncertainty of the photon fluence given by the Monte Carlo for each energy bin. This energy fluence was then summed over all the energy bins to create a new spectrum. The value of $(\bar{\mu}_{en}/\rho)_{w,a}$ was calculated for each spectrum and the uncertainty was taken as the standard deviation of 100 values.

4.2.3.3 DISCUSSION

The difference between the values of $(\bar{\mu}_{en}/\rho)_{w,a}$ for the ice calorimeter geometry and those given in IAEA TRS 277 is due to either differences in field size, phantom size,

SSD or the 'in air' spectrum. This was investigated for X-rays generated at 180 kV using the EGS4 Monte Carlo code. Initially the ice calorimeter geometry was simulated and then the phantom size was increased to 30 x 30 cm, this reduced the ice value of $(\bar{\mu}_{en}/\rho)_{w,a}$ by 0.16%. The field size was then increased to 10 x 10 cm at 2 cm deep in water, this further reduced the ice calorimetry value of $(\bar{\mu}_{en}/\rho)_{w,a}$ by 0.35%. The remaining 0.23% is assumed to be due to differences in SSD and input spectra.

4.3 CALCULATION OF A DEPTH DOSE CURVE IN WATER.

A depth dose curve in water was calculated using the Monte Carlo code, for X-rays generated at 100 kV as a further check on the methodology used in the calculation of $(\bar{\mu}_{en}/\rho)_{w,a}$. This was done by calculating the spectra at 1 cm intervals between 1 and 7 cm deep in water. From these spectra the absorbed dose to water (D_w) was calculated using:

$$D_w = \Psi \left(\frac{\bar{\mu}_{en}}{\rho} \right)_w \qquad (13)$$

where

Ψ is the energy fluence

$(\bar{\mu}_{en}/\rho)_w$ is the mean mass energy absorption coefficient for water.

This was then compared with depth dose curves measured using a NE2561 ionization chamber (see figure 4.5). The absorbed dose for each depth was normalized to 2 cm deep in water.

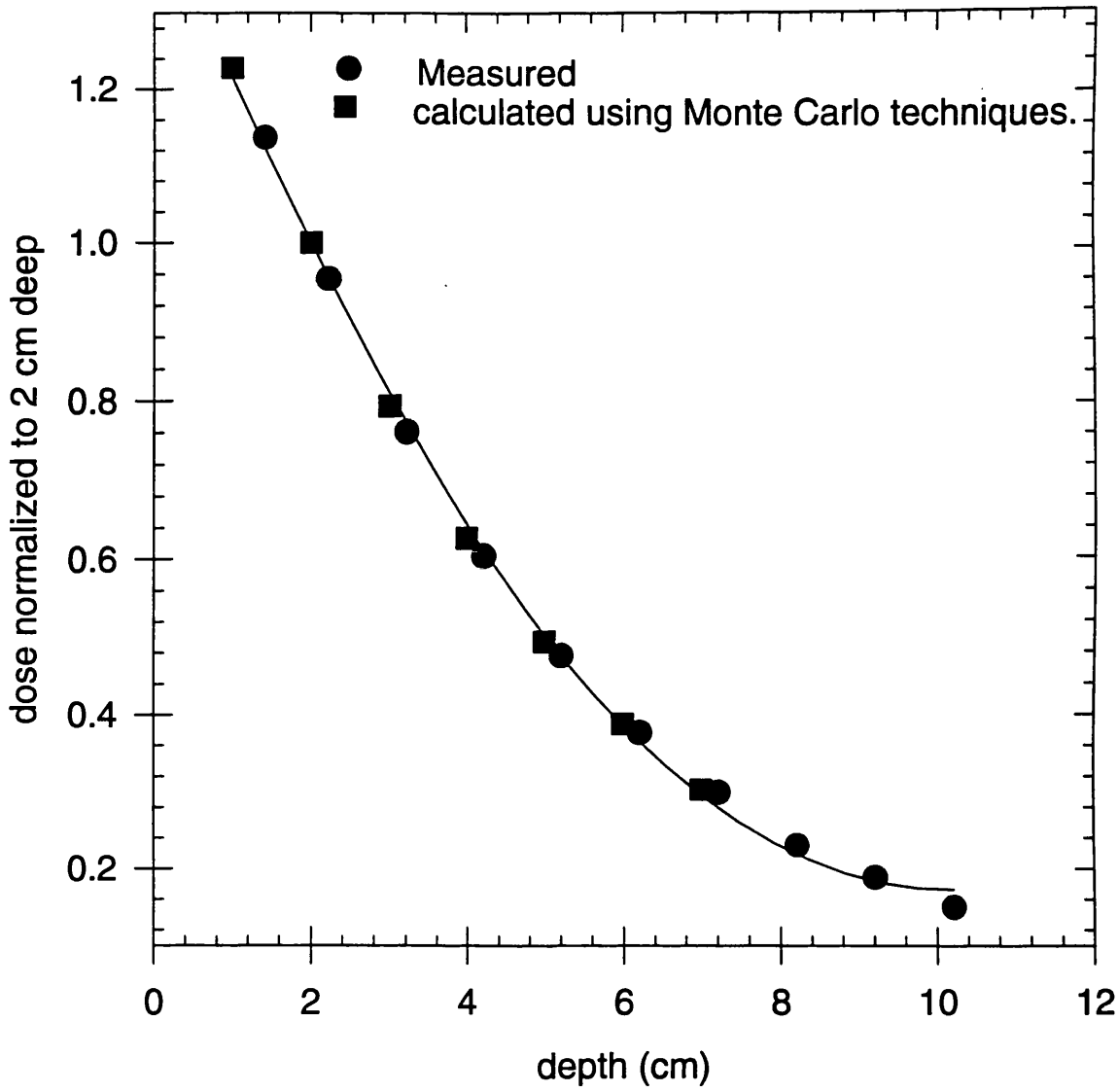

Figure 4.5 Comparison of depth dose curves in water for 0.15 mm Cu HVL, X-rays.

4.3.1 DISCUSSION

Figure 4.5 shows that the depth dose curves measured using a NE2561 ionization chamber agree with the Monte Carlo calculation.

The values of $(\bar{\mu}_{en}/\rho)_{w,a}$ given in IAEA TRS 277 are for 5 cm deep in water whereas the values quoted in this thesis were for 2 cm deep. Therefore the variation of $(\bar{\mu}_{en}/\rho)_{w,a}$ with depth was investigated. It was found that $(\bar{\mu}_{en}/\rho)_{w,a}$ increased from 1.0295 to 1.0326 between 1 and 7 cm deep in water for 100 kV generating potential.

4.4 BEAM QUALITY INDEX FOR MEDIUM ENERGY X-RAYS.

To measure the absorbed dose to water accurately the quality of the X-ray beam must be uniquely defined at the point of measurement in water. The unique method of defining the beam quality is to acquire a detailed knowledge of the photon fluence spectrum at the point of interest in water. However the X-ray spectrum is not a practical quality index as it is not easy to measure at a depth in water. Also if two laboratories have different shaped spectra it is difficult to relate the two in terms of absorbed dose to water.

ICRU Report 23 and IAEA TRS 277 have ignored the necessity of measuring the quality of the beam at the point of measurement in the phantom and instead attempt to specify the beam in air. ICRU Report 23 recommends that for X-rays generated below 400 kV, the half value layer (HVL) is the preferred beam quality index. The HVL is the thickness of an absorber required to attenuate the beam to half the intensity of the incident radiation. However X-rays having a particular HVL may be produced either by light filtration of high voltage radiation or by heavy filtration of low voltage radiation. IAEA TRS 277 has tried to address this problem by characterising the beam by tube potential, total filtration and first half value layer.

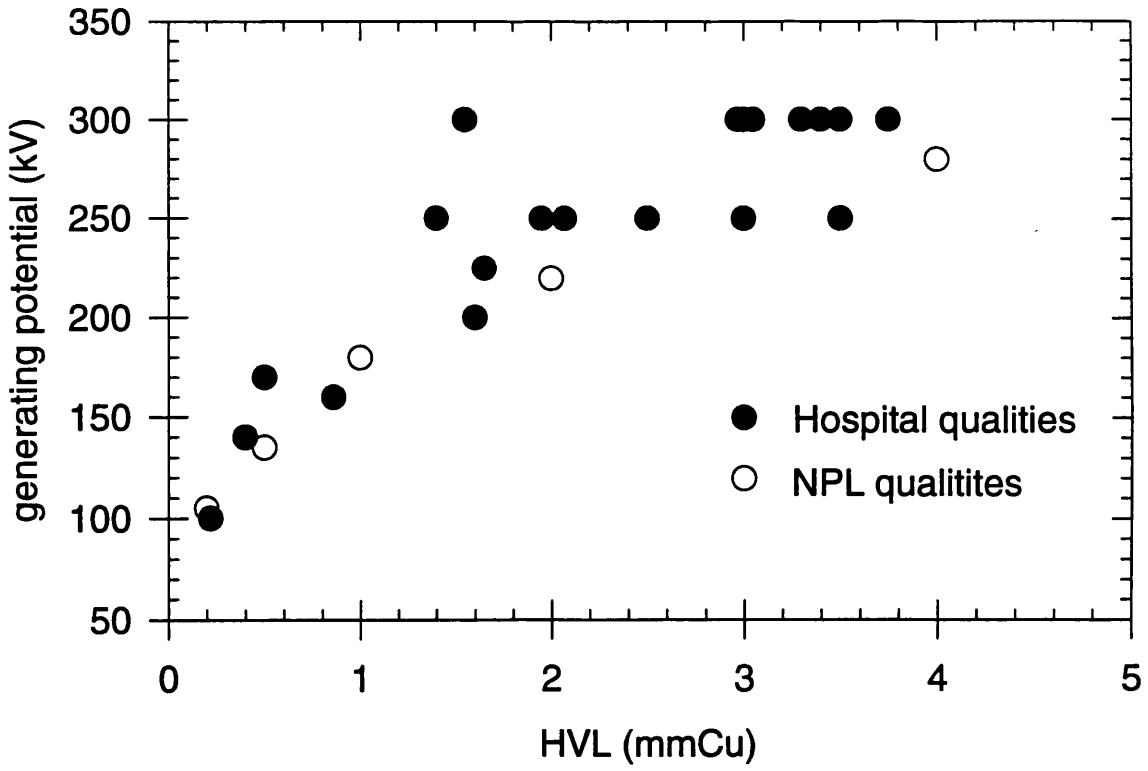

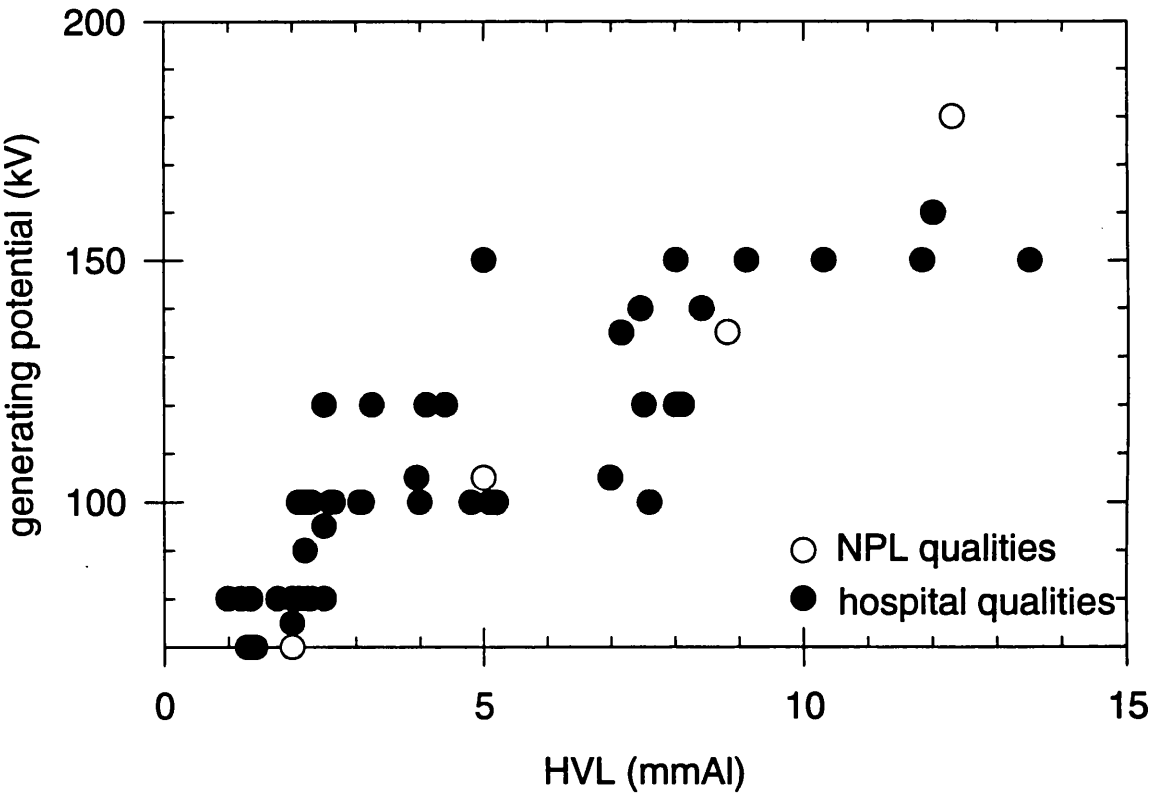

Figure 4.6: To show the variation of HVL with generating potential for 26 radiotherapy centres throughout the U.K.

TABLE 4.4 SPECIFICATION OF X-RAY BEAM QUALITY AT A DEPTH IN WATER.

Author	Radiation	comments
Harrison [38]	diagnostic X-rays	Percentage depth dose in water differed by 25% for X-rays generated at 100 kV and 60 kV having the same HVL.
Clarkson and Mayneored [39]		Used a pair of coaxial ionization chambers that were identical except the inner wall material, one chamber having a copper wall and the other a carbon wall. A ratio reading gave an indication of radiation quality at the site of measurement.
Knight and Nahum [32]	2 mm Al HVL	Investigated the ratio of mass energy absorption coefficients of water to air and found the largest difference was 2% at 2 mmAl HVL for X-rays generated at 50 and 100 kVp.

4.4.1 A BEAM QUALITY INDEX FOR MEDIUM ENERGY X-RAYS.

To assess the variation of the primary in air spectrum for medium energy X-rays throughout the UK a questionnaire was sent to all of the 64 radiotherapy centres, 26 centres replied. Figure 4.6 shows that if the beam quality is represented by generating potential and HVL there is little consensus on the beam qualities adopted for medium energy radiotherapy in the UK. For example a X-ray beam with HVL of 1.6 mmCu can be generated by a potential that varies by 100 kV. The qualities adopted by NPL are approximately the mean value.

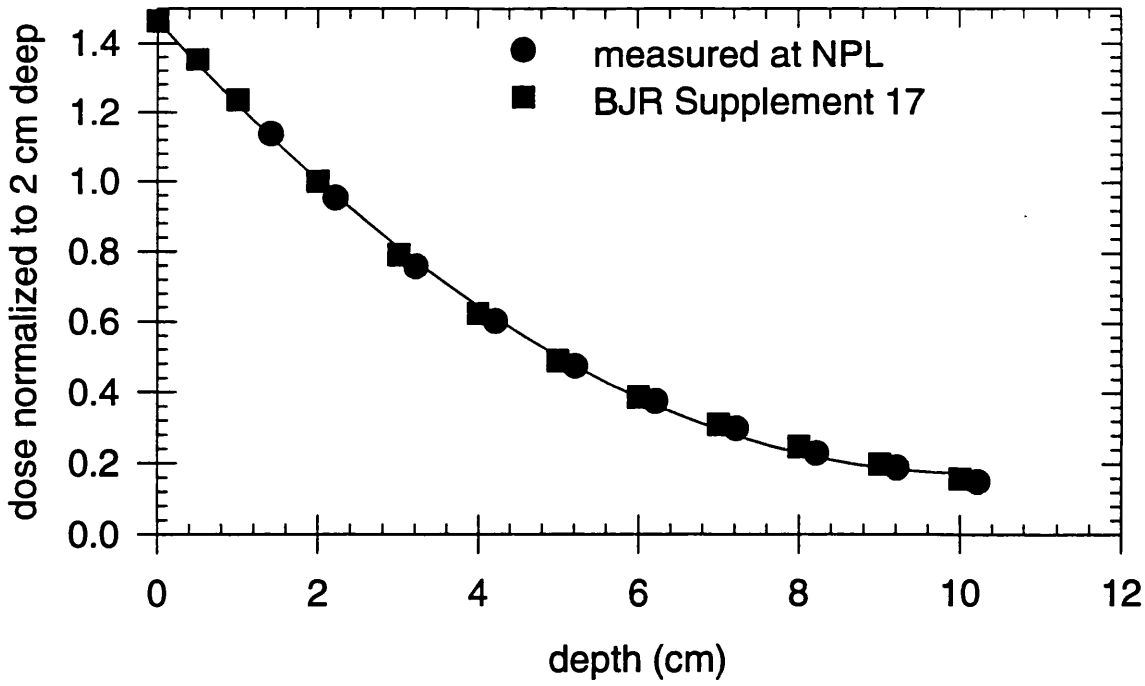

Figure 4.7a: Comparison of the depth dose curves given in BJR Supplement 17 with those measured at NPL for 0.15 mm Cu HVL.

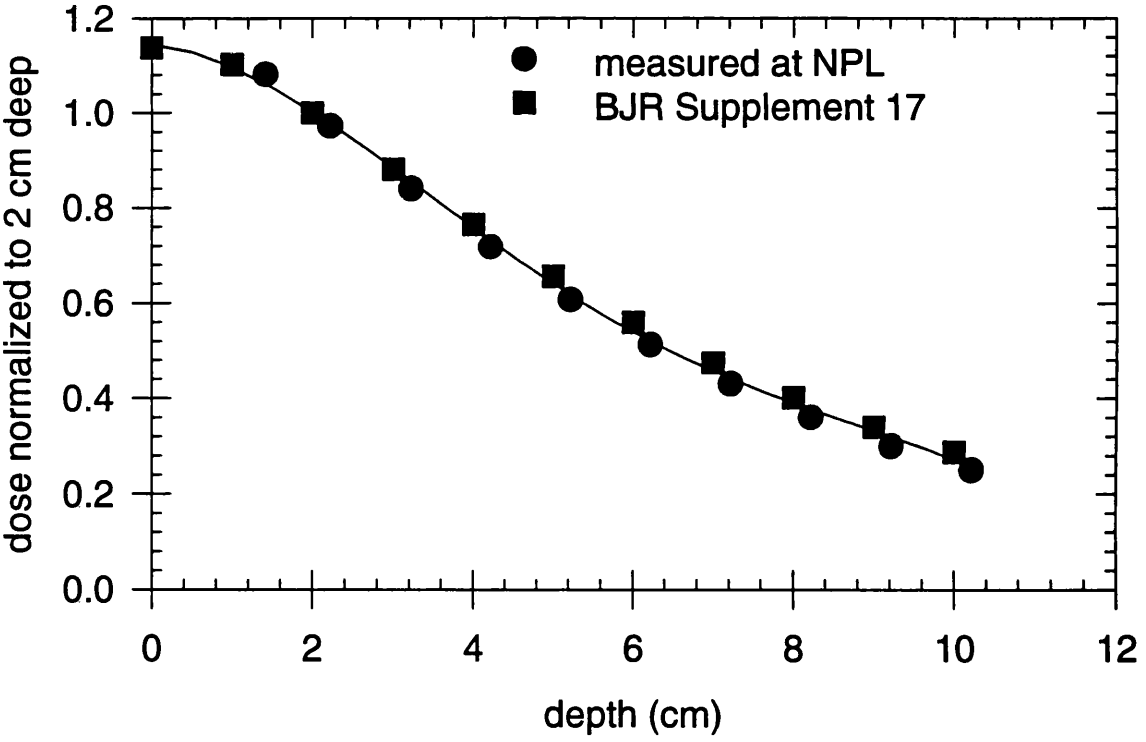

Figure 4.7b: Comparison of the depth dose curves given in BJR Supplement 17 with those measured at NPL for 1 mmCu HVL

The next stage was to investigate the variation of depth dose curves for medium energy X-rays throughout the UK. From the 26 radiotherapy departments surveyed, 19 measured depth dose curves and found them to be consistent with those given in BJR Supplement 17 [40]. Figures 4.7a and 4.7b show that the depth dose curve measured at NPL agree with those given in BJR Supplement 17. A quality index based on the slope of the depth dose curve and the mean energy of the spectrum was investigated.

4.4.1.1 DETERMINATION OF A QUALITY INDEX FOR MEDIUM ENERGY X-RAYS.

To determine an extreme variation of the spectrum with HVL and generating potential, ten primary X-ray spectra were calculated using the method recommended by Birch and Marshall [34]. All of the spectra were simulated for a tungsten target at an angle of 22°. Four of the spectra were simulated for a generating voltage of 100 kV while the remaining six were for a generating voltage of 280 kV. The inherent filtration matched that of the NPL medium energy X-ray tube (see Appendix 1) while the added filtration was adjusted to match the HVL quoted for the NPL therapy spectra within 0.6%.

TABLE 4.5 SIMULATED SPECTRA

Generating Voltage kV	total filtration (mm)	HVL (mm Cu)
100	2.5 Be + 4.8 Perspex + 3.4 Al	0.15088
100	2.5 Be + 4.8 Perspex + 5.14 Al	0.20068
100	2.5 Be + 4.8 Perspex + 23 Al	0.49951
100	2.5 Be + 4.8 Perspex + 128 Al	0.99658
280	1.25 Perspex	0.14990
280	1.82 Perspex	0.19971
280	4.8 Perspex + 0.28 Al	0.50049
280	4.8 Perspex + 4 Al	1.00146
280	4.8 Perspex + 4 Al + 0.54 Cu	2.0049
280	4.8 Perspex + 4 Al + 6 Cu	3.99072

4.4.1.2 CALCULATION OF THE PHOTON FLUENCE SPECTRUM AT A DEPTH IN WATER.

To specify the slope of the depth dose curve, the dose at 2 and 5 cm deep in a water phantom was calculated using the Monte Carlo code EGS4 [35]; similarly to that described in Section 4.2.3 for the incident primary spectra given in Table 4.5. From the calculated spectra the values of the ratio of mass energy absorption coefficients of water to air at 2 cm deep in water were calculated using the same method as described in Section 4.2.

The mean energy at 2 cm deep in water was calculated using:

$$\overline{E} = \frac{\int_0^{Emax} \frac{d\phi}{dE} E \, dE}{\int_0^{Emax} \frac{d\phi}{dE} dE} \qquad (14)$$

$d\Phi/dE$ is the photon fluence spectrum at 2 cm deep in water.

E_{max} is the generating voltage.

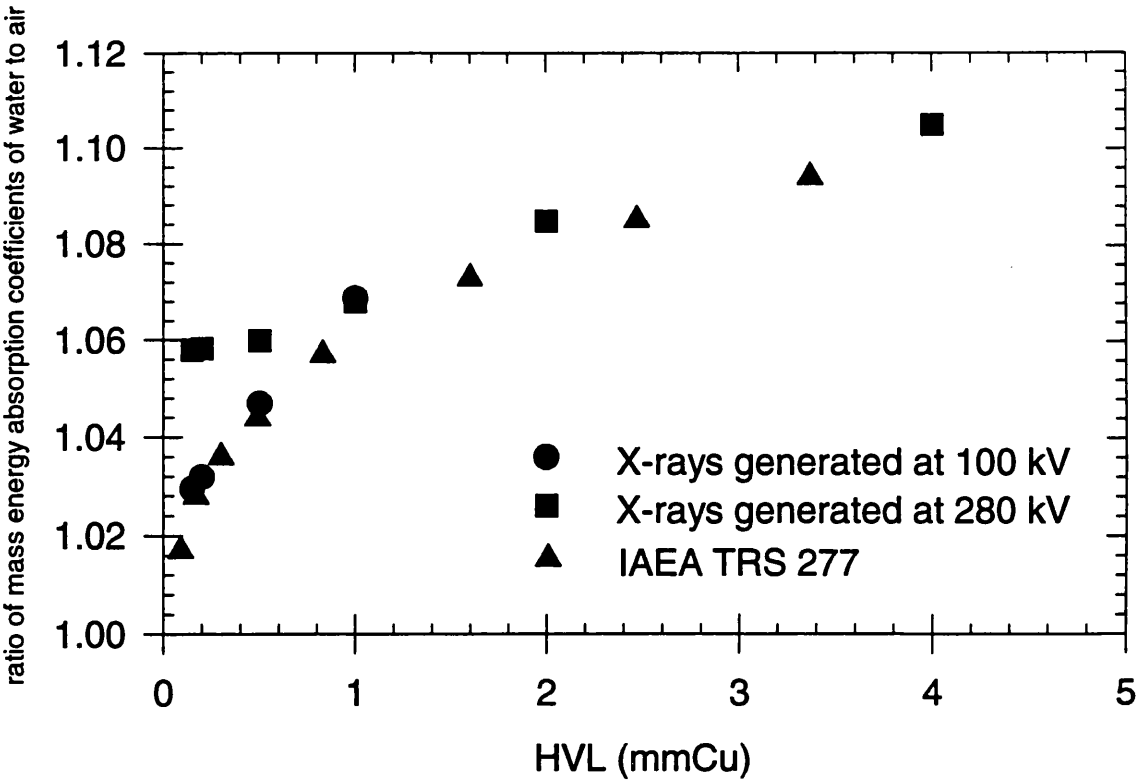

Figure 4.8a: To show the variation of HVL with the ratio of mass energy absorption coefficients of water to air.

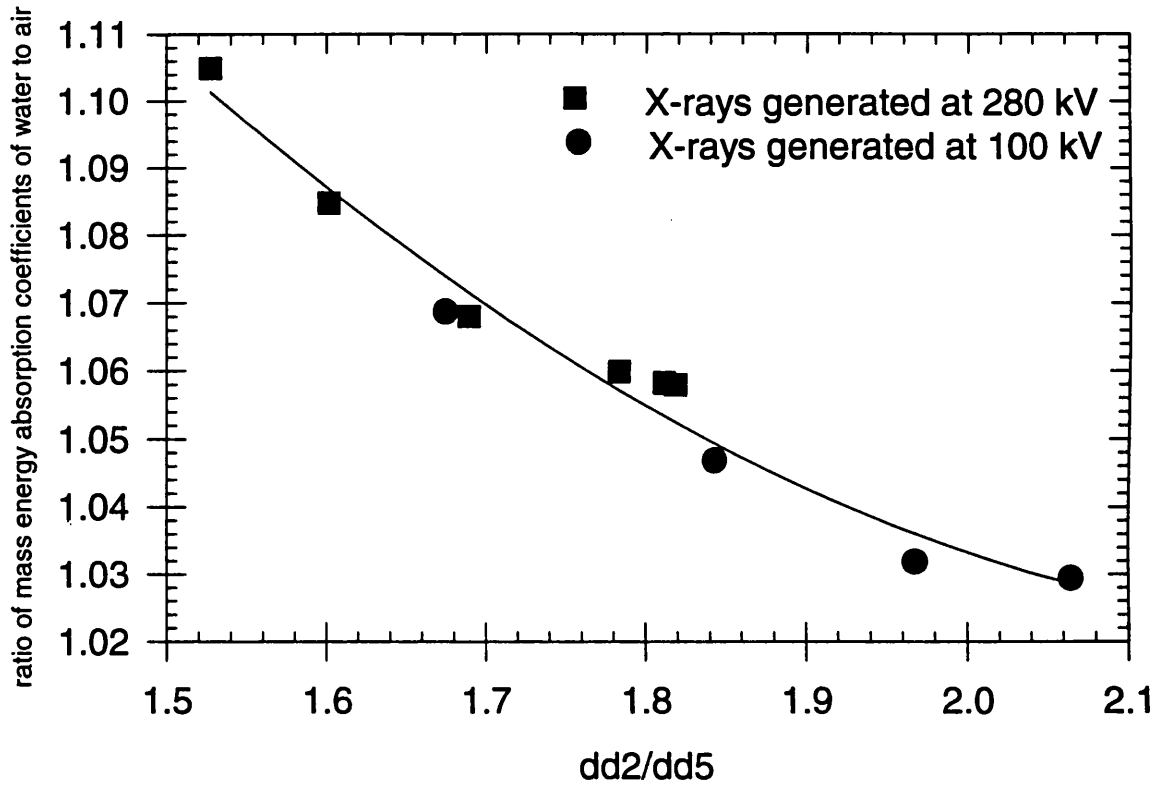

Figure 4.8b: To show the variation of the ratio of the dose at 2 cm to that at 5 cm deep in water (dd2/dd5) with the ratio of mass energy absorption coefficients of water to air.

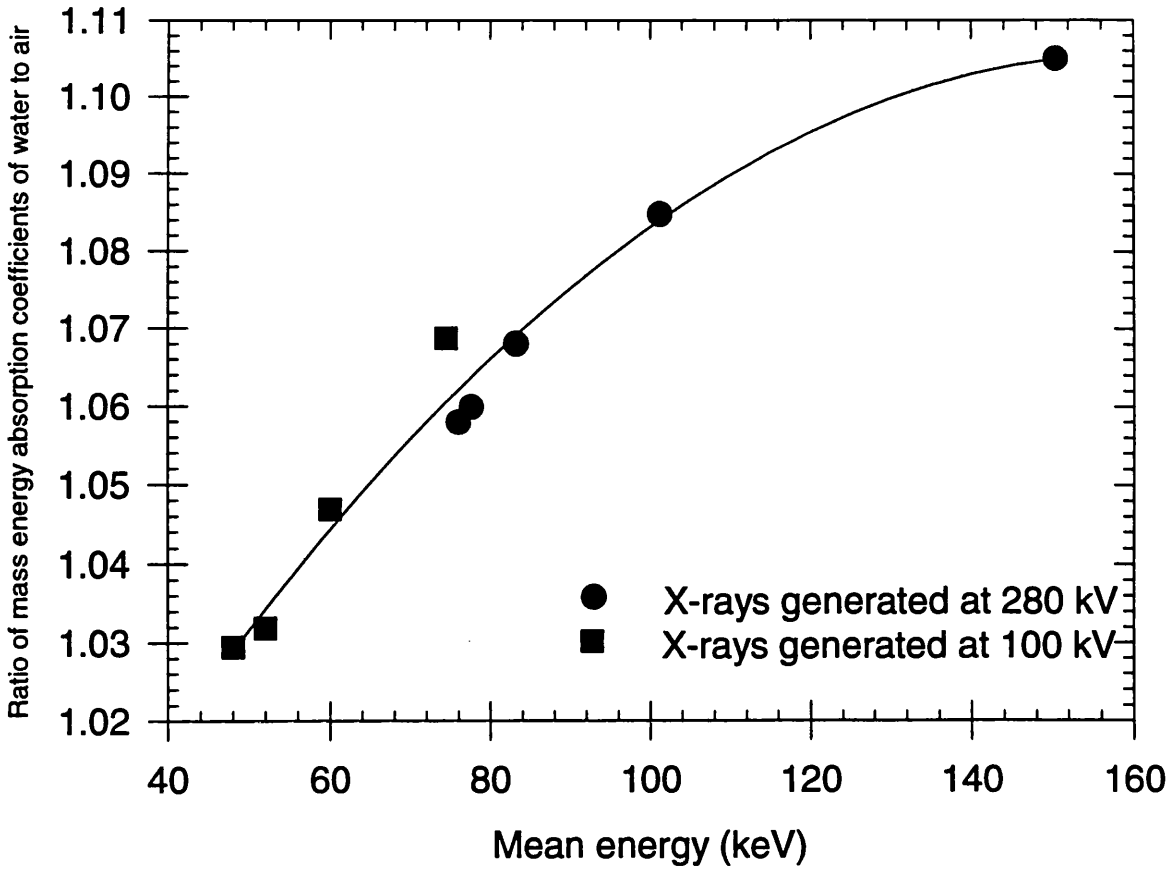

Figure 4.8c: To show the variation of mean energy with the ratio of mass energy absorption coefficients of water to air.

4.4.1.3 DISCUSSION.

Figure 4.8a shows the beam specified in terms of HVL is insufficient for the accurate determination of $(\bar{\mu}_{en}/\rho)_{w,a}$, at the lowest beam quality $(\bar{\mu}_{en}/\rho)_{w,a}$ varies by 3% for a fixed HVL. This is expected as HVL specifies the spectrum in air whereas the absorbed dose to water is measured at 2 cm deep in water. The mean energy of the photon fluence spectrum is not a good beam quality index as it is impractical. Figure 4.8b shows the quality index that best defines $(\bar{\mu}_{en}/\rho)_{w,a}$, is the ratio of dose at 2 and 5 cm deep in water, this is similar to the beam quality used at high energies, the tissue phantom ratio [25].

CHAPTER 5

WATER CALORIMETRY.

5.1 INTRODUCTION.

Absorbed dose to water can be measured directly using a water calorimeter, where the heating effect produced by ionizing radiation is observed. The aim of this chapter is to assess the feasibility of measuring absorbed dose to water accurately using a water calorimeter when irradiated with medium energy X-rays. If this is possible then the absorbed dose to water measured with the water calorimeter will be compared with that using an ionization chamber. The difference between the two methods will be attributed to the chamber correction factor.

5.1.1 BASIC PRINCIPLES OF WATER CALORIMETRY.

For water calorimetry, the relationship between measured temperature rise ($\Delta\theta$), and absorbed dose to water (D_w) is given by:

$$D_w = \frac{c_w \cdot \Delta\theta}{1 - k_{HD}} \qquad (15)$$

where

c_w is the specific heat capacity of water at the operating temperature of the calorimeter,

k_{HD} is the heat defect (see equation 16).

Water calorimetry exploits the low thermal diffusivity of water, which enables the measurement of absorbed dose to water at a point. This assumes that heat transport into and from the point of measurement is negligible for the duration of the measurement. The water calorimeter has the advantage that it does not require energy dependant parameters; such as the energy required to produce an ion pair, chamber correction factor, stopping power ratios, and $(\bar{\mu}_{en}/\rho)_{w,a}$ that may be required for dosimetry using ionization chambers or G-values for Fricke dosimetry.

Unfortunately water calorimeters are relatively insensitive. For example if the specific heat capacity of water is taken as 4200 $Jkg^{-1}K^{-1}$, then an absorbed dose of 1 Gy delivered to the water calorimeter results in a temperature rise of only 0.2 mK. Therefore if an accuracy of 1% is required then a temperature resolution of 2 μK is needed. The other major disadvantage with water calorimetry is that not all the energy absorbed from the radiation results in a temperature rise. Some of the energy imparted by the radiation may change the chemical composition of the water, this is known as the heat defect and will be discussed later in this chapter.

The problems of water calorimetry have appeared insurmountable to some researchers who have resorted to graphite calorimeters [41,42,43,44]. In graphite the temperature rise is about six times that of water and as graphite is elemental it is assumed to have zero heat defect. However, graphite calorimeters possess many disadvantages; such as the high diffusivity of graphite results in the inability to measure at a point, instead the dose must be averaged over a block of graphite known as the core. The core is thermally isolated from the main graphite phantom by gaps. A correction is therefore needed to account for the effects of the gaps being made of non graphite material [45]. The main disadvantage is that a graphite calorimeter measures absorbed dose to graphite and not the required absorbed dose to water. A method is therefore required to convert from absorbed dose in graphite to water [46]. The problems of graphite calorimetry have been addressed by some authors using graphite in water [47] and polystyrene in water calorimeters [48].

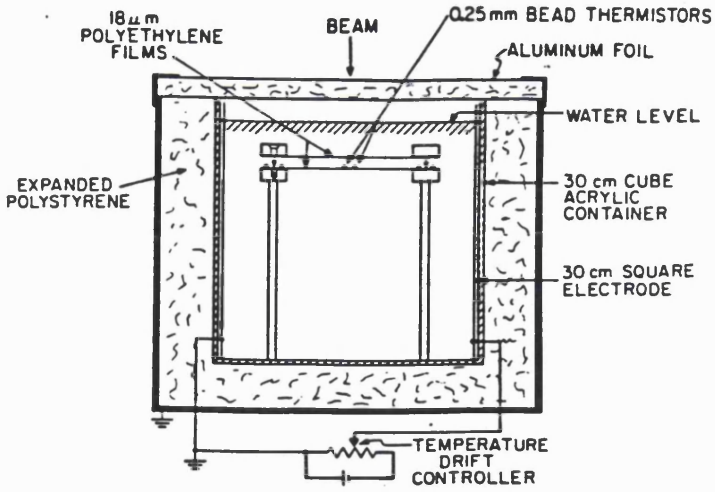

'original' Domen design [49]

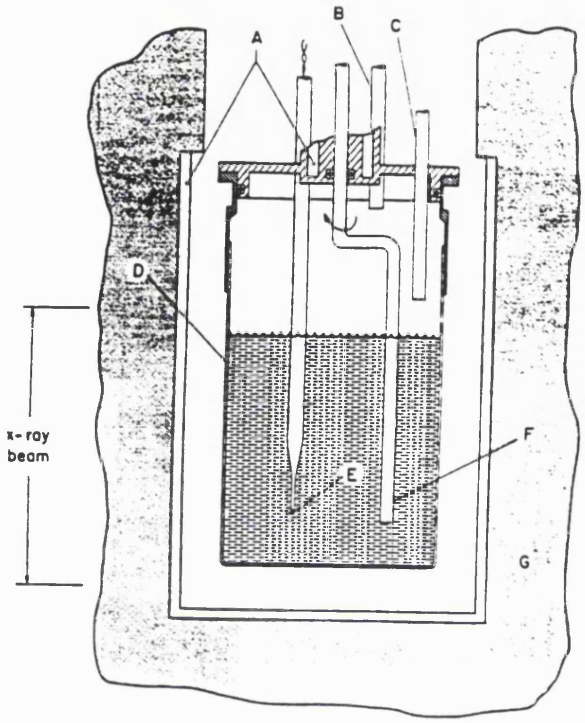

NRCC water calorimeter [51]

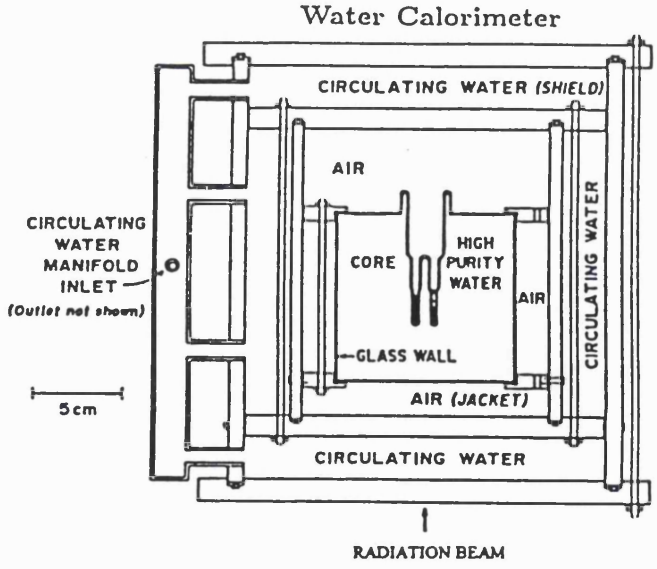

Schultz [50] high purity calorimeter

Figure 5.1: Examples of modern types of water calorimeter.

5.1.2 DESIGN OF WATER CALORIMETERS.

5.1.2.1 INTRODUCTION.

In the literature there have been three basic types of modern water calorimeters, the 'original' Domen calorimeter, the high purity calorimeter and the calorimeter used by the National Research Council of Canada (see figure 5.1).

The basic concept of the water calorimeter operated at the National Research Council of Canada (NRCC) [51] is different from the other calorimeters. The other calorimeters attempt to measure the absorbed dose at a point in the calorimeter. Whereas the water in the NRCC calorimeter is stirred and so measures the mean absorbed dose throughout the calorimeter. The aim of the NRCC is to determine the absorbed dose delivered to Fricke solution, by replacing the calorimeter water with Fricke solution. The main advantage of this design is that convection is not a consideration, but a correction for the heat excess from all non water materials is required. This form of dosimetry would be difficult to adopt at medium energy X-rays because of the high dose (approximately 40 Gy) required by Fricke solution to obtain high accuracy. Also, for medium energy X-rays the G-value for Fricke is not known accurately.

TABLE 5.1 COMPARISON OF DIFFERENT CALORIMETER DESIGNS.

Author	Type of calorimeter	Radiation	Uncertainty on calorimeter measurements (%)
Domen [49]	Original Domen design	^{60}Co gamma rays	0.3-1.1
Mattson [14]	Original Domen design	100 kV X-rays 280 kV X-rays	3.5-4.5 1-2
Kubo [15]	Original Domen design	280 kV having HVL's 0.5 0.625 and 1.7 mmCu	0.65-1.95
Schultz[50]	high purity water saturated with N_2 calorimeter	four photon energies between ^{60}Co and 25 MV	0.2
Seuntjens [12]	high purity water	100 kV ^{60}Co	3 1

5.1.2.2 HEAT FLOW IN A WATER CALORIMETER.

Most designs of water calorimeter rely on heat transport into and away from the point of measurement being negligible: The main modes of transport in a calorimeter are convection and conduction. These will now be discussed when a calorimeter is irradiated with medium energy X-rays.

TABLE 5.2 CONDUCTION OF HEAT IN A WATER CALORIMETER IRRADIATED WITH MEDIUM ENERGY X-RAYS.

Author	Radiation	Dose-rate	heat loss correction due to conduction (%)
Nath and Rothman [52]	250 kV X-rays	500 cGy/min	0.1 (adiabatic boundary conditions) 0.6 (isothermal boundary conditions)
Nath and Rothman [52]	^{60}Co		Negligible
Seuntjens [12]	HVL 0.1mmCu		0.3

5.1.2.3 CONVECTION IN A WATER CALORIMETER.

Rayleigh [53] found that the onset of convection occurs when the rate at which energy is liberated by buoyancy forces exceeds the rate at which energy is dissipated by thermal conduction and viscous damping. Domen initially eliminated convection by irradiating his calorimeter with radiation beams directed vertically downwards. For the horizontal beams used in this project something more imaginative had to be done. For a given geometry and liquid, there will be a critical Rayleigh number such that convection will occur for all values greater than or equal to this number. For simple geometries such as two parallel planes or concentric cylinders the critical value of the Rayleigh number for water is 1000. Domen found that if either the distance between plastic convection barriers [49] or the diameter of the water calorimeter core [54] did not exceed 4 cm then convection would not occur. Another way of preventing convection in a water calorimeter [50,55] is to operate the calorimeter at 4 °C, where the density of the water changes by only 0.006% between 2 and 6 °C. Thus the buoyancy forces and viscous forces will be unaltered over this

temperature range and convection is prevented. The second method of prevention is preferable as it does not require non water materials near the temperature sensor.

5.2 HEAT DEFECT FOR A WATER CALORIMETER

5.2.1 INTRODUCTION.

Ross [56] defined the heat defect (k_{HD}) as:

$$k_{HD} = \frac{E_a - E_h}{E_a} \qquad (16)$$

where:

E_a is the energy absorbed by the irradiated material,

E_h is the energy that appears as heat.

k_{HD} is greater than zero for endothermic processes and less than zero for exothermic processes.

The heat defect is a fundamental problem in all radiation calorimeters and it must be known accurately if a calorimeter is to be a useful dosimetric tool. Ross et al [57] suggested four possible mechanisms that can produce the heat defect; two kinds of radiation induced optical emission, a possible transfer of energy to acoustic modes and radiation induced chemical reactions. The first three were estimated by Ross et al and found to contribute less than 0.1% of the energy absorbed. Ross et al therefore concluded that the most important mechanism causing the heat defect is radiation induced chemical reactions.

The extent of water radiolysis depends on several factors such as type and energy of radiation, absorbed dose, dose-rate, and impurities in the water. The aim of this section is to estimate the value of the heat defect for the water calorimeter used in this project, when irradiated with medium energy X-rays.

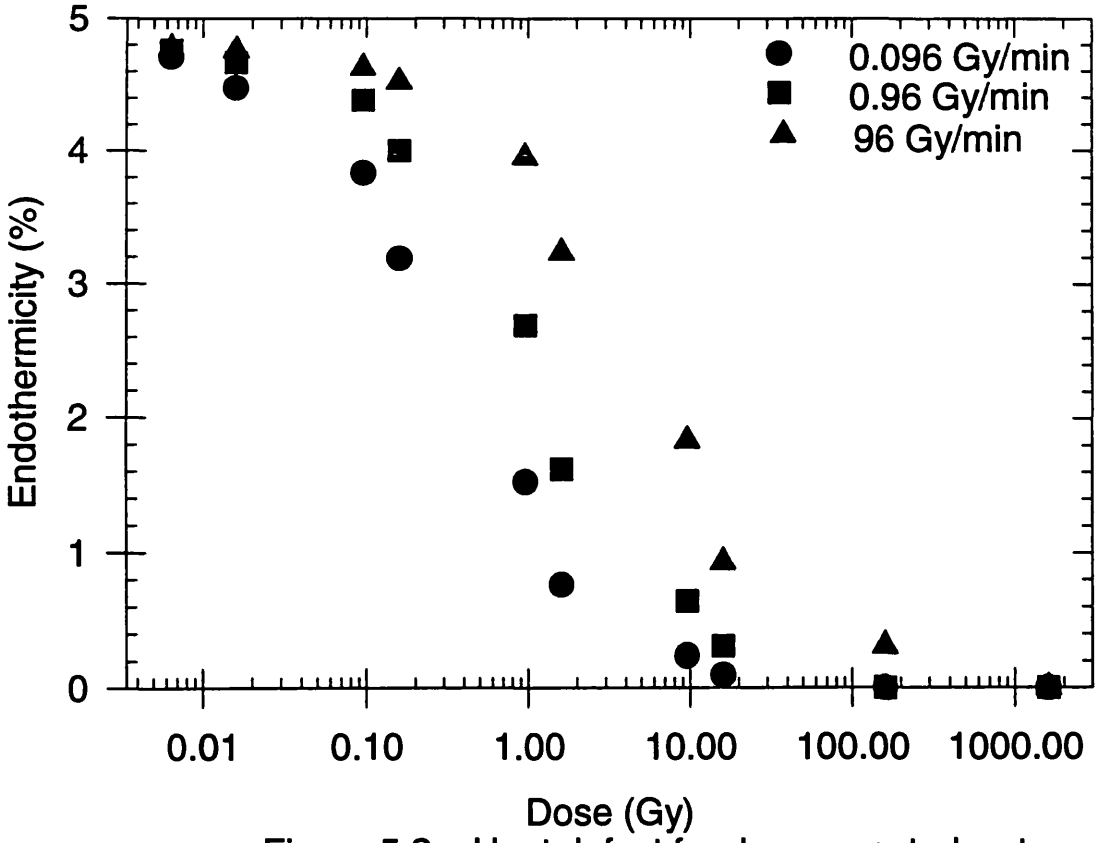

Figure 5.2a: Heat defect for deoxygenated water taken from Fletcher [58]

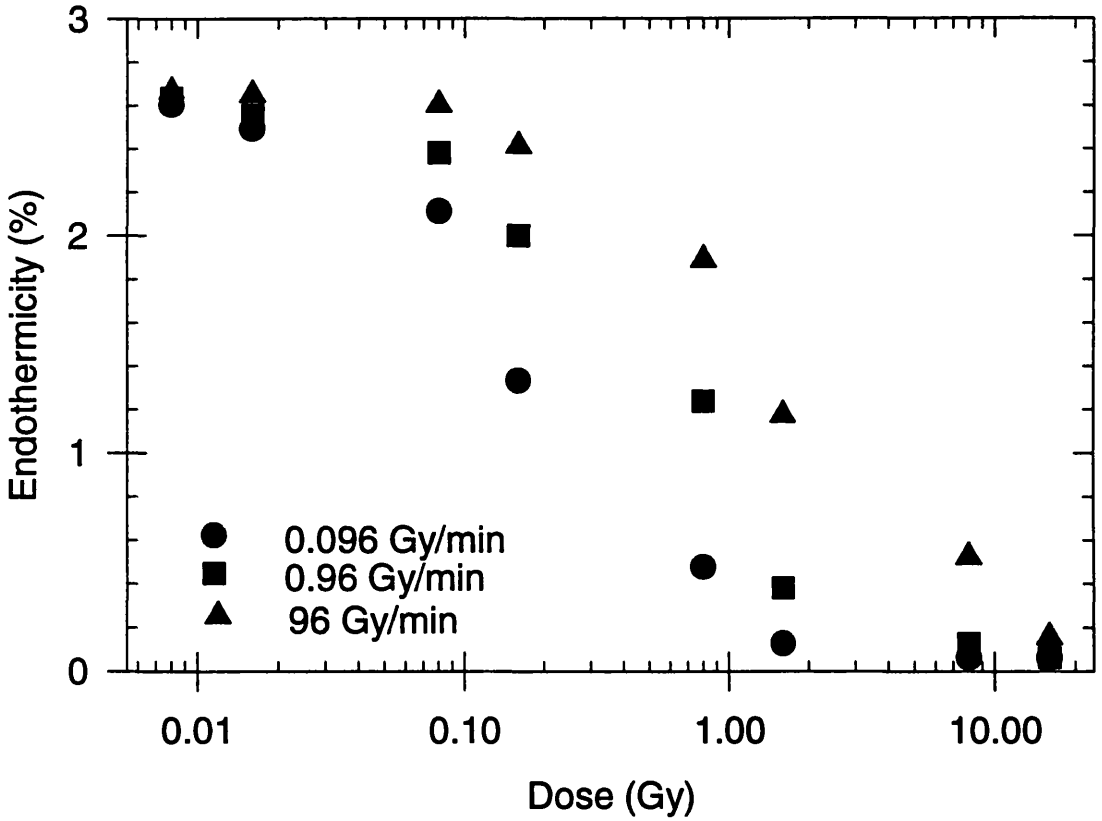

Figure 5.2 b: Heat defect for Hydrogen saturated water taken from Fletcher [58].

5.2.2 REVIEW OF THE LITERATURE.

Figures 5.2a and 5.2b show the variation of the heat defect with accumulated dose for the substances used in modern calorimeters namely, pure water and water saturated with H_2 as given by Fletcher [58].

TABLE 5.3a COMPARISON OF THE HEAT DEFECT FOR WATER SATURATED WITH THE COMMON GASES USED IN WATER CALORIMETRY.

Author	Gas used to saturate water.	Energy	dose-rate (Gy/min)	total dose (Gy)	Method	Heat defect (%)
Domen [54]	H_2	^{60}Co	1.8	1250	calorimetry[a]	0.3
Palmans [62]	H_2	^{60}Co	0.6	595-610	calculated	0
Palmans [62]	pure water saturated with Ar	^{60}Co	0.6	595-610	calculated	-0.05
Ross et al [56]	N_2	20 MV X-rays	24.6	100-500	calculated	0
Ross et al [56]	N_2	20 MV X-rays	24.6	100-500	calorimetry[b]	-0.4±0.3
Schultz et al [50]	N_2	4 MV X-rays	3	6	calorimetry[c]	-0.2±0.4

a. Domen measured the heat defect by comparing the dose measured with H_2 saturated water to that using a graphite and graphite in water calorimeter. The heat defect for the other saturated waters was found by comparison with the H_2 saturated water.

b. Ross et al calculated the heat defect for 50/50 H_2/O_2 water. The heat defect for the other saturated waters was found by comparison with the H_2/O_2 saturated water.

c. Schultz calculated the heat defect by comparing the absorbed dose to water measured using his calorimeter to that using an ionization chamber.

TABLE 5.3b COMPARISON OF THE HEAT DEFECT FOR WATER SATURATED WITH THE COMMON GASES USED IN WATER CALORIMETRY.

Author	Gas used to saturate water.	Energy	dose-rate (Gy/min)	total dose (Gy)	Method	Heat defect (%)
Klassen et al [59]	pure water	LET= 0.2eV/nm	20	8	calculated	0±0.05
Klassen et al [59]	pure water	LET= 0.2eV/nm	1	2	calculated	0±0.05
Selbech [60]	pure water	17-30 KV X-rays		50	total absorption calorimetry	0±0.6
Roos [61]	pure water	1-5 MeV electrons			total absorption calorimetry	0±0.44

a. Domen measured the heat defect by comparing the dose measured with H_2 saturated water to that using a graphite and graphite in water calorimeter. The heat defect for the other saturated waters was found by comparison with the H_2 saturated water.

b. Ross et al calculated the heat defect for 50/50 H_2/O_2 water. The heat defect for the other saturated waters was found by comparison with the H_2/O_2 saturated water.

c. Schultz calculated the heat defect by comparing the absorbed dose to water measured using his calorimeter to that using an ionization chamber.

Tables 5.3a and 5.3b show that there is consensus on the value of the heat defect for the saturated waters commonly used in water calorimetry after an initial dose. This assumes that the system is clean and that there are no air spaces above the water for the gases to escape. Most of the experimental results involve a comparison between different dosimetric techniques, it is reassuring that the heat defect is independent

of the technique. It appears from figure 5.2b that H_2 saturated water has advantages over the other types of water as it leads to zero heat defect with the minimum initial dose.

Klassen et al [63] have discussed the concept of zero heat defect for pure water. When pure water is irradiated, H_2O_2, H_2, and O_2 are produced with G-values that depend on the dose-rate. These stable products do not increase in concentration indefinitely with accumulated dose. Instead they react with the reactive species produced by radiolysis. The rates of these back reactions increase until the production and destruction of the stable products becomes equal, at which point their products cease to change and a stable state is obtained. A stable state is equivalent to a state with zero heat defect.

5.2.3 CALCULATION OF THE HEAT DEFECT

5.2.3.1 RADIOLYSIS OF WATER

Draganic [64] suggested the chain of events that occurs on the absorption of radiation by water, are:

a) *The physical stage* takes place on the shortest time scale about 10^{-15} seconds or less. This involves interactions of the incident quantum with atoms of the medium and results in the production of excited species and secondary particles.

b) *The physicochemical stage* is where energy is deposited along the primary tracks. This involves chemical reactions resulting in the rearrangement of the ions, and the formation of radicals and excited species. The primary products of water at this stage are:

$$H_2O \rightarrow \underbrace{OH + e^-_{aq} + H}_{radical} + \underbrace{H_2O_2 + H_2}_{molecule}$$

where

e^-_{aq} is a hydrated electron,

c) *The chemical stage* commences when the primary species diffuse away from the

point of origin and reacts with solute species. A complete list of these reactions is given in Appendix 3 [58].

5.2.4 CALCULATION OF THE HEAT DEFECT

The heat defect was calculated using a computer programme called Chemsimul [65]. This program translates a sequence of chemical reactions into a set of coupled differential equations. These equations are solved by numerical integration after specifying rate constants, initial concentrations, radiation chemical yields, absorbed dose and duration of irradiation. A complete set of input parameters for the programme is given in Appendix 3. The results are presented as concentrations of radiolytic products at specified times after the start of irradiation.

The heat defect was calculated by summing all species with concentrations greater than 10^{-20} mol/dm^3 (typically H_2O_2, OH^-, H_2O, O_2^-, O_2, H^+ and H_2) after irradiation. For all the calculations it was assumed that the water contained no impurities and was neutral (pH 7). The heat defect was then taken as the percentage of the endo/exo thermisivity (ΣCH) to the total radiation energy absorbed by the system, i.e.

$$K_{HD} = \frac{\Sigma CH}{\kappa} \times 100 \qquad (18)$$

where

κ is the total radiation energy absorbed by the water

C is the concentration of the species in mol/dm^3,

H is the heat of formation in k/mol.

5.2.5 COMPARISON WITH ROSS ET AL.

To check the calculation of the heat defect the conditions given by Ross et al[56] were simulated. Their water calorimeter consisted of a small sealed vessel

containing 10 ml of de-oxygenated stirred water, saturated with various gases. It was irradiated with 20 MV X-rays at a dose-rate of 0.4 Gys^{-1}.

TABLE 5.4 COMPARISON OF HEAT DEFECTS.

Type of water	Endothermic heat defect (%)	
	Ross et al[56]	This thesis
Air saturated	2.1	2.2
1.4 mM O_2	2.1	2.2
0.85 mM H_2	0	0.08

5.2.6 HEAT DEFECT FOR MEDIUM ENERGY X-RAYS.

Most of the papers mentioned in Table 5.3a and 5.3b are for calorimeters irradiated with ^{60}Co gamma rays and photons with higher energies. There is a change in the LET of the radiation from 0.29 eV/nm at ^{60}Co to 1.7 eV/nm for X-rays generated at 200 kV (see Table 5.5), which may result in a change in heat defect.

It has been suggested that this can be explained in terms of spurs [66]. The cluster of ionized and excited species produced by the radiolysis of water are called spurs, blobs or short tracks if the energy per cluster is from 6 to 100 eV, 100 to 500 eV or 500 to 5000 eV, respectively. For low LET radiation, about 70% of the energy is deposited in spurs. In water the primary spur products are highly reactive but some escape from the region of the spur before reacting. Others may undergo reactions within the spur to give rise to stable products that diffuse throughout the liquid. The spur reactions depend on the linear energy transfer (LET) of the ionizing radiation. As the LET increases, adjacent spurs begin to overlap so that reactions within the spurs become important and the G-value will change.

TABLE 5.5 LINEAR ENERGY TRANSFER FOR VARIOUS TYPES OF RADIATION [67]

Radiation	LET_{Δ} (eV/nm) Δ=100 eV
^{60}Co	0.29
22 MV X-rays	0.19
2 MeV electrons	0.2
200 kV X-rays	1.7
H^3 β-rays	4.7
50 kV X-rays	6.3
5.3 MeV α-rays	4.3

Unfortunately the data on the variation of G-values with LET between 0.29 and 1.7 eV/nm is sparse. Yamaguchi [68] gives the variation of G-values with energy for e^-_{aq}, H, H^+, OH, OH^-, H_2O_2 and H_2. However, in this paper mass and charge are not conserved making this data useless for the present purposes. Klassen and Ross [69] give G-values for Intermediate (30 eV/nm) and High (300 eV/nm) LET radiations. These were then simulated using Chemsimul for a total dose of 4 Gy at 1 Gy/min and 0.3 Gy/min and the results are shown in Figure 5.3.

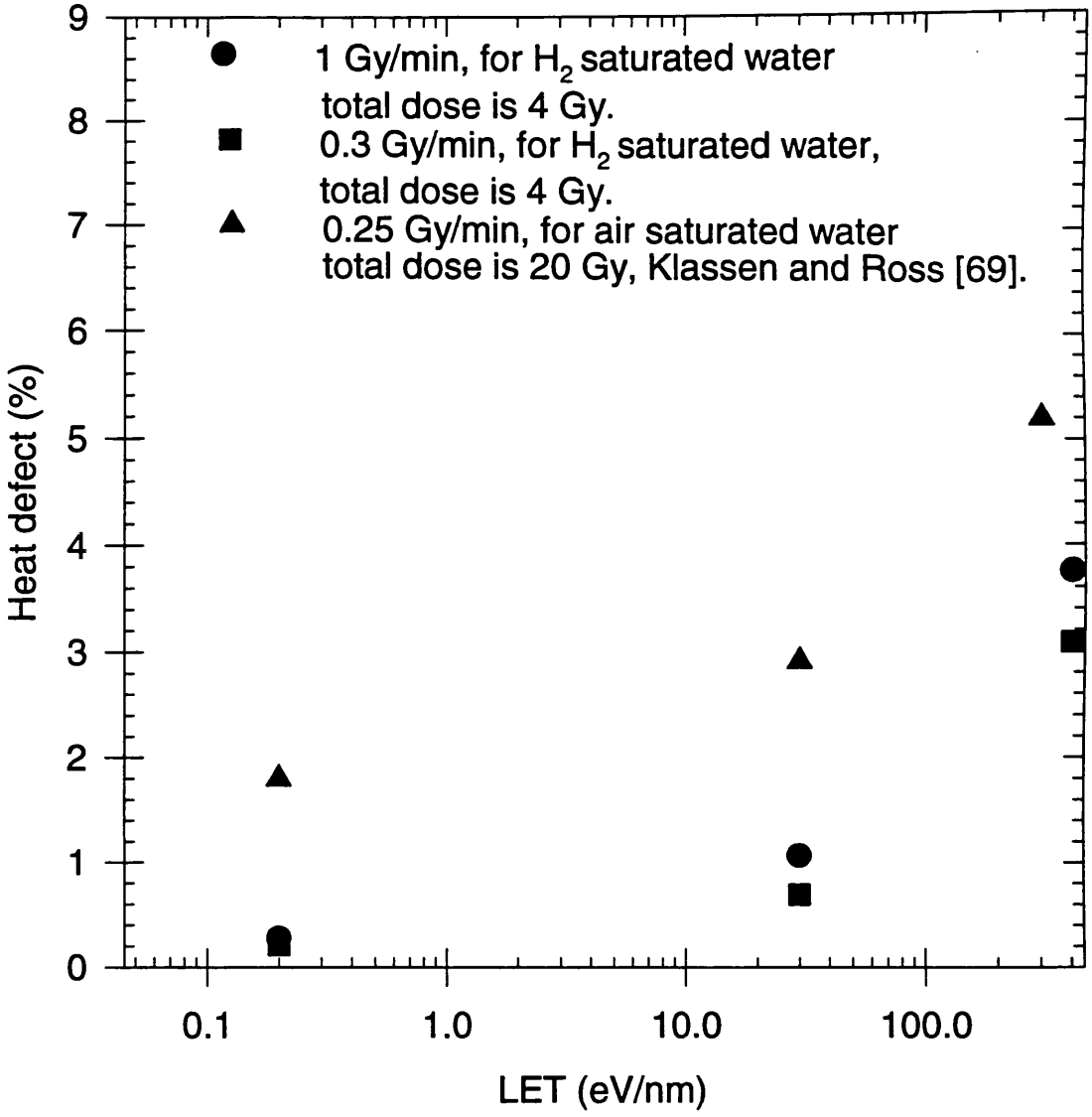

Figure 5.3: Variation of the heat defect with LET.

5.3 DESIGN OF THE WATER CALORIMETER USED IN THIS THESIS.

Four criteria had to be specified before the calorimeter vessel could be designed. Firstly the depth at which a temperature sensor should be positioned in the water. It was apparent from the steep depth dose curves for medium energy X-rays that the temperature probe needs to be positioned accurately and to be as near to the surface as possible to maximize the dose. An ionization chamber will eventually be compared with the calorimeter, this will involve the temperature sensor being replaced with an ionization chamber. For the horizontal X-ray beams employed at NPL the most practical depth is 2 cm, ensuring that the ionization chamber does not touch the front face of the calorimeter vessel.

Secondly the diameter of the calorimeter vessel perpendicular to the X-ray beam axis had to be determined. This was a compromise between having a vessel wholly in the beam to irradiate the water uniformly and having a vessel with the walls outside the beam. In the first case there is the problem of the glass conducting heat to the water (glass has a specific heat of about 0.8 $Jkg^{-1}K^{-1}$, with a temperature rise 5 times that of the surrounding water). Whereas in the latter case there are problems of heat flow within the water due to its non-uniform irradiation and it is not clear what effect the unirradiated water will have on the radiolysis of the irradiated water. It was decided that the diameter of the vessel should be equal to the full width half height of the beam intensity profile i.e. 57.6 mm.

Thirdly the front face of the vessel must be as thin as possible to reduce attenuation of the beam and reduce the amount of heat conducted from the front face to the thermistor. The back wall must be as far away as is practical from the thermistor. The final criterion is that the vessel must be watertight so that there are no air volumes that could influence the heat defect.

Figure 5.4 shows the final design of the water calorimeter used in this thesis. The front face consisted of a 0.2 mm thick microscope slide held on with surface tension. The main difficulty with this vessel is the large amount of glass around the thermistor probe that may conduct additional heat to the thermistor.

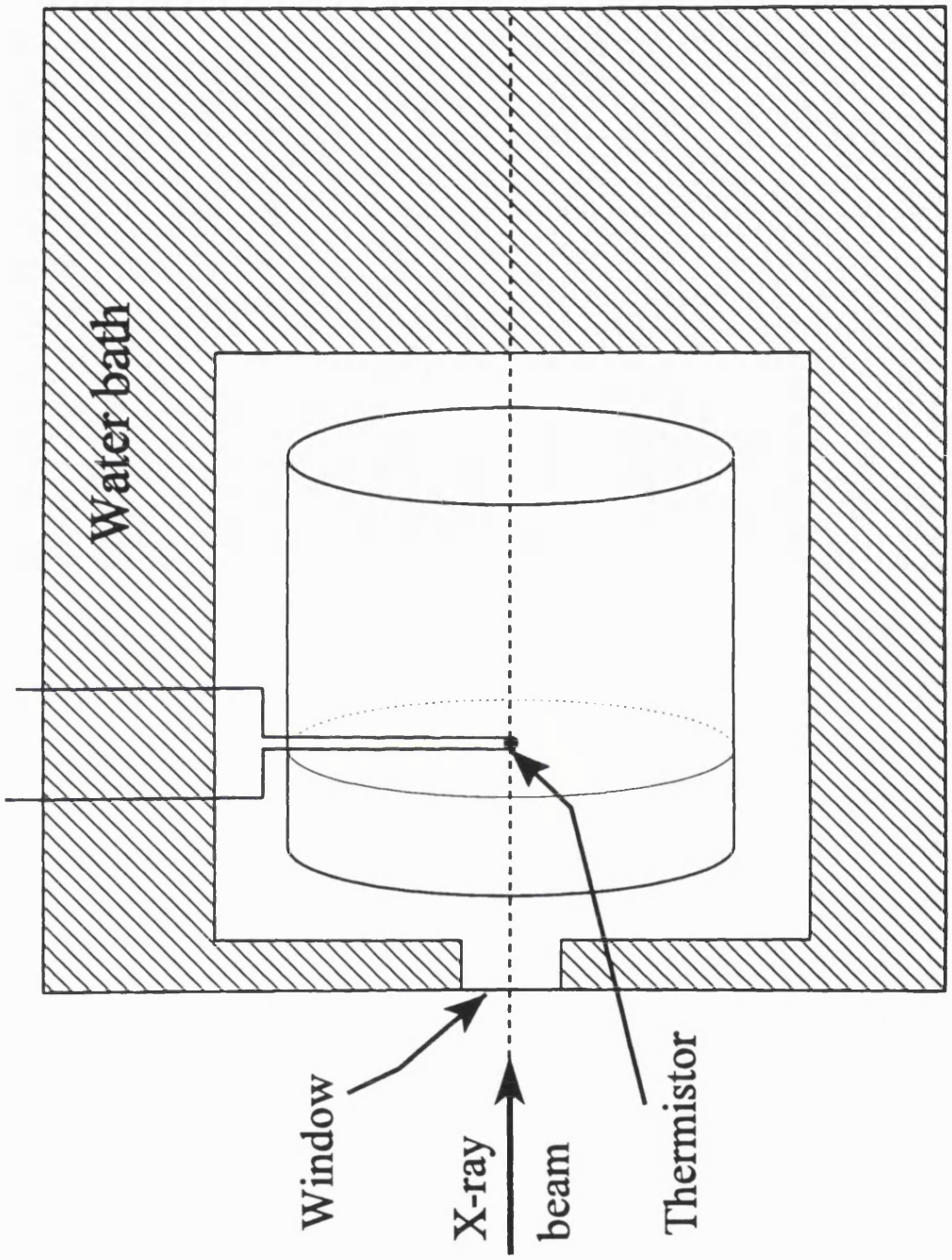

Figure 5.4: Diagram of the water calorimeter.

The calorimeter was kept at 4 °C by placing it in a water bath that operated at (4 ± 0.004) °C. These temperature variations are larger than the temperature rise due to the radiation. The bath was therefore designed with an air cavity surrounding the calorimeter vessel; the air acts as a buffer so that the water in the calorimeter vessel will experience smaller temperature variations than in the bath.

5.4 INTRODUCTION TO THERMISTORS.

Thermistor is an acronym for thermally sensitive resistor. Thermistors are made from semiconductors and have temperature coefficients that range from about -5% to +60% per °K. The advantages of using a thermistor as a temperature sensitive device in the calorimeter are:

1. Large temperature coefficient of resistance.
2. Small size.
3. The ability to withstand electrical and mechanical stresses.
4. The possibility to measure temperature remotely.

The sign of the temperature coefficient distinguishes the basic types of thermistors that is negative temperature coefficient (N.T.C) and positive temperature coefficient (P.T.C). Commercial PTC thermistors are comparatively new, cannot be specified specifically for analytical work and have a temperature coefficient that depends markedly on temperature. In future PTC thermistors should be an advantage to calorimetry due to their large temperature coefficients over a small temperature range. In this work NTC thermistors were adopted as they were most widely available. The variation of the resistance of N.T.C thermistors with temperature approximately follows an exponential law over a limited temperature range.

$$R = R_o \exp\left(\beta\left(\frac{1}{T} - \frac{1}{T_o}\right)\right) \qquad (19)$$

where:

R_o is the resistance of the thermistor at temperature T_o.

β is the material constant.

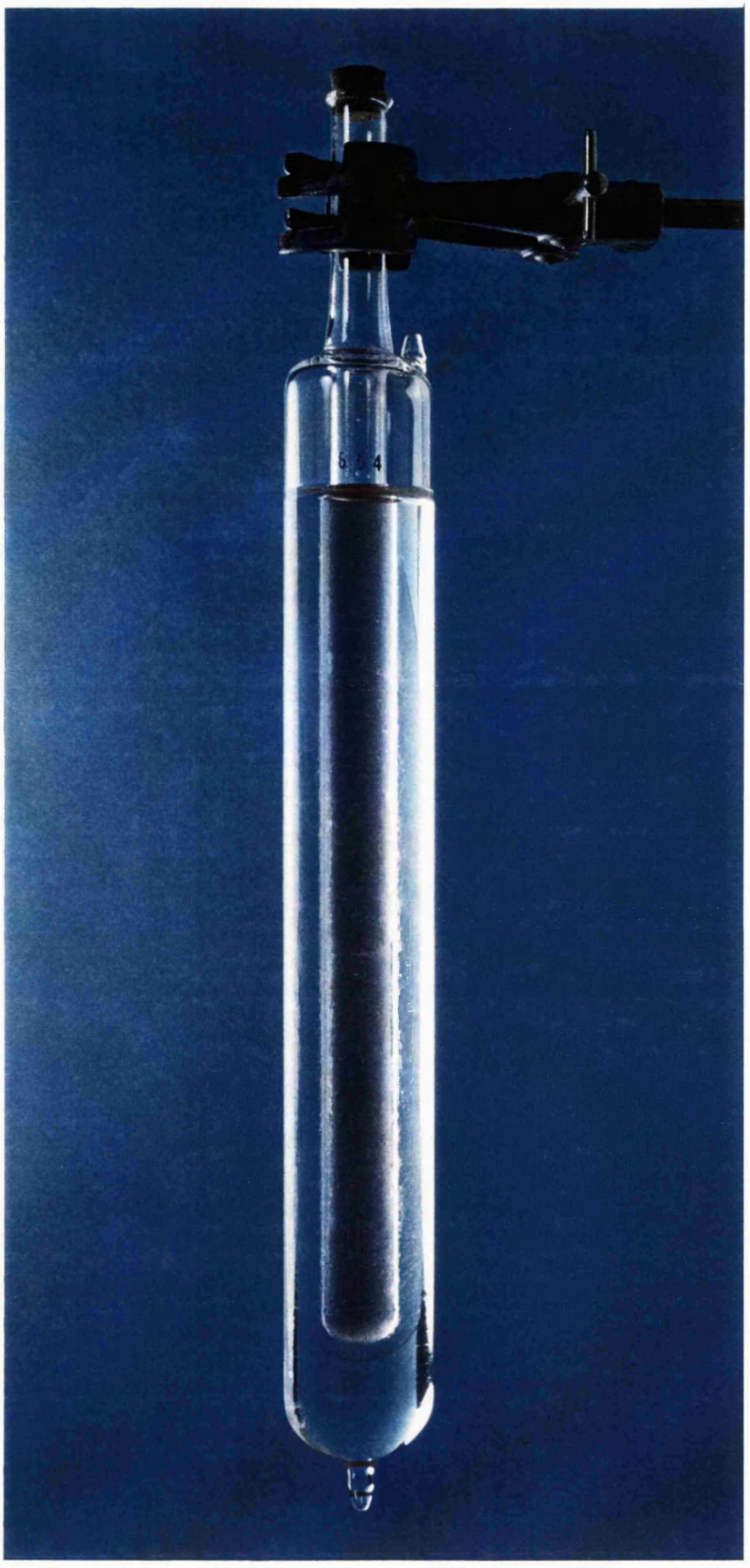

Figure 5.5 Picture of a water triple point cell.

The sensitivity (S) of the thermistor is defined by:

$$S = \frac{1}{R}\frac{dR}{dT} = -\frac{\beta}{T^2} \qquad (20)$$

5.4.1 MEASUREMENT OF TEMPERATURE USING A THERMISTOR CONNECTED TO A WHEATSTONE BRIDGE.

There are two methods of using a wheatstone bridge to measure the change of thermistor resistance with temperature. Firstly the out-of-balance voltage of the bridge produced by the change in thermistor resistance is nulled using a balance resistor. The change in balance resistor is then equal to the change in thermistor resistance. The temperature change can be determined by calibrating the thermistor resistance in terms of temperature. An alternative method is to measure the change in bridge out-of-balance voltage with variation in thermistor resistance. Here the temperature change can be determined by calibrating the bridge out-of-balance voltage directly in terms of temperature. This method eliminates the need to convert from voltage change to resistance change and as no null balancing is required the measurement is simplified. Kubo and Brown [70] have shown that there is no significant difference between the temperature measured using the two methods therefore the second method will be adopted in this thesis.

5.4.2 CALIBRATION OF THE THERMISTOR USED IN THE WATER CALORIMETER

Absorbed dose to water is derived from the measurement of the temperature rise produced by the radiation, therefore the thermistor must be calibrated. In principle only relative temperatures are required although in practice it is more convienient to work with absolut temperatures. The thermistor is calibrated against a platinum resistance thermometer, that in turn is calibrated using triple point cells.

The temperature scale adopted now is International Temperature Scale of 1990, ITS-90 [77]. This is based on several reference point temperatures, ranging from the triple point for hydrogen at -259.3467 °C to the freezing point of copper at 1084.62

°C. The triple-point temperature of a pure substance is where solid, liquid and vapour phases of a pure substance coexist in equilibrium. In the temperature range 0 to 50 °C, triple points are best realized using triple point cells (see figure 5.5). For a water calorimeter there are three commercially available cells covering the temperature range 0-40 °C: those of water at 0.01 °C, diphenyl ether at 26.862 °C and ethylene carbonate at 36.315 °C.

5.5 INITIAL MEASUREMENTS USING A WATER CALORIMETER.

The calorimeter vessel was placed in the cavity of the temperature bath operated at 4 °C. The bath was then placed on the carriage in the ^{60}Co exposure room at a focal distance of approximately 40 cm with the thermistor on the beam axis. The thermistor was then connected to the DC wheatstone bridge with a bridge voltage of 1.266 V. The water calorimeter was irradiated at a dose-rate of 3 Gy/minute for a total dose of 30 Gy.

A typical calorimeter run is shown in figure 5.6, the pre-irradiation drift is from a to b, from b to c the calorimeter is irradiated and the post irradiation drift is from c to d. The slope of the pre and post irradiation drifts are dependent on the environmental conditions and on the radiation history of the calorimeter. If the slopes differ then the measurement should be rejected as a temperature change in the environment has occurred during the irradiation period. The temperature rise can be calculated by extrapolating a linear fit on the pre and post irradiation drift to the midpoint of the irradiation.

Figure 5.7 shows that when the absorbed dose to the water is reduced to a typical clinical dose of 5 Gy at 1 Gy/minute then the signal to noise ratio is too low for accurate measurements. The situation deteriorates when using medium energy X-rays at NPL, as the maximum dose-rate is 0.3 Gy/min at the point of measurement. The water calorimeter in its present form was therefore abandoned.

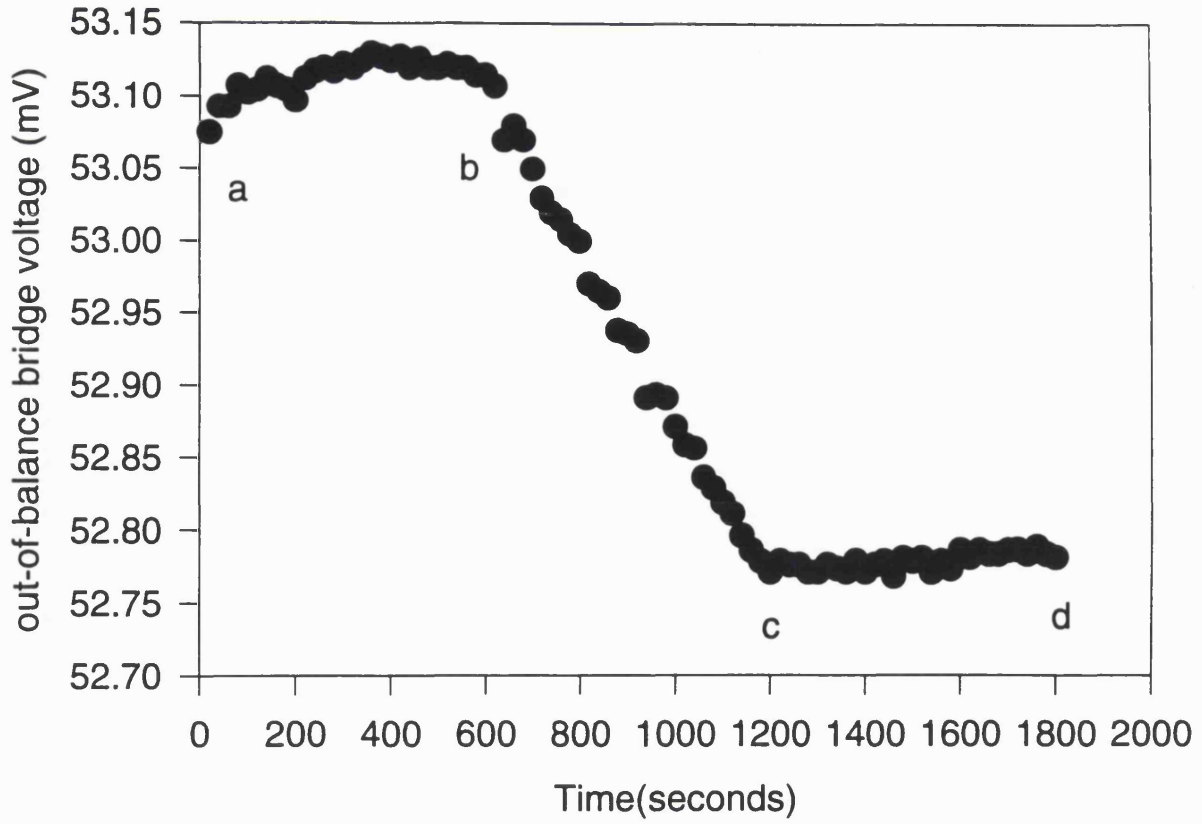

Figure 5.6: A typical water calorimeter irradiation at 3Gy/min for a total dose of 30 Gy, using Co-60 gamma rays.

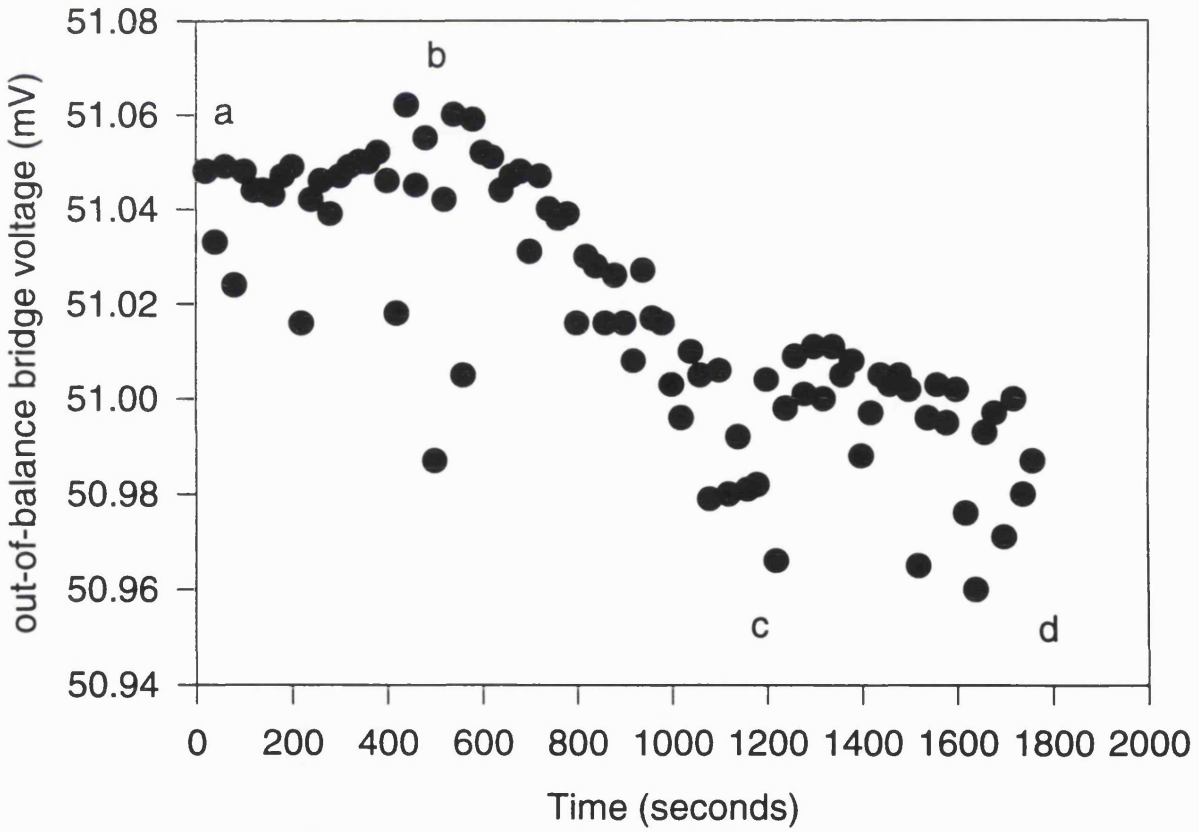

Figure 5.7: A water calorimeter irradiation at 1Gy/min for a total dose of 5 Gy, using Co-60 gamma rays.

CHAPTER 6

MEASUREMENT OF ABSORBED DOSE TO WATER USING AN ICE CALORIMETER.

If an experiment requires statistical analysis to establish a result, then one should do a better experiment.

Ernest Rutherford.

6.1 INTRODUCTION.

In the previous chapter it was found that water calorimetry was impractical for the low dose rates used in this thesis due to its low signal to noise ratio. To overcome this, an ice calorimeter was designed and built.

The only reference to an ice calorimeter in the literature [71] was formed with melt ice and water in equilibrium. The temperature rise due to the radiation was found by measuring the change in volume of the mixture when irradiated. However, this method is very insensitive as the volume of the ice and water mixture decreases by only 0.2717 $mm^3 J^{-1}$. The ice calorimeter described in this thesis relies on the ice remaining in a stable state and the temperature measured at a point in the ice.

6.1.1 COMPARISON OF WATER AND ICE CALORIMETRY.

6.1.1.1 ADVANTAGES OF ICE CALORIMETRY.

6.1.1.1.1 TEMPERATURE RISE.

For a water calorimeter the temperature rise is only 0.2 mK when irradiated to a dose of 1 Gy. Figure 6.1 shows that there is a step in the specific heat capacity [79] when water is frozen, and it continues to decreases with decreasing temperature. This results in the small temperature rise due to the radiation being magnified when water is frozen. For example at -10 ^{0}C the specific heat capacity of ice is approximately half that of the water at 4 ^{0}C. Therefore, the temperature rise in an

ice calorimeter will be double that in a water calorimeter for the same absorbed dose.

6.1.1.1.2 THE EFFECTS OF MATERIALS IN CONTACT WITH WATER.

A water calorimeter requires a vessel to contain the water for example water calorimeters have been designed with Perspex [12] and glass calorimeter container vessels [50, 51, 55]. This can cause two effects, firstly if the material leaches impurities during storage or irradiation then the heat defect will be altered. Secondly the specific heat capacity of glass is about one fifth that of water. So for the same absorbed dose the temperature rise in glass is about five times that of the surrounding water and consequently heat is conducted from the glass to the water.

Ice may solve this problem as it does not require a vessel in contact with the ice during operation. But water does require containment while freezing and therefore impurities may leach into the ice at this stage.

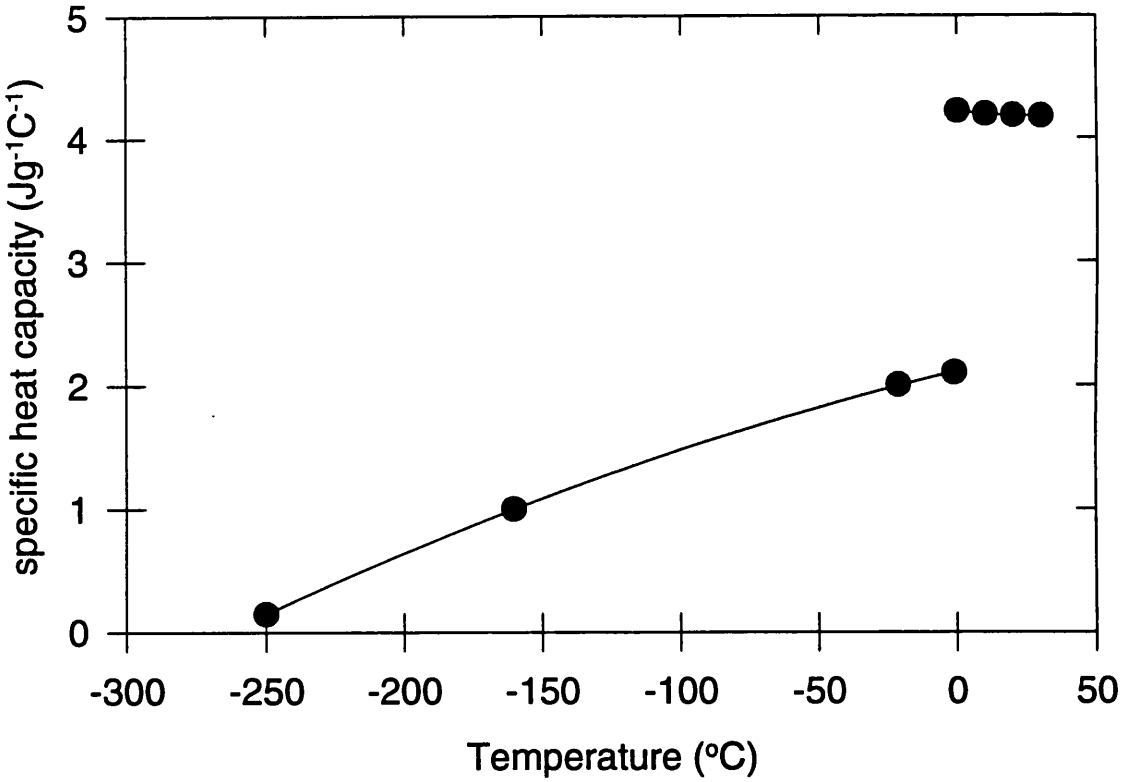

Figure 6.1 The variation of specific heat capacity with temperature for water.

6.1.1.2 DISADVANTAGES OF ICE CALORIMETRY.

6.1.1.2.1 PHASE BEHAVIOUR IN ICE

Figure 6.2 shows that there are nine phases of ice depending on the pressure and temperature of formation [72]. In addition there exists a modification of hexagonal ice (1h), called cubic (1c) ice that is metastable between -80 to -120 °C, at which temperature it becomes stable [73, 74]. For ice calorimetry all phase changes should be avoided. This can be achieved by forming the ice at atmospheric pressure and restricting the temperature range between 0 and -80°C.

6.1.1.2.2 THERMAL DIFFUSIVITY OF ICE.

The thermal diffusivity of ice is approximately ten times that of water. This may result in the heat due to the radiation diffusing too quickly to enable the measurement of absorbed dose to water at a point. To overcome this, the ice calorimeter design may incorporate a thermally isolated core where the absorbed dose is measured similarly to that in a graphite calorimeter. This would be difficult to manufacture as machining a thin disc of ice may cause it to melt. Alternatively the diffusion of heat throughout the calorimeter can be modelled and a correction applied. In this thesis the latter method will be adopted.

6.1.1.2.3 HEAT DEFECT.

Klassen [75] has shown a chemically stationary state exists for both pure and H_2 saturated ice near 0 °C when irradiated at low doses. Klassen showed that for de-arated ice, freshly frozen and operated at -10 °C a stationary state was reached after a dose of 25 Gy. For ice annealed at -10 °C for 2-4 days before irradiation a stationary state was achieved after a dose of 8 Gy. If the temperature of the ice is reduced to -23 °C then a stationary state is reached after 200 Gy. Klassen also showed that cracked ice exhibited erratic behaviour.

Klassen irradiated the ice using ^{60}Co gamma rays at a dose rate of 8 Gy/min. It was shown in chapter 5 that there is little difference between the heat defect for water irradiated with ^{60}Co gamma rays and 134 kV X-rays. In this chapter it will be assumed that this is valid for ice.

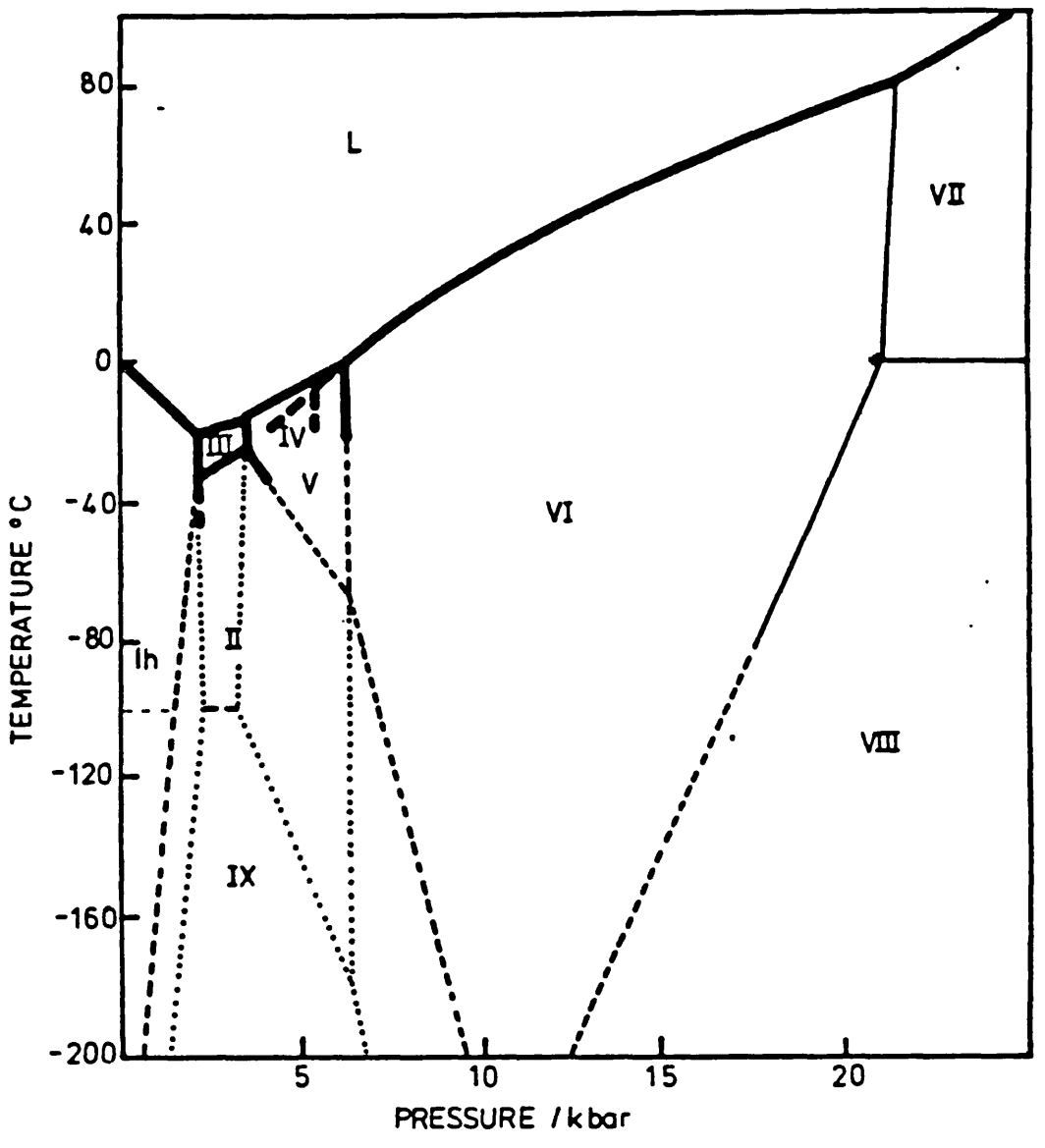

Figure 6.2: Phase diagram for ice.

Reproduced from 'Ice Physics' by Hobbs [72] by permission of Oxford University Press.

6.2. MEASUREMENTS OF THE ABSORBED DOSE TO WATER USING AN ICE CALORIMETER.

6.2.1 CONSTRUCTION OF THE ICE CALORIMETER.

The dimensions of the ice calorimeter were the same as those chosen for the water calorimeter (see chapter 5). The water used to make the ice calorimeter was the triple distilled water used for the preparation of the NPL Fricke solution [76] i.e. the purest available. The Pyrex glass beakers in which the ice was formed were cleaned using chromic acid. The ice calorimeter was constructed of two ice blocks 6 cm in diameter, 8 cm and 2 cm long respectively. To form clear ice free of any air bubbles the beakers were placed in a temperature controlled bath, surrounded by water at -8 ^{0}C. When the temperature of the water fell below freezing point a small amount of ice was placed in the beaker to seed the ice. Each of the ice blocks was allowed to form slowly overnight and then removed from the beakers by hand.

A thermistor 3.18 mm long and 0.46 mm diameter was placed in a Si coated plastic sleeve and then sandwiched between the ice blocks. The two ice blocks were placed on top of one another and fused together after about 24 hours. The resulting cylinder of ice was then placed horizontally in the cavity of a temperature controlled bath operated at -8°C.

The resistance of the thermistor was 97 kΩ at the ice temperature of -6 °C and its resistance changed with temperature by approximately 246 ΩK^{-1}. The thermistor leads were soldered to two copper leads, which were then connected to one arm of an AC wheatstone bridge using a low noise cable. Thus, the electronics could be operated in the control room next to the irradiation facilities.

6.2.2 MEASURING ELECTRONICS.

Figure 6.3 is a schematic diagram of the electronics used to measure the temperature rise in the ice. This consists of an AC wheatstone bridge that produces an AC voltage change in response to the change in thermistor resistance.

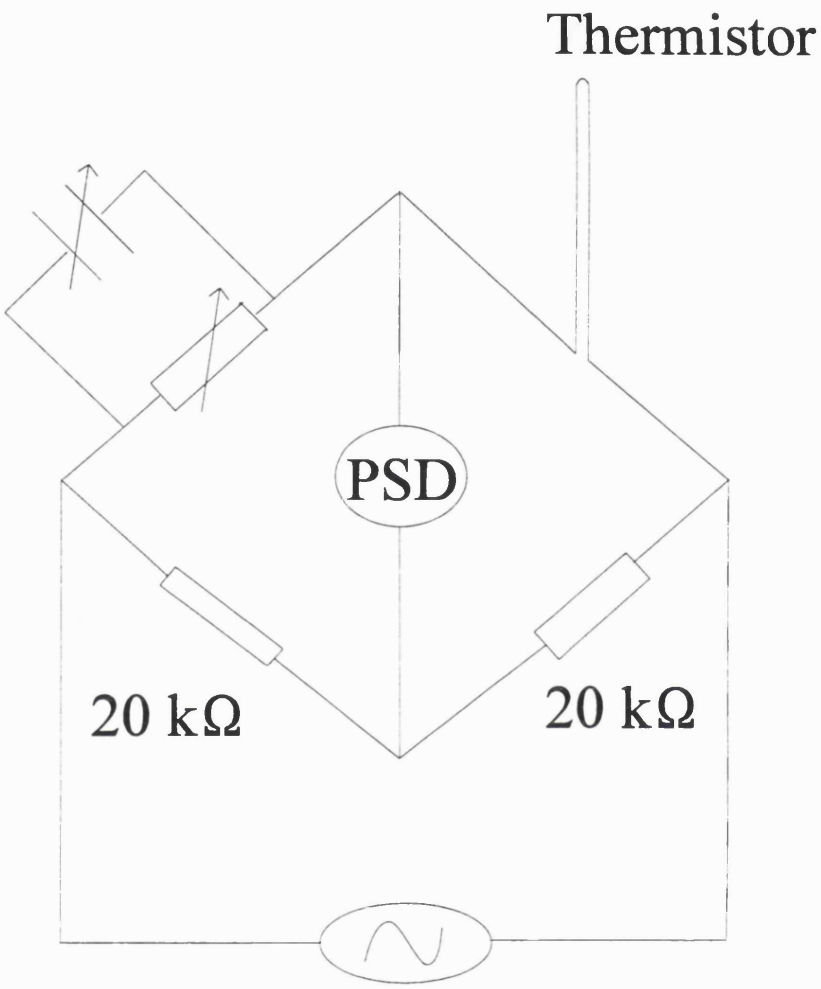

Figure 6.3: Schematic diagram of the measuring circuit used for the ice calorimeter.

The fixed resistors used in the bridge were high precision made by Vishay with a stability of 0.6 ppm/K. The bridge was driven by a smooth sine wave produced by an EG&G model 5209 lock-in amplifier operated at a frequency of 182.6 Hz. This frequency was chosen as it is not a harmonic of the mains electricity supply (48 to 52 Hz).

The AC out of balance bridge voltage was amplified, demodulated and amplified to a DC voltage. The DC voltage was fed into an analogue to digital converter. All of this was done using an EG&G model 5209 lock-in amplifier that consists of a high gain AC amplifier, a phase sensitive detector and a DC amplifier.

A BBC computer was used to read the DC out of balance bridge voltage from the EG&G lock-in amplifier. The results were displayed on its screen and stored on a floppy disc. The data was transferred to a 486 personal computer for analysis.

6.2.2.1 CIRCUIT SHIELDING.

Successful measurements at very low voltages (μV) require particular care related to shielding, thermo-electric effects, ground loops, magnetic fields and Johnson noise. The special precautions required to reduce the noise were:

1. Low noise cable was used to connect the thermistor to the AC wheatstone bridge.
2. The thin leads from the thermistor to the cable were wrapped in aluminum foil and earthed.
3. The cast-aluminum box used to house the bridge was earthed.
4. The calorimeter was shielded in the steel temperature bath by providing an earthed aluminum foil lid.
5. The outside of the temperature bath was earthed.
6. A single earthing point for the circuit was provided by the EG&G lock in amplifier.

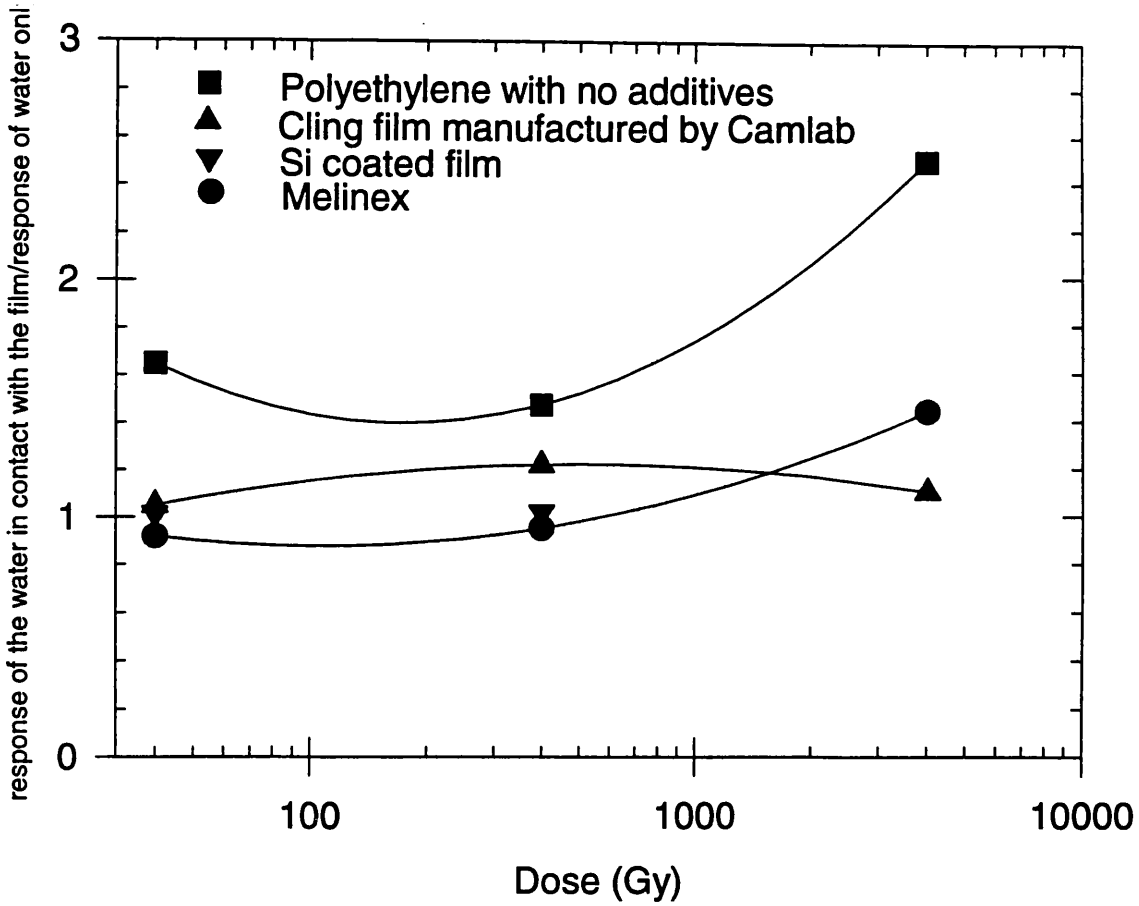

Figure 6.4: Effect of films on the purity of water.

6.3 EFFECTS OF FILM ON THE PURITY OF WATER

For the ice calorimeter the effect of the film used to insulate the thermistor, on the purity of the ice is unknown. If the film is leaching impurities to the ice calorimeter then the heat defect is unpredictable. This experiment was performed using water instead of ice. It is expected that the reactions in water will be quicker than those in ice and therefore have a greater effect on the heat defect. Melinex, polyethylene with no additives, cling film produced by Camlab and silicon coated film were investigated as their manufacturers claimed that these films do not evolve organic impurities in water. This was done by taking advantage of the fact that Fricke solution is sensitive to impurities [76].

The film was placed in a beaker of triple distilled water and irradiated for a rangeof doses between 40 and 4000 Gy using ^{60}Co γ-rays. A mixture was made of equal amounts of Fricke solution and the water in contact with the film. The optical density of this mixture was compared with that of a control mixture. Figure 6.4 shows that water in contact with the polyethylene with no additives affects the purity of water. Whereas the remaining three films show a reduced effect.

6.4 MEASUREMENT OF THE TEMPERATURE RISE USING A THERMISTOR.

The absorbed dose is derived from the measurement of the temperature rise produced by the radiation beam, the thermistor must therefore be calibrated. In principle only relative temperatures are required although in practice it is more convenient to work with absolute temperatures.

The conversion of the bridge out-of-balance voltage to a change in thermistor temperature is a two-stage process. Firstly the resistance of a 100Ω platinum resistance thermometer (PRT) was compared at reference point temperatures. The PRT was then used as a transfer device to convert the out-of-balance voltage of the bridge to temperature. I will now discuss each of these steps.

6.4.1 CALIBRATION OF A PLATINUM RESISTANCE THERMOMETER.

The normal method of calibrating a platinum resistance thermometer (PRT) is using triple point cells (see section 5.4.2). However, the closest reference point temperature (below zero) to the operating temperature (-6 °C) of the ice calorimeter is the freezing point of mercury at -38.862 °C. As this is far from -6 °C the temperature section at NPL calibrated the PRT by direct comparison with a secondary standard PRT.

6.4.2 CALIBRATION OF THERMISTORS.

The thermistor in the ice calorimeter was calibrated after all of the irradiations had been completed. A hole approximately 3 mm in diameter was drilled in the ice as close to the thermistor as possible and the PRT was placed in the hole. The PRT was connected to a DVM programmed to read resistance directly. This DVM was checked every morning with a 100 kohm resistor, no change was observed in the measured resistance throughout the experiment within the uncertainty of the DVM (five decimal places). The temperature of the bath was varied from -6 to -8 °C, ensuring that the bath was allowed a minimum of 7 hours to reach equilibrium after each step. At each step a set of 10 readings were taken of the out-of-balance bridge voltage and the resistance of the PRT.

6.5 COMPARISON OF THE ABSORBED DOSE TO WATER MEASURED USING THE ICE CALORIMETER TO THAT USING THE PRIMARY STANDARD GRAPHITE CALORIMETER USING ^{60}CO GAMMA RAYS.

6.5.1 IRRADIATION OF THE ICE CALORIMETER.

The ice calorimeter was placed in a temperature bath with its major axis positioned on the beam axis. The calorimeter was irradiated via a monitor chamber, using a field size of 6 cm x 6 cm at the position of the thermistor. Before the start of the irradiations the ice calorimeter was given a dose of approximately 30 Gy, this was repeated after a break in the irradiations of more than 1 day.

The out-of-balance voltage from the wheatstone bridge was measured every 8 seconds. Figure 6.5 shows a typical calorimeter measurement. It consists of three stages, an initial temperature drift measurement for 240 seconds, an irradiation period of 240 seconds to give a dose of approximately 1.5 Gy and a post irradiation drift measurement for 480 seconds. It was found that the pre and post irradiation drifts were very noisy for a single calorimeter run. This was improved by summing the calorimeter runs point by point for 30 calorimeter runs. Figure 6.6 shows that combining the calorimeter runs in this way gives an improved signal to noise ratio of approximately 250:1.

To determine the absorbed dose to water using these measurements both the temperature rise and the specific heat capacity at the operating temperature are required. The traditional method of determining the temperature rise from figure 6.6 is to fit a line to the pre and post irradiation drifts and extrapolate them to the midpoint of the irradiation. However for ice calorimetry it can be seen that the pre and post irradiation drifts have distinctive shapes that makes this method impossible. The temperature rise was therefore determined by modelling [78] the diffusion of heat throughout the ice as recommended by Duane and described in Appendix 4. The specific heat capacity was interpolated (see figure 6.1) to the

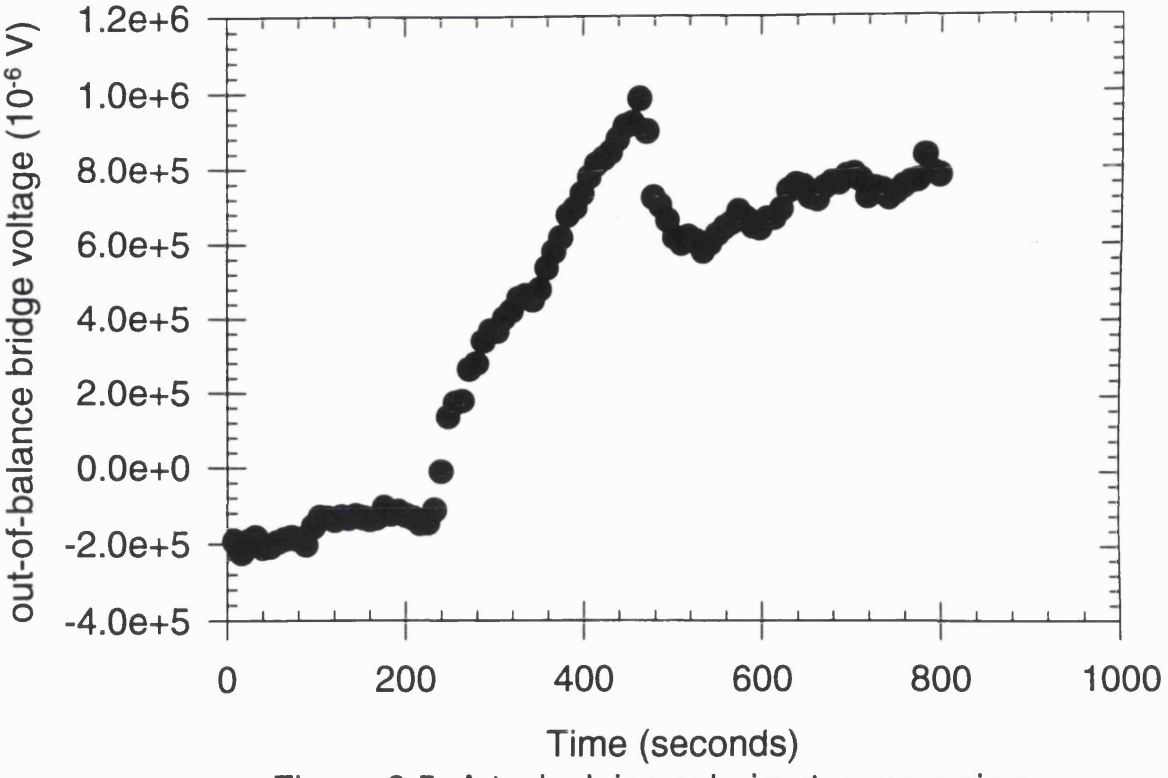

Figure 6.5: A typical ice calorimeter run using ^{60}Co gamma rays.

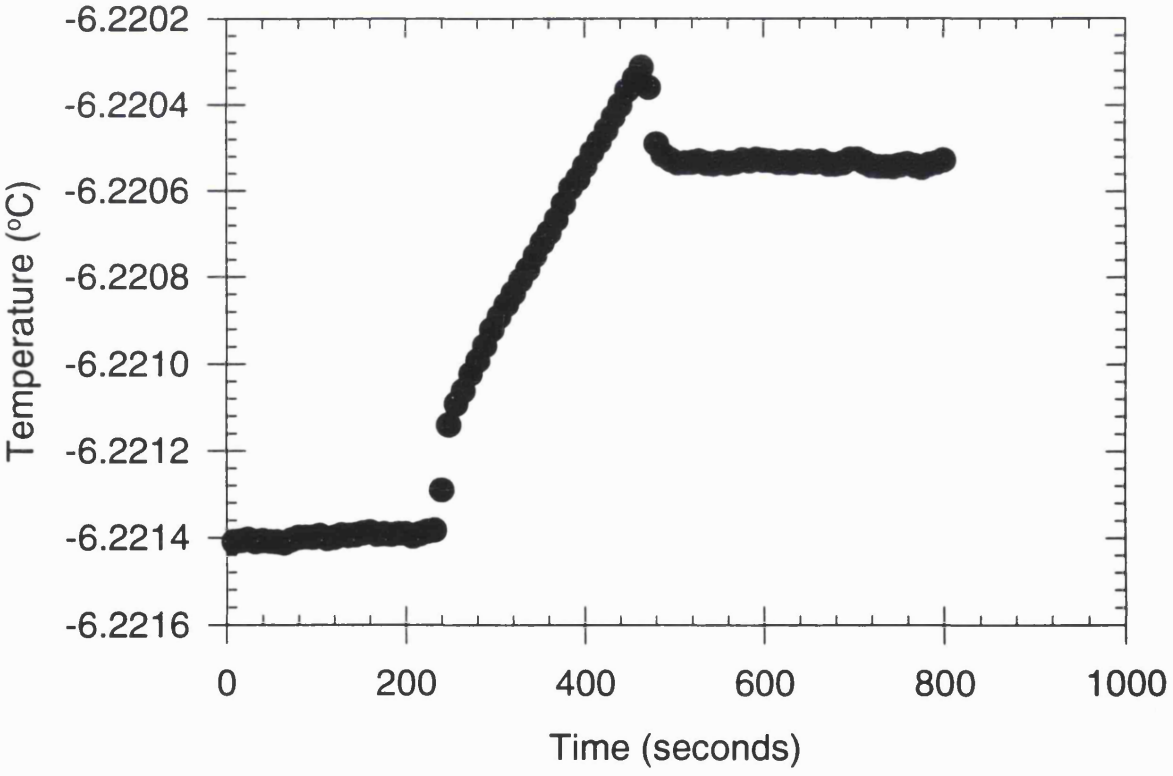

Figure 6.6: Summation of 30 ice calorimeter runs, when irradiated with ^{60}Co gamma rays.

operating temperature using data given in Kaye and Laby [79].

6.5.2 IRRADIATION OF A NE2561 IONIZATION CHAMBER

The ice calorimeter was removed from the temperature controlled bath and the temperature of the bath was increased from -10 °C to 20 °C. A glass vessel that had the same external dimensions as the ice calorimeter and a front face 0.2 mm thick, was placed in the bath, such that the glass vessel will experience the same radiation field as the ice calorimeter. The glass vessel was then filled with water and a waterproof sleeve was fixed at 2 cm deep in the vessel. Three NE2561 ionization chambers were placed alternately in the sleeve and their responses measured using a NE2560 electrometer via a monitor chamber. The response of each chamber was corrected for temperature, pressure, front face of the glass vessel and depth in water.

To investigate the effects of the waterproof sleeves on the chambers response, each chamber was measured in three different sleeves. The maximum spread between a set of measurements was 0.2% and the difference between the sleeves was 0.4%.

6.5.3 CALIBRATION OF A NE2561 IONIZATION CHAMBER BY DIRECT COMPARISON WITH THE PRIMARY STANDARD GRAPHITE CALORIMETER IN ^{60}Co.

Figures 6.7 and 6.8 show the NPL primary graphite calorimeter [80] that follows the design of Domen [41]. Absorbed dose to graphite is measured in the 2 cm diameter, 3 cm thick graphite disc which forms the core of the calorimeter. The core is surrounded by three graphite jackets to isolate it thermally from an extensive graphite phantom. The gaps of 1mm between the core and the jackets are evacuated. During irradiation the energy absorbed by the core raises the core temperature by T_R, which is sensed by a thermistor in one arm of an AC bridge [81,42]. The calorimeter is calibrated by dissipating in the core a measured quantity of electrical energy, E_E. For the core of mass m, the absorbed dose to graphite is given by:

$$D_C = \frac{E_E \cdot T_R}{m \cdot T_E} \qquad (21)$$

where T_E is the temperature rise during the electrical calibration.

In practice changes in bridge out of balance voltage are measured rather than actual changes of temperature. The main corrections to the calorimeter measurements are for the effects of the gaps around the core [45] and for the energy losses during the electrical calibration.

To calibrate each NE2561 ionization chamber, they were placed alternately in a 17 cm sided, square graphite phantom. The centres of the chambers and midplane of the calorimeter core were placed at the same depth in graphite and same source to detector distance. The ionization chamber measurements were corrected to standard temperature and pressure. This comparison gives chamber calibration factors in terms of absorbed dose to graphite per unit charge. The conversion to absorbed dose to water follows the work of Burns [46] where the photon fluence scaling theorem was used.

6.5.4 RESULTS

TABLE 6.1 RESULTS OF THE COMPARISON BETWEEN GRAPHITE AND ICE CALORIMETRY USING ^{60}Co GAMMA RAYS.

NE2561 chamber serial number.	258	259	260
calibration factor in absorbed dose to water per charge determined using the graphite calorimeter (Gy/C x 10^7)	10.021	10.312	10.244
calibration factor in absorbed dose to water per charge determined using the ice calorimeter. (Gy/C x 10^7)	9.843	10.140	10.049
ice calorimetry / graphite calorimetry	0.982	0.983	0.981

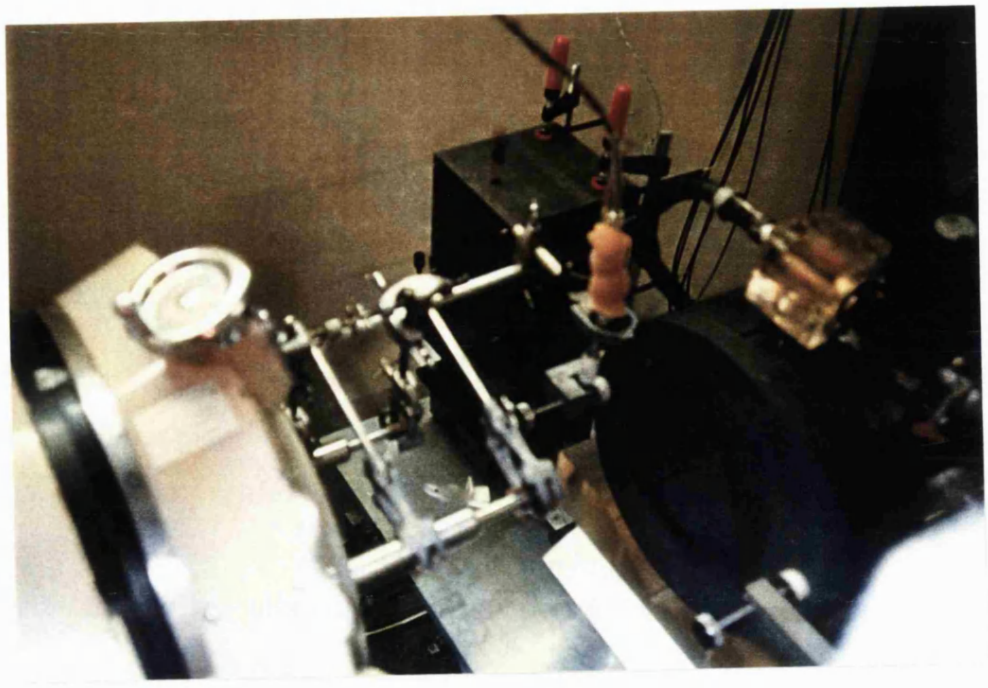

Figure 6.7: Picture of NE2561 chamber calibrated by direct comparison with the primary standard graphite calorimeter.

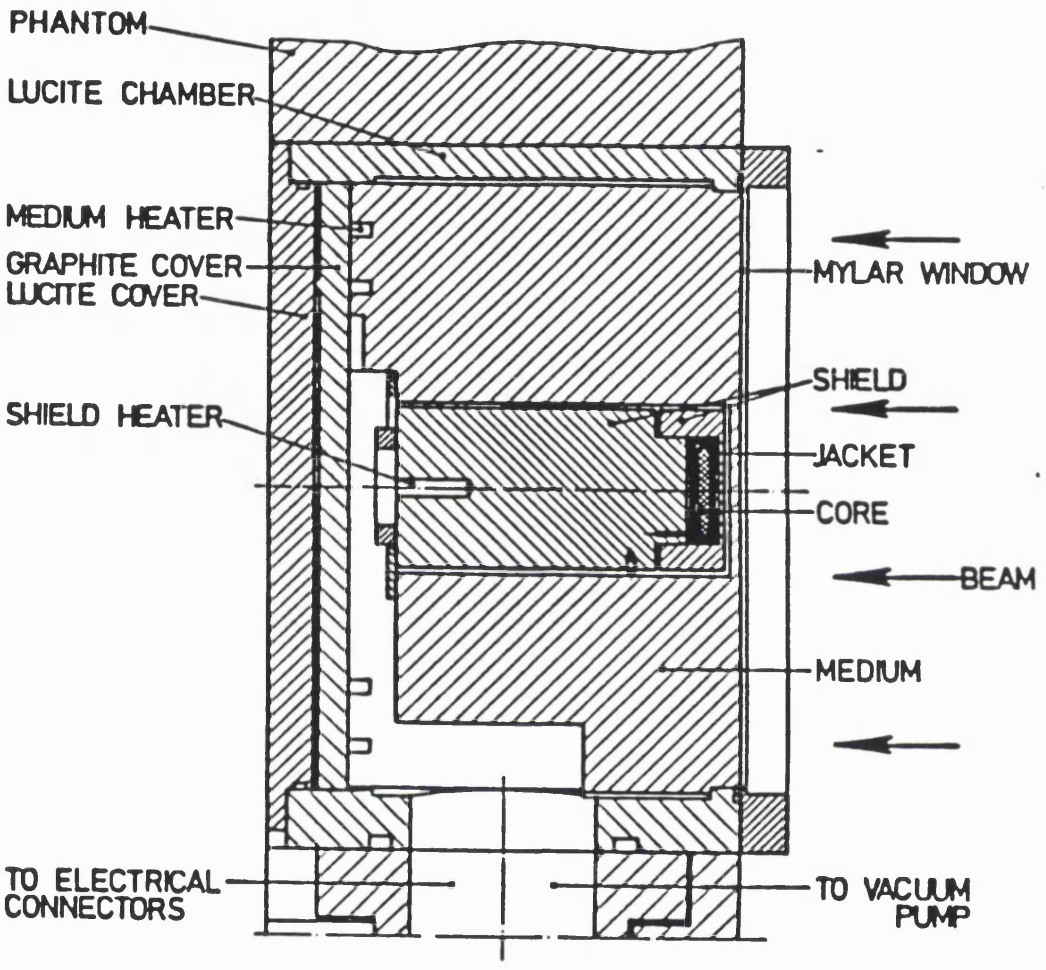

Figure 6.8: Diagram of the primary standard graphite calorimeter

6.5.5 UNCERTAINTIES

TABLE 6.2 UNCERTAINTIES FOR THE MEASUREMENTS DONE USING ^{60}Co GAMMA RAYS.

Source of uncertainty	uncertainty (1σ) (%)	
	Random	non-random
Comparison with the graphite calorimeter.		
Calibration of the ionization chambers by comparison with the graphite calorimeter [80]		1.4
Deviation from inverse square law (a)	0.75	
chamber measurement		
depth in water (b)	0.7	
charge calibration of NE2560 electrometer [82]		0.1
set of five readings (c)	0.1	
difference between waterproof sleeves (see section 6.5.2)	0.4	
correction due to front face of phantom (d)		0.05
ice calorimeter measurement		
calibration of PRT (e)		0.04
calibration of the thermistor (f)	2	
depth in ice (g)		0.7
interpretation of temperature rise in the ice.(h)	1	
specific heat capacity of ice (i)		3
Quadrature sum	2.5	3.4
Overall uncertainty	4.2	

(a) Estimated from inverse square law measurements.

(b), (g) and (d) The uncertainty in depth was estimated from visual inspection. This was converted to an uncertainty in the dose from depth dose data given in BJR Supplement 17 [40].

(c) This uncertainty is the standard deviation of a set of five ionization chamber readings.

(e) This uncertainty was taken from the calibration certificate.

(f) and (h) Estimated from a fit to the experimental data.

(i) Estimated from Giauque and Stout [83].

6.6 DETERMINATION OF THE CHAMBER CORRECTION FACTOR FOR A NE2561 IONIZATION CHAMBER IRRADIATED WITH X-RAYS GENERATED AT 134 KV.

6.6.1 IRRADIATION OF THE ICE CALORIMETER.

The ice calorimeter was operated in the same manner as when it was irradiated using ^{60}Co gamma rays except that the out-of-balance voltage from the bridge was measured every 12 seconds for a dose rate of approximately 0.25 Gy/min. Figure 6.9 shows the sum of 25 calorimeter measurements when the ice calorimeter was irradiated using X-rays generated at 134 kV.

6.6.2 ABSORBED DOSE TO WATER MEASURED USING AN IONIZATION CHAMBER.

Three NE2561 ionization chambers connected to a Keithley electrometer were used for the ionometric measurements. The ionization chambers without their waterproof sleeves were initially calibrated in air by direct comparison with the primary standard free air chamber, as described in chapter 3. To ensure that the ionometric measurements were performed in a similar geometry to the ice calorimeter, a glass vessel having the same dimensions as the calorimeter was employed with the chambers placed in their waterproof sleeves at 2 cm deep. The glass vessel was placed in the water bath maintained at 20 °C.

A set of readings consisted of five readings taken of the ionization current via a

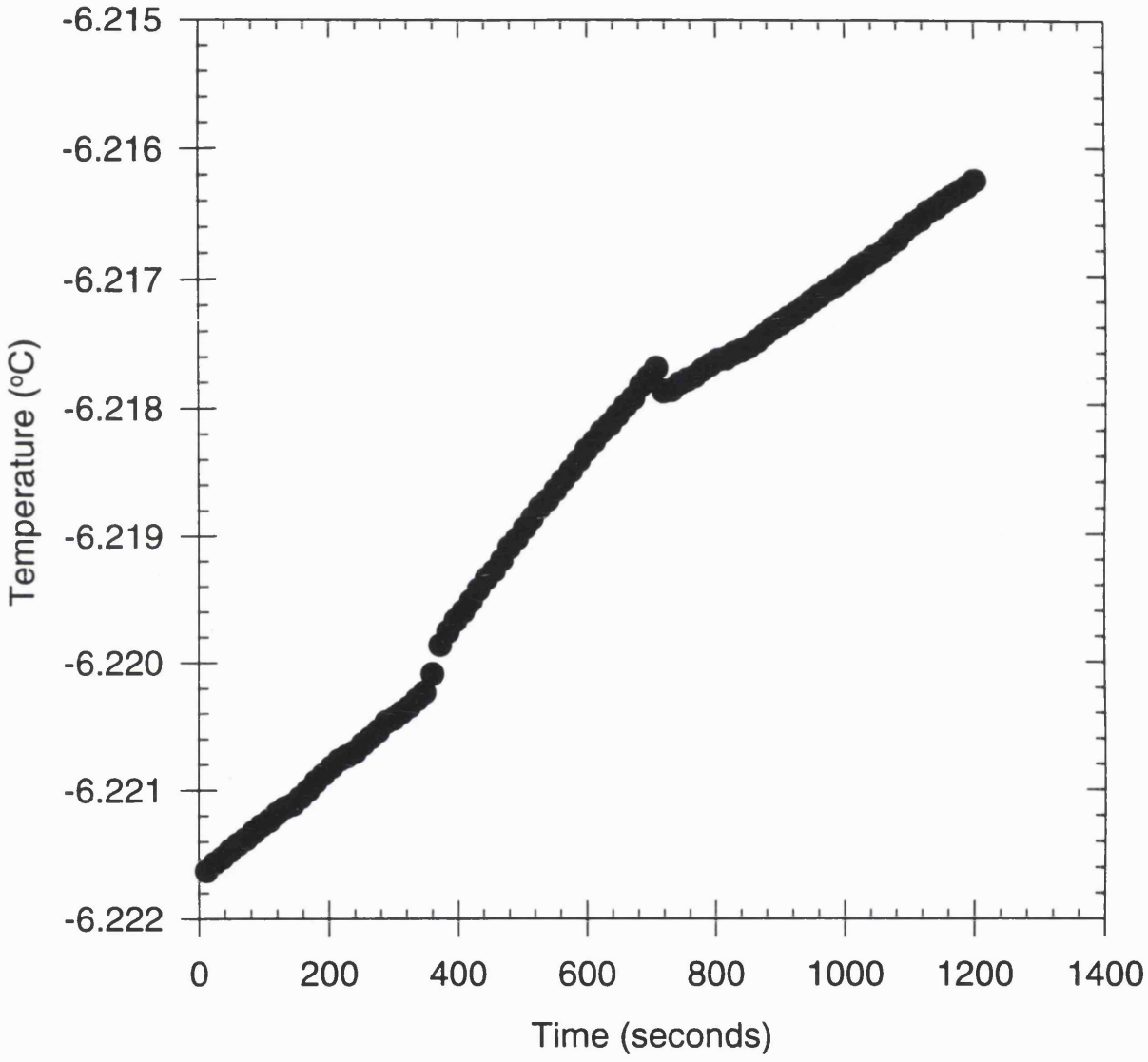

Figure 6.9: Summation of 22 calorimeter runs when the ice calorimeter is irradiated with X-rays generated at 134 kV.

transmission monitor. To check the reproducibility and the effect of the waterproof sleeves, three sets of measurements were performed with each chamber in the three sleeves. The maximum spread between the sets of measurements was 0.3%, whereas the maximum difference between the sleeves was 1.1%. The absorbed dose to water was determined for each chamber using the equation in Section 3.3 where $(\bar{\mu}_{en}/\rho)_{w,a}$ is taken from Table 4.3.

6.6.3 RESULTS

TABLE 6.3 RESULTS OF THE DETERMINATION OF ABSORBED DOSE TO WATER USING AN IONIZATION CHAMBER.

NE2561 chamber serial number	258	259	260
air kerma calibration factor (Gy/C x 10^7)	8.840	9.165	9.164
$(\bar{\mu}_{en}/\rho)_{w,a}$	1.051	1.051	1.051
calibration factor determined using chapter 3. (Gy/C x 10^7)	9.291	9.623	9.631

TABLE 6.4 RESULTS OF THE DETERMINATION OF ABSORBED DOSE TO WATER USING THE ICE CALORIMETER.

NE2561 chamber serial number	258	259	260
Temperature measured using the ice calorimeter (°C x 10^{-4})	7.186	7.186	7.186
specific heat capacity of ice ($JKg^{-1}C^{-1}$)	2076.6	2076.6	2076.6
Response of chamber. (C x 10^{-8})	1.649	1.6169	1.6079
calibration factor (Gy/C x 10^7)	9.049	9.229	9.281
ice calorimetry / chamber dosimetry	0.974	0.959	0.964

6.6.4 UNCERTAINTIES

TABLE 6.5 UNCERTAINTIES ASSOCIATED WITH THE MEASUREMENT OF K_{ch} FOR A NE2561 CHAMBER IRRADIATED WITH 134 kV X-RAYS

Source of uncertainty	Uncertainty (1σ) (%)	
	Random	non-random
chamber measurements		
depth in water	1.5	
set of 5 readings	0.1	
charge calibration of the electrometer		0.1
front face of the glass vessel		0.05
calibration of the chamber in terms of air kerma		1.1
$(\bar{\mu}_{en}/\rho)_{w,a}$		0.15
effect of waterproof sleeves	1.1	
ice calorimeter		
depth in ice		1.5
calibration of the PRT		0.04
calibration of the thermistor	2	
interpretation of the temperature rise in ice	3.5	
specific heat capacity of ice		3
comparison of the absorbed dose to water the graphite calorimeter at ^{60}Co		1.2
Quadrature sum	4.4	3.7
Overall uncertainty	5.7	

The uncertainties were derived similarly to that given in Table 6.2.

CHAPTER 7
CONCLUSIONS

In this thesis a detailed investigation of the measurement of absorbed dose to water using an ionization chamber was performed. It was found that the chamber correction factor (k_{ch}) was dependent on the type of chamber used. For the U.K secondary standard chamber (NE2561), it was found in Chapter 3 that k_{ch} varied from (1.022 ± 0.03) to (1.016 ±0.01) for HVL between 0.15 and 4 mmCu. The only published data for a NE2561 chamber is that calculated by Ma et al [84] using Monte Carlo techniques. Ma et al found that the chamber correction factor for a NE2561 was (1.016±0.01) for X-rays at 8.8 mmAl HVL, when irradiated with a 10 x 10 cm^2 field. This agrees with the values given in this thesis within the stated uncertainties.

The ratio of mass energy absorption coefficients of water to air was calculated for the conditions given in the IAEA code and those used for the ice calorimetry. At 0.17 mmCu HVL the value calculated in this thesis agrees with the IAEA code within 0.1%.

A survey of the medium energy radiotherapy centres throughout the UK revealed that there is little consensus on the beam qualities adopted, when stated in terms of HVL. In this thesis it is recommended that HVL should be replaced with a quality index that is dependent on the depth dose curve, such as the ratio of dose at 2 and 5 cm deep in water.

Water calorimetry using medium energy X-rays was studied in this thesis. Heat defect calculations for water showed that zero heat defect could be attained using H_2 saturated water after an initial dose of about 10 Gy. It was also shown that there is negligible difference between the heat defect for water irradiated with ^{60}Co gamma rays and medium energy X-rays. Unfortunately initial measurements performed using the water calorimeter showed that it was not a useful tool using medium energy X-rays due to its low signal to noise ratio.

To overcome this problem an ice calorimeter was designed and built. The calibration factor for a NE2561 chamber at ^{60}Co determined using the primary standard graphite calorimeter is (1.8±0.08) % greater than that found using the ice calorimeter. The difference between the ice and graphite calorimeter was measured consistently with three NE2561 chambers within 0.1%. The difference between the calorimeters may be attributed to several causes such as an endothermic heat defect for the ice calorimeter or a problem in converting from graphite to water for the graphite calorimeter.

The ice calorimeter was then irradiated with 0.5 mmCu HVL X-rays as this is the lowest medium energy recommended in the new UK code of practice for low and medium energy X-rays [85]. It was found that the absorbed dose to water measured using the ice calorimeter is less than that using conventional chamber dosimetry by (3.5±0.2)%. If the difference between ice and graphite calorimetry at ^{60}Co is attributed to an endothermic heat defect for the ice then this difference is reduced to 2%. This implies that the chamber correction factor for a NE2561 ionization chamber is (0.98±0.05). It is unlikely that the lower limit of the chamber correction factor determined using the ice calorimeter is valid as there is no other work to support a chamber correction factor that is less than unity. This agrees with the value of k_{ch} given in chapter 3 of this thesis and that given by Ma [84] within the stated uncertainties.

7.1 FUTURE WORK

For ice calorimetry to be a useful dosimetric tool the uncertainties associated with the measured absorbed dose must be reduced. There are three main sources of uncertainty, the calibration of the thermistor in ice, the interpretation of the temperature rise from the calorimetry measurements and the specific heat capacity of ice. The calibration of the thermistor in ice could be improved if a properly designed temperature enclosure were employed. Unfortunately the temperature bath used in this thesis was dependent on the room temperature. For the irradiations this was not critical as the exposure rooms at NPL are temperature controlled but for the calibration of the thermistor a temperature controlled room was not

available. The second source of uncertainty is modelling the heat flow in ice that is necessary due to the high diffusivity of ice. A solution may be to construct an ice calorimeter that has a thermally isolated core similar to the primary standard graphite calorimeter. The final source of uncertainty is associated with the specific heat capacity of ice. It is recommended that a full investigation of the measurement of the specific heat capacity of ice at the operating temperature of the calorimeter be conducted.

An accurate ice calorimeter could solve many questions in megavoltage photon dosimetry; such as the conversion from absorbed dose in graphite to water, the value of W/e and the conversion from air kerma measured using cavity chambers to absorbed dose to water.

8. REFERENCES.

1 **DEPARTMENT OF HEALTH,** Summary of radiotherapy machine activity, England, Financial year 1992-93, Prepared by the Government Statistical Service.

2 **KLEVENHAGEN S.C, AUKETT R.J, BURNS J.E, HARRISON R.M, KNIGHT R.T, NAHUM A.E AND ROSSER K.E,** Report of the IPSM working party on low and medium energy X-ray dosimetry, Phys. Med. Biol.,**36**,1027-1038, 1991.

3 **ICRU Report 23,** Measurement of absorbed dose in a phantom irradiated by a single beam of X or gamma rays. International Commission on Radiation Units and Measurements, Bethesda, 1973.

4 **IAEA TRS 277,** Absorbed dose determination in photon and electron beams. Technical Reports Series 277, International Atomic Energy Agency, Vienna, 1987.

5 **IAEA,** Review of data and methods recommended in the International code of practice: IAEA technical report series number 277 absorbed dose determination in photon and electron beams, Proceedings of a consultants meeting organized by the IAEA, 8-11 December 1992.

6 **CCEMRI,** Effect of a change in stopping power values on the W-value recommended by ICRU for electrons in dry air, Report of the CCEMRI(1), 85-8 (BIPM Sevres), 1985.

7 **LIDEN K. V. H.,** Errors introduced by finite size of ion chambers in depth-dose measurements, (Proc. Int. Conf. Vienna, 1960), IAEA, Vienna 1961, 161-172.

8 **HARRISON R.M.,** Visual demonstration of the displacement effect of an ionization chamber within a phantom, at low X-ray energies (<150 keV), Phys. Med. Biol., 1993, **38,** 1329-1334.

9 **RAKOW A. AND WILL W.,** Zur Messung der Standardionendosis in Festen und Flüssigen Medien bei Röntgen- und Gammastrahlung mit Energien zwischen 50 keV und 3 MeV, Strahlentherapie, **141,** 332-335, 1971.

10 **ZOETELIEF J., ENGLES A. C. and BROERSE J. J.** Displacement corrections for spherical ion chambers in phantoms irradiated with neutron and photon beams. Proceedings of an International Symposium on Dosimetry and Radiotherapy, Paris, 1980, IAEA, Vienna, 1981, 125-138.

11 **MA C.** Monte Carlo simulation of dosimeter response using transputers. Phd thesis of University of London, U.K., 1991.

12 **SEUNTJENS J. ,THIERENS H. AND SCHNEIDER U.,** Correction factors for a cylindrical ionization chamber used in medium energy X-ray beams. Phys Med. Biol., 1993, **38,** 1-27.

13 **RAKOW A. AND WILL W.,** Zur Messung der Standardionendosis in Festen und Flüssigen Medien bei Röntgen- und Gammastrahlung mit Energien zwischen 50 keV und 3 MeV, Strahlentherapie, **133,** 354-360, 1967.

14 **MATTSON O.,** Comparison of water calorimetry and ionization chamber dosimetry in 100 and 200 kV X-rays beams, Report of the CCEMRI (1)/85-15 (BIPM, Sevres), 1985.

15 **KUBO H.,** Water calorimetric determination of absorbed dose by 280 kVp orthovoltage x-rays. Radiotherapy and Oncology 4, 1985, 275-281.

16 **SCHNEIDER U., GROSSWENDT B. AND KRAMER H.M.,** Perturbation correction factor for X-rays between 70 and 280 kV, (IAEA-SM-298/34, Proc. Int. Conf. Vienna 1987), IAEA, Vienna, 1988, 141-149, 1988.

17 **BURNS J. E. AND PRITCHARD D. H.,** Effects of non air-equivalence of NPL secondary standard therapy level ionization chamber, NPL Report, Rad. Sci., 40, 1977.

18 **CCEMRI** Correction de Humidité, Report of the CCEMRI (1), 6, (BIPM Sevres), 1977.

19 **BURNS J. E. AND ROSSER K. E.,** Saturation correction for the NE 2560/1 dosemeter in photon dosimetry, Phys. Med. Biol., 1990, **35**, 687-93.

20 **MARSH A.R.S AND MORETTI C.J,** Comparison of exposure standards for medium energy x radiation using a transfer instrument, CCEMRI(1)/83-14, 1983.

21 **BERNARD G.P., ASTON, G.H., MARSH, A.R.S AND REDDING, K,** On the Congruity of N.P.L. Exposure Standards, Phys. Med. Biol., 1964, **9**, 333-343.

22 **SHIPLEY D.R.,** Private communication.

23 **BURNS J. E.,** Private communication. 1991.

24 **Ma C-M AND NAHUM A.E.,** Monte Carlo calculated stem effect corrections for NE2561 and NE2571 chambers in medium-energy X-ray beams, Phys. Med. Biol., 1995, **40**,63-72.

25 **IPSM 1990,** Code of practice for high-energy photon therapy based on the NPL absorbed dose calibration service, Phys. Med. Biol., 1990, **35,** 1355-1360.

26 **CUNNINGHAM J. R. AND SONTAG M. R.,** Displacement corrections used in absorbed dose determination. Med. Phys., **13,** 1980, 672-6.

27 **SEUNTJENS J., THIERENS H., VAN DER PLAETSEN A. and SEGAERT,O.** Determination of the absorbed dose to water with ionization chambers calibrated in free air for medium energy X-rays. *Phys. Med. Biol.*,1988, **33,** 1171-1185.

28 **ICRU Report 10b,** Physical aspects of irradiation: recommendations of the ICRU, (Bethesda Md: International Commission on Radiation Units and Measurements), 1964.

29 **SCHNEIDER U,** Kalibrierung von therapiedosimetern im phantom für roentgenstrahlung, Medizinische Physik, 143-148/B6, 1981.

30 **HUBBELL J. H.** Photon mass attenuation and energy absorption coefficients from 1 keV to 20 MeV. Int. J. Radiat. Isot., 1982, **33** 1269-1290.

31 **BERGER M.,** The X- or Gamma-Ray Energy Absorption or Transfer Coefficient: Tabulations and Discussion', Rad. Res. 15 1-29, 1961.

32 **KNIGHT R. T. AND NAHUM A. E.,** Depth and field size dependence of ratios of mass energy absorption coefficients, water-to-air, for kV X-ray dosimetry, Proc. doc. of IAEA symposium on measurement assurance in dosimetry, May 1993, IAEA-SM-330/17.

33 **DUANE S.,** Stripping program. private communication, 1991.

34 **BIRCH R. and MARSHALL M.,** Computation of Bremsstrahlung X-ray

spectra and comparison with spectra measured with a Ge(Li) detector. Phys. Med. Biol., 1979, **24**, 505-517.

35 **NELSON R. W., HIRAYAMA H. and ROGERS D. W. O.**, The EGS4 code system. Stanford Linear Accelerator Center Report SLAC-265, 1985.

36 **CHILTON A. B.**, A note on the fluence concept. Health Physics, 1978, **34**, 715-716.

37 **DUANE S.**, Private communication, 1990.

38 **HARRISON R.M**, Central-axis depth-dose data for diagnostic radiology, Phys. Med. Biol. **26**, 657-670, 1981.

39 **CLARKSON J.R AND MAYNEORD W.V**, The 'quality' of high-voltage radiations. part1 1, BJR **12**, 168-180, 1939.

40 **BJR SUPPLEMENT 17**, Central axis depth dose data for use in radiotherapy, BJR 17, 1983.

41 **DOMEN S.R AND LAMPERTI P.A**, A heat -loss-compensated calorimeter: Theory, Design and Performance, J. Res. Nat. Bur. Stds., **78A**, 595-610, 1974.

42 **DuSAUTOY, A.R**, UK photon-beam primary standard calorimeter, Proceedings of the NPL calorimetry workshop, 12-14 October 1994.

43 **LEITNER, A AND WITZANI, J**, The realization of the unit of absorbed dose at the BEV, Proceedings of the NPL calorimetry workshop, 12-14 October 1994.

44 **GRIMBERGEN, T.W.M**, Changes of the electrical calibration factor observed

for the NMi graphite calorimeter, Proceedings of the NPL calorimetry workshop, 12-14 October 1994.

45 **OWEN B AND DuSAUTOY A.R,** NPL absorbed dose graphite calorimeter correction for the effect of the gaps around the core, NPL Report RSA (EXT)12, National Physical Laboratory, Teddington, Middlesex, TW11

OLW, 1990.

46 **BURNS J.E,** Absorbed dose calibrations in high-energy photon beams at the National Physical Laboratory: conversion procedure, Phys. Med. Biol., **39,** 1555-1575, 1994.

47 **TOIVONEN M., JARVINEN H., BERLYAND V. A., BREGADZE Y.I., AND MASLYAEV P.R.,** Calorimeters for absorbed dose standards or reference dosimeters for radiotherapy: Comparison with other methods, Proceedings of the NPL calorimetry workshop, 12-14 October 1994.

48 **KUBO H,** Estimate of the thermal diffusion from a polystyrene-water calorimeter detector to surrounding water during irradiation, Phys. Med. Biol., **30,** 785-798, 1985.

49 **DOMEN S.R.,** An absorbed dose water calorimeter: theory, design and performance, J. Res. Nat. Bur. Std., **87,** 211-235, 1982.

50 **SHULTZ R.J, HUQ M.S, VENKATARAMANAN N and MOTAKABBIR K.A,** A comparison of ionization-chamber and water-calorimeter dosimetry for high energy x rays, Med. Phys. **18,** 1229-1233, 1991.

51 **ROSS C.K, KLASSEN N.V, SHORTT K.R AND SMITH G.D,** A direct comparison of water calorimetry and Fricke dosimetry, Phys. Med. Biol. **34,** 23-42, 1989.

52 **NATH R and ROTHMAN A,** A model of heat production and transport in a water calorimeter, Med. Phys. **15** 370-374, 1988.

53 **NORMAND C and POMEAU Y,** Convection instability: A physicist's approach, Rev. Mod. Phys. **49** 581-624, 1977.

54 **DOMEN S.R,** A sealed water calorimeter for measuring absorbed dose to water, J. Res. N.I.S.T, **99**, 121-141,1994.

55 **ROOS M.,** The current status of water absorbed dose calorimetry in the PTB, Proceedings of a workshop held at the National Research Council of Canada in Ottawa, 9-15, 1988.

56 **ROSS C.K, KLASSEN N.V AND SMITH G.D,** The effect of various dissolved gases on the heat defect of water, Med. Phys. **11** 653-658, 1984.

57 **ROSS C.K, KLASSEN N.V, SHORTT K.R AND SMITH G.D,** Water calorimetry with emphasis on the heat defect, Proceedings of a workshop held at the National Research Council of Canada in Ottawa, 69-75, 1988.

58 **FLETCHER J.W,** Radiation chemistry of water at low dose rates with emphasis on the energy balance: A computer study, Atomic Energy of Canada Ltd. Document No. AECL-7834, 1982.

59 **KLASSEN N.V AND ROSS C.K,** Absorbed dose calorimetry using various aqueous solutions, Radiat. Phys. Chem. **38** 95-104, 1991.

60 **SELBACH H.J, HOHLFELD K. and KRAMER H.M.,** An experimental method for measuring the heat defect of water using total absorption of soft X-rays, Metrologia, **29**, 341-347, 1992.

61 **ROOS M, GROSSWENDT B AND HOHLFELD K,** An experimental

method for determining the heat defect of water using total absorption of high-energy electrons, Metrologia, **29**, 59-65, 1992.

62 **PALMANS H AND SEUNTJENS J,** Construction, correction factors and relative heat defect of a high purity, 4°C water calorimeter for absorbed dose determinations in high energy photon beams, Proceedings of the NPL calorimetry workshop, 12-14 October 1994.

63 **KLASSEN N.V, ROSS C.K, SHORTT K.R AND SMITH G.D,** The chemical heat defect of water, Proceedings of a workshop held at the National Research Council of Canada in Ottawa, 55-59, 1988.

64 **DRAGANIC LG AND DRAGANIC Z.D,** The radiation chemistry of Water, Academic Press, 1971.

65 **BJARGBAKKE E, SEHESTED K, LANG RASMUSSEN O AND CHRISTENSTENSEN H,** Input files for computer simulation of water radiolysis, Risø-M-2430, 1984.

66 **MOZUMDER A AND MAGEE J.L,** Model of tracks of ionizing radiations for radical reaction mechanisms, Rad. Res., **28**, 203-214, 1966.

67 **ICRU Report 16,** Linear energy transfer, International Commission on Radiation units and measurements, 1970.

68 **YAMAGUCHI,** A spur model applied to estimate yields of species in water irradiated by monoenergetic photons 50 eV - 2 MeV, Radiat. Phys. Chem. **34**, 801-807, 1989.

69 **KLASSEN N. V. AND ROSS C. K.,** The radiation chemistry of water at high LET, Proceedings of a workshop held at the National Research Council of Canada in Ottawa, 95-97, 1988.

70 **KUBO H and BROWN D.E,** Calorimeter dose determination by direct voltage measurements on a Wheatstone-type bridge circuit, Phys. Med. Biol. **29**, 885-889, 1984.

71 **BRYNJOLFSSON A AND HOLM N.W,** Calorimetric measurements of γ-rays and calibration of ferrous sulphate radiation dosimeter, Metrology of radionuclides, Proceedings of a symposium organized by the International Atomic Energy Agency, Vienna, 419-422, 1959.

72 **HOBBS P. V.,** Ice Physics, Clarendon Press, Oxford , 1974.

73 **FRANKS F,** Water a comprehensive treatise, volume 1, The physics and physical chemistry of water, Plenum Press, 1972.

74 **FLETCHER N.H,** The chemical physics of ice, Cambridge University press, 1970.

75 **KLASSEN N.V,** The radiolysis of ice near 0 °C and the heat defect, in preparation, 1995.

76 **ELLIS S.C.,** The Dissemination of absorbed dose standards by chemical dosimetry, mechanism and use of the Fricke dosemeter, Ionizing Radiation Metrology by Casnati, 163-179, 1974.

77 **INTERNATIONAL TEMPERATURE SCALE OF 1990,** BIPM Com. Cons. Thermométrie, **16,** Document 2, 1987.

78 **DUANE S,** private communication, 1994.

79 **KAYE G.W.C AND LABY T.H,** Tables of Physical and Chemical constants, 14th edition, Longman 1973.

80 **ROSSER K.E, OWEN B, DuSAUTOY A.R, PRITCHARD D.H, STOKER I, AND BREND C.J,** The NPL absorbed dose to water calibration service for high-energy photons, Proc. of a symp. on Measurement Assurance in Dosimetry, Vienna IAEA-SM-330/35, 1993.

81 **STOKER I AND DuSAUTOY A.R,** The measuring assembly for the NPL Primary standard absorbed dose graphite calorimeter at therapy levels, NPL report RSA (EXT)23, NPL Teddington, UK, 1991.

82 **ANGLISS R. F,** The electrical calibration of a Nuclear Enterprises Ltd. Type 2560 measuring assembly, NPL report RSA(EXT)56, NPL Teddington, UK, 1995.

83 **GIAUQUE W. F AND STOUT J. W,** The entropy of water and the third law of thermodynamics. The heat capacity of ice from 15 to 273 °K. Journal of the American chemical society, **38**, 1144-1150, 1936.

84 **MA C-M AND NAHUM A. E,** Calculations of ion chamber displacement effect corrections for medium-energy X-ray dosimetry, Phys. Med. Biol., **40**, 45-62, 1995.

85 **IPSM,** Code of practice for the determination of absorbed dose for X-rays below 300 kV generating potential (0.035 mmAl to 4 mmCu HVL, 10 - 300 kV generating potential), to be published.

86 **EVANS R.D.** The Atomic Nucleus, McGraw Hill, 1955.

87 **ICRU Report 19.** Radiation Quantities and Units, International Commission on Radiation Units and Measurements, Bethesda, 1971.

88 **WAGMAN, EVANS, PARKER, SCHUMM, HARLOW, BAILEY, CHURNEY AND NUTTALL,** The NBS tables of chemical thermodynamic

properties, J. Phys. Chem. Ref. Data **11** Suppl. 2. 1982.

89 **CARSLAW H. S AND JAEGER J. C,** Conduction of heat in solids, second edition, Clarendon Press, Oxford, 1989.

APPENDIX 1

MEDIUM ENERGY X-RAY QUALITIES AT NPL

Generating Potential (kV)	Half Value Layer (mmA1)	(mmCu)	Added filters (mm)
(a) Inherent filtration 2.5 mmBe + 4.8 mm Perspex			
100	4.0	0.15	4.4 Al
105	5.0	0.20	0.10 Cu + 1.0 Al
135	8.8	0.50	0.27 Cu + 1.0 Al
(b) Inherent filtration 4 mmA1 equivalent + 4.8 mm Perspex			
180	12.3	1.0	0.42 Cu + 1.0 Al
220	16.1	2.0	1.20 Cu + 1.0 Al
280	20.0	4.0	1.4 Sn + 0.25 Cu

APPENDIX 2

PHYSICS OF MEDIUM ENERGY X-RAYS.

A2.1 INTERACTIONS OF MEDIUM ENERGY X-RAYS WITH MATTER.

Table A2.1, list the possible processes by which the electromagnetic field of a photon can interact with matter as suggested by Evans [86].

TABLE A2.1 POSSIBLE INTERACTIONS OF ELECTROMAGNETIC RADIATION WITH MATTER.

TYPE OF INTERACTION	EFFECTS OF INTERACTION
1. Interaction with atomic electrons. 2. Interaction with nucleons. 3. Interaction with the electric field surrounding nuclei or electrons. 4. Interaction with the meson field surrounding nucleons.	(a) Complete absorption. (b) Elastic scattering (coherent). (c) Inelastic scattering (incoherent).

There are twelve ways of combining columns 1 and 2, so in theory there are twelve different ways in which photons can be absorbed or scattered by matter. In practice for radiation dosimetry there are three main interactions; photoelectric effect (1a), Compton effect (1c) and pair production (3c). For pair production to occur the X-ray energy must be greater then 1.02 MeV, therefore pair production is nonexistent over the medium energy X-ray range and will be ignored in this thesis. A minor effect for medium energy X-rays is Rayleigh scatter (1b). In this process the incident photon collides with an electron that is sufficiently tightly bound to the atom for the whole atom to absorb the recoil. The energy transfer to the atom is negligible and the photon is scattered without loss of energy. In most cases of radiological interest Rayleigh scattering is excluded because it does not cause energy to be absorbed.

A2.2 RADIATION QUANTITIES.

A2.2.1 FLUENCE.

A radiation source will give rise to a radiation field. Within this field there will be a fluence (Φ) of particles defined by the International Commission on Radiation Units and Measurements [87] as:

$$\Phi = \frac{dN}{da} \tag{22}$$

where

dN is the number of particles incident on a sphere of cross-sectional area da. The units of fluence are m^{-2}.

A2.2.2 ENERGY FLUENCE.

Consideration may be given to the energy carried by the particles rather than the particles themselves. The energy fluence (Ψ) is:

$$\Psi = \frac{dR}{da} \tag{23}$$

where

dR is the radiant energy entering a sphere of cross-sectional area da. The unit of energy fluence is Jm^{-2}.

A2.2.3 MASS ENERGY TRANSFER COEFFICIENT.

The mass energy transfer coefficient (μ_{tr}/ρ) of a material for indirectly ionizing particles of specified energy is the quotient of dE_{tr}/E by ρdl. Where dE_{tr}/E is the fraction of incident particle energy (excluding rest energies) transferred to kinetic energy of charged particles, by interactions traversing a distance dl in a medium of density ρ.

$$\frac{\mu_{tr}}{\rho} = \frac{1}{\rho E}\frac{dE_{tr}}{dl} \tag{24}$$

A2.2.4 MASS ENERGY ABSORPTION COEFFICIENT.

The mass energy absorption coefficient (μ_{en}/ρ) of a material for indirectly ionizing particles of specified energy is the product of the mass energy transfer coefficient for that energy and (1-g), where g is the fraction of the energy of secondary charged particles lost to bremsstrahlung in the material.

$$\frac{\mu_{en}}{\rho} = \frac{\mu_{tr}(1-g)}{\rho} \qquad (25)$$

A2.2.5 ABSORBED DOSE AND AIR KERMA.

As radiation passes through an absorbing medium it interacts in two stages. Firstly the energy of the indirectly ionizing photons is transformed to kinetic energy of electrons. Secondly these directly ionizing electrons are slowed down and deposit their energy in the medium. The second step is of interest in radiotherapy and radiobiology as energy is absorbed. The first step is described by the quantity kerma (kinetic energy released per unit mass) whereas the second step is described by the quantity absorbed dose.

The energy transfer of kerma takes place at a point, but the subsequent imparting of energy to matter that gives rise to the absorbed dose is spread over distances determined by the ranges of the charged particles.

A2.2.5.1 KERMA.

Kerma (K) is defined by ICRU (International Commission on Radiation Units) [87] as the quotient dE_{tr} by dm, where dE_{tr} is the sum of the initial kinetic energies of all charged particles liberated by indirectly ionizing particles in a volume element of the specified material and dm is the mass of the matter in that volume element.

$$K = \frac{dE_{tr}}{dm} \qquad (26)$$

The kinetic energy of an electron may be spent in two ways:

(1) Coulomb-force interactions with atomic electrons of the absorbing material. These are called collision (c) interactions.

(2) Radiative (r) interactions with the Coulomb force field of atomic nuclei, in which X-ray photons (bremsstrahlung or breaking radiation) are emitted as the electron decelerates.

Since dE_{tr} is the sum of the initial energies of the charged particles liberated by indirectly ionizing particles, Kerma (K) includes both interactions. Hence:

$$K = K_c + K_r \tag{27}$$

where:

K_c is the collision kerma,

K_r is the kerma due to radiative interactions.

It follows that for a given monoenergetic radiation beam Kerma can be written:

$$K = \psi \frac{\mu_{tr}}{\rho} \tag{28}$$

A2.2.5.2 ABSORBED DOSE.

Absorbed dose (D) is defined by ICRU [87] as the quotient of $d\bar{\epsilon}$ by dm. Where $d\bar{\epsilon}$ is the mean energy imparted by ionizing radiation to matter in a volume element and dm is the mass of the matter in that volume element.

$$D = \frac{d\bar{\epsilon}}{dm} \tag{29}$$

The energy imparted by ionizing radiation to matter in a volume is:

$$\epsilon = \Sigma\epsilon_I - \Sigma\epsilon_{ex} + \Sigma Q \tag{30}$$

where:

$\Sigma\epsilon_I$ is the sum of the energies (excluding rest energies) of all those directly and

indirectly ionizing particles that have entered the volume,

$\Sigma\epsilon_{ex}$ is the sum of the energies (excluding rest energies) of all those directly and indirectly ionizing particles that have left the volume,

ΣQ is the sum of all the energies released, minus the sum of all the energies expended, in any transformations of nuclei and elementary particles that have occurred within the volume.

A2.3 DETERMINATION OF ABSORBED DOSE TO WATER USING MEDIUM ENERGY X-RAYS.

For medium energy X-rays the collision kerma in air K_{air} can be measured using a calibrated ionization chamber by:

$$K_{air} = M_{air}\, N_K \qquad (31)$$

where

M_{air} is the reading of the ionization chamber when it is used in air corrected to the same ambient conditions as the calibration factor,

N_K is the air kerma calibration factor for the chamber for standard ambient conditions and for the radiation quality of the incident beam in air.

If the chamber is placed at a depth in water, the air kerma in water $(K_{air})_{water}$ is given by:

$$(K_{air})_{water} = M_{z=2}\, N_K\, k_{ch} \qquad (32)$$

where

$M_{Z=2}$ is the reading of the ionization chamber when it is used at 2 cm deep in water corrected to the same ambient conditions as the calibration factor,

k_{ch} allows for the change in the chamber response when it is calibrated in air to when it is used at a depth in water.

In this thesis

$$k_{ch} = k_{\alpha}\, k_{st}\, p_{rep}\, k_{sleeve} \qquad (33)$$

where:

k_{α} accounts for angular and energy dependance on the response of the chamber in water compared to when the chamber is calibrated in air,

k_{st} accounts for the influence of the stem on the response of the chamber in water compared to when the chamber is calibrated in air,

p_{rep} accounts for the replacement of the water by the cavity and wall of the chamber,

k_{sleeve} accounts for effect of the waterproof sleeve on the response of the chamber in water compared to when the chamber is calibrated in air,

The next step is to convert the air kerma in water to the water kerma in water by:

$$K_{water} = (K_{air})_{water} \left(\frac{\bar{\mu}_{en}}{\rho} \right)_{w,a} \qquad (34)$$

where:

$(\bar{\mu}_{en}/\rho)_{w,a}$ is the ratio of mass energy absorption coefficients of water to air.

Now

$$D_w = K_{water} \qquad (35)$$

Assuming:

(a) Bremsstrahlung production is negligible. Now the radiative kerma is zero and the total kerma is equal to the collision kerma. This is the case when using medium energy X-rays in low Z-materials.

(b) Charge particle equilibrium exists.

Combining equations 32, 34 and 35 gives:

$$D_w = M_{z=2}\, N_K \left(\frac{\bar{\mu}_{en}}{\rho} \right)_{w,a} k_{ch} \qquad (36)$$

APPENDIX 3

PARAMETERS USED TO CALCULATE THE HEAT DEFECT

A3.1 Initial Concentrations (mol/dm^3) [65]

$H_2O = 55.6$ $OH^- = 1 \times 10^{-7}$ $H^+ = 1 \times 10^{-7}$

A3.2 G-values (molecules/100 eV) for ^{60}Co at room temperature. [65]

$OH = 2.67$	$e^-_{aq} = 2.66$	$H = 0.55$	$H_2 = 0.45$
$H_2O_2 = 0.72$	$H^+ = 2.76$	$OH^- = 0.1$	$H_2O = -6.87$

G-values were derived so as they obeyed the laws of conservation of mass and charge.

A3.3 Water radiolysis equations and rate constants. [58]

REACTION		RATE CONSTANTS ($L.mol^{-1}.s^{-1}$)
RE1:	$OH + OH \rightarrow H_2O_2$	6×10^9
RE2:	$OH + e^-_{aq} \rightarrow OH^- + H_2O$	2.5×10^{10}
RE3:	$OH + H \rightarrow H_2O$	2.5×10^{10}
RE4:	$OH + O^- \rightarrow HO_2^-$	1.8×10^{10}
RE5:	$OH + HO_2 \rightarrow H_2O_3$	7.9×10^9
RE6:	$OH + O_2^- \rightarrow OH^- + O_2$	1×10^{10}
RE7:	$OH + O_3^- \rightarrow O_3 + OH^-$	2.5×10^9
RE8:	$OH + O_3^- \rightarrow HO_2 + O_2^-$	6×10^9
RE9:	$OH + H_2O_2 \rightarrow H_2O + O_2^- + H^+$	2.7×10^7
RE10:	$OH + HO_2^- \rightarrow H_2O + O_2^-$	7.5×10^9
RE11:	$OH + OH^- \rightarrow O^- + H_2O$	1.4×10^{10}

RE12: $OH + H_2 \rightarrow H_2O + H$	4×10^7
RE13: $OH + O_3 \rightarrow O_2^- + O_2 + H^-$	1×10^8
RE14: $e^-_{aq} + e^-_{aq} \rightarrow 2OH^- + H_2$	3×10^9
RE15: $e^-_{aq} + H \rightarrow OH^- + H_2$	2×10^{10}
RE16: $e^-_{aq} + O^- \rightarrow 2OH^-$	1.5×10^{10}
RE17: $e^-_{aq} + O_2^- \rightarrow HO_2^- + OH^-$	1.2×10^{10}
RE18: $e^-_{aq} + H_2O_2 \rightarrow OH + OH^- + H_2O$	1.6×10^{10}
RE19: $e^-_{aq} + HO_2^- \rightarrow O^- + OH^- + H_2O$	3.5×10^9
RE20: $e^-_{aq} + H^+ \rightarrow H + H_2O$	2.2×10^{10}
RE21: $e^-_{aq} + O_2 \rightarrow O_2^- + H_2O$	2×10^{10}
RE22: $e^-_{aq} + O_3 \rightarrow O_3^- + H_2O$	3.6×10^{10}
RE23: $e^-_{aq} + N_2O \rightarrow O^- + N_2 + H_2O$	9×10^9
RE24: $H + H \rightarrow H_2$	1×10^{10}
RE25: $H + HO_2 \rightarrow H_2O_2$	2×10^{10}
RE26: $H + O_2^- \rightarrow HO_2^-$	2×10^{10}
RE27: $H + H_2O_2 \rightarrow OH + H_2O$	6×10^7
RE28: $H + OH^- \rightarrow e^-_{aq}$	1.5×10^7
RE29: $H + O_2 \rightarrow O_2^- + H^+$	2×10^{10}
RE30: $H + O^3 \rightarrow OH + O_2$	3.6×10^{10}
RE31: $H + O^- \rightarrow OH^-$	$2 \times 1O^{10}$
RE32: $O^- + O^- \rightarrow O_2^=$	9×10^8
RE33: $O^- + O_2^- \rightarrow O_3^=$	3.5×10^8
RE34: $O^- + O_3^- \rightarrow 2O_2^-$	3.5×10^8
RE35: $O^- + H_2O_2 \rightarrow O_2^- + H_2O$	5×10^8
RE36: $O^- + HO_2^- \rightarrow OH^- + O_2^-$	3.5×10^8
RE37: $O^- + H_2O \rightarrow OH + OH^-$	2×10^6
RE38: $O^- + O_2 \rightarrow O_3^-$	3.0×10^9
RE39: $O^- + H_2 \rightarrow OH^- + H$	2×10^8
RE40: $HO_2 \rightarrow O_2^- + H^+$	8×10^5
RE41: $HO_2 + HO_2 \rightarrow O_2 + H_2O_2$	7.5×10^5
RE42: $HO_2 + O_2^- \rightarrow O_2 + HO_2^-$	1×10^8
RE43: $O_2^- + H^+ \rightarrow HO_2$	5×10^{10}

RE44: $O_2^- + O_3 \rightarrow O_3^- + O_2$	1.5×10^9
RE45: $H_2O_3 \rightarrow O_2 + H_2O$	2.1
RE46: $O_3^- \rightarrow O^- + O_2$	3.3×10^3
RE47: $O_3^- + H^+ \rightarrow OH + O_2$	9×10^{10}
RE48: $H_2O_2 + OH^- \rightarrow HO_2^- + H_2O$	5×10^8
RE49: $HO_2^- + H_2O \rightarrow H_2O_2 + OH^-$	5.735×10^4
RE50: $HO_2^- + O_3 \rightarrow O_3^- + O_2^- + H^+$	3×10^6
RE51: $H_2O \rightarrow H^+ + OH^-$	2.599×10^{-5}
RE52: $H_2O + O_2^- \rightarrow HO_2^- + OH^-$	1×10^8
RE53: $H_2O + O_3^- \rightarrow O_2 + 2OH^-$	1×10^8
RE54: $H^+ + OH^- \rightarrow H_2O$	1.43×10^{11}

A3.4 Heats of formation [88]

Species	Heat of formation (kJ/mol)
H_2O_2	-191.17
OH^-	-229.994
H_2O	-285.83
O^-_2	-24.7
O_2	-11.7
H^+	0
H_2	-4.2
HO^-_2	-160.33

APPENDIX 4

CONDUCTION OF HEAT IN THE ICE CALORIMETER.

A4.1 INTRODUCTION.

The ice calorimeter described in this thesis works on the principle that an absorbed dose at a point can be derived from the measurement of the temperature profile at that point. This requires that the heat transport into and from the point of measurement is negligible and does not affect the measurement of the temperature rise at the point of interest. In practice the conduction of heat throughout the calorimeter is described by three effects. Firstly non-uniformity of the heat flow radially in the calorimeter, secondly the heat flow along the major axis of the calorimeter due to the non-uniformity of the depth dose profile. Finally the specific heat capacity of the materials in contact with the ice is less than that of the ice. Therefore, irradiation causes excess heat to be generated in the thermistor. The amount of excess heat is proportional to the mass of the material that should be made as small as possible. The heat flow calculations presented in this thesis were derived by Duane [78].

A4.2 GENERAL CONDUCTION.

The transfer of heat by conduction can by described by the Fourier equation [89].

$$\frac{d^2\theta}{dx^2} + \frac{d^2\theta}{dy^2} + \frac{d^2\theta}{dz^2} - \frac{1}{\alpha}\frac{d\theta}{dt} = \frac{A(x,y,z,t)}{K}$$

where:

θ is the temperature,

t is the time,

K is the thermal conductivity of the ice,

A(x,y,z,t) is the source function,

α is the thermal diffusivity of the ice at temperature θ.

where:

$$\alpha = \frac{K}{\rho \cdot c}$$

where:

ρ is the density of the ice,

c is the specific heat capacity of the ice.

A4.3 RADIAL AND AXIAL FLOW OF HEAT IN THE ICE CALORIMETER.

The ice calorimeter was designed with a diameter equal to the diameter of the medium energy X-ray beam at NPL. As the X-ray beam is approximately flat the heat flow radially is assumed to be negligible. The problem therefore reduces to a one dimensional heat flow problem along the major axis of the calorimeter. Irradiation of the ice calorimeter causes the ice to be heated non-uniformly due to the decreasing dose with depth. The shape of the depth dose profile determines the initial temperature profile and the evolution with time was calculated for the time of a calorimeter run.

The solution was calculated analytically by dividing the calorimeter into 22 discrete slabs, each 0.24 cm long. It was assumed that there was no flow of heat in the slab and that heat only flowed between the slabs. Where the flow of heat between two slabs (1,2) is:

$$\frac{d\theta}{dx} \propto \alpha(\theta_1 - \theta_2)$$

The results are shown in Figure A4.1, where it is assumed that the flow of heat from the edges of the calorimeter is negligible.

A4.4 THERMISTOR OVERSHOOT.

The thermistor used in this thesis is a small cylinder, approximately 3.18 mm long and 0.46 mm in diameter, with a pair of thin platinum wires entering one end of the cylinder. If measurements are to be accurate, the excess heat must be conducted rapidly away during irradiation or heat flow calculations should determine the amount of excess heat.

Information about the thermistors chemical composition is not known to enable a

quantitative heat flow calculation. There is also an added complication as the heat flow exhibits cylindrical symmetry for short times and changes to spherical symmetry as time progresses. The spherical geometry was modelled by dividing a sphere into 13 shells the inner sphere containing the thermistor. The sphere was uniformly heated except for excess heating near the inner shell. The cylindrical symmetry was modelled analytically.

Duane [78] found (see figure A4.2) that the rise in the excess heat due to thermistor overshoot can be characterized into three main sections. A linear rise immediately after the irradiation is started, a logarithmic rise follows and finally a constant term. This is mimicked when the beam is turned off.

A4.5 TOTAL CORRECTION DUE TO HEAT CONDUCTION.

The total correction due to heat conduction in the ice calorimeter was calculated by a fit of the model to the experimental data (see figure A4.3). The pre irradiation drift was taken to be linear, followed by a linear fit immediately after the beam is turned on and a logarithmic fit. This left a time dependent temperature profile in the ice at the depth of measurement. This was fit to the function calculated in section A4.3, multiplied by a factor that is the corrected temperature.

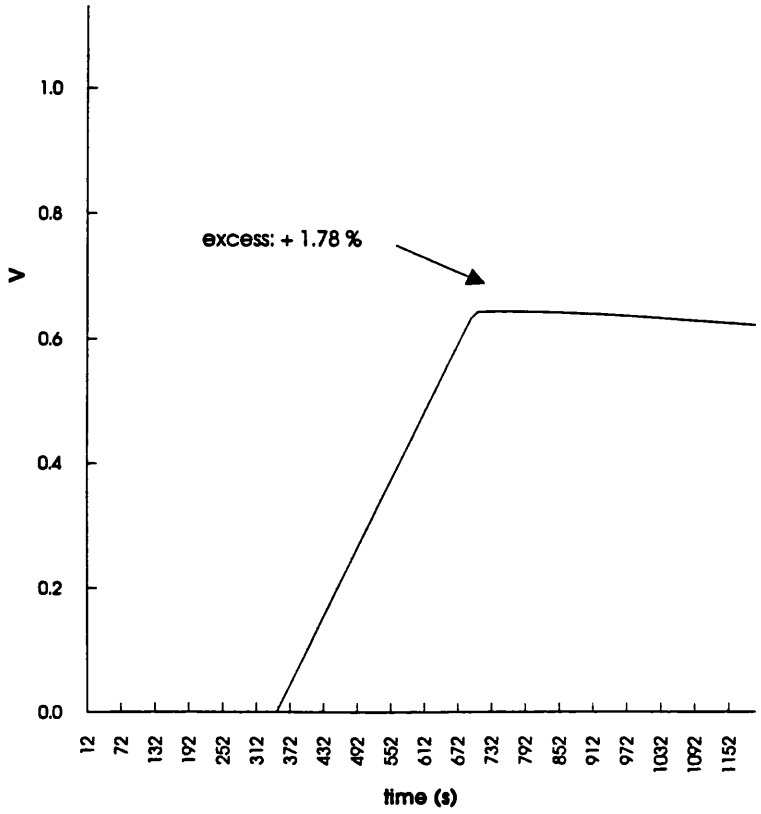

Figure A4.1 Temperature at 2 cm in water

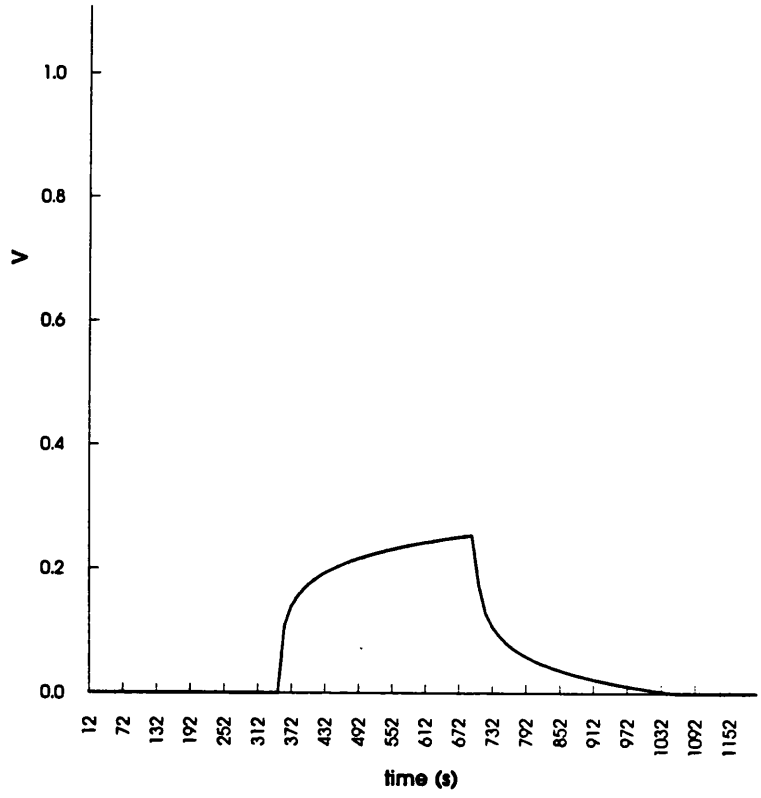

Figure A4.2 Thermistor overshoot.

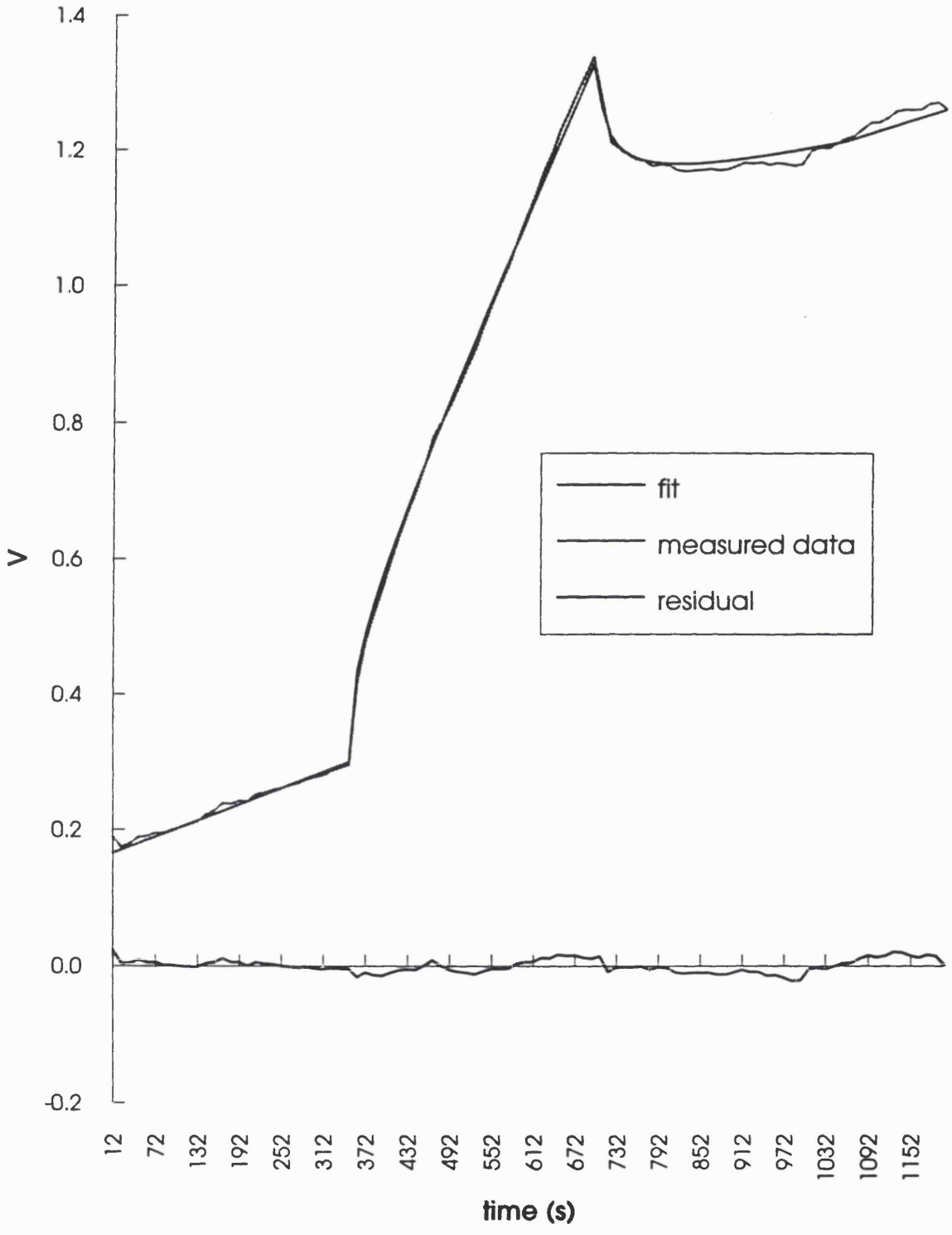

Figure A4.3 Comparison of the measured and modelled data.

ADDENDUM TO PHD THESIS ENTITLED ' MEASUREMENT OF ABSORBED DOSE TO WATER FOR MEDIUM ENERGY X-RAYS'

UNIVERSITY OF LONDON, MARCH 1996

KAREN ELIZABETH ROSSER

1. RECOMMENDED CHANGES TO ICRU REPORT 23 AND IAEA TRS 277.

1.1 In IAEA TRS 277, P_u is defined as the replacement correction only but the values quoted are for the chamber correction factor. IAEA should correctly define P_u to include all of the components of the chamber correction factor (see equation 2, page 17 of this thesis).

1.2 The values of P_u given in IAEA TRS 277 should not include values determined using the graphite extrapolation chamber until the difference between this method and other methods is understood.

1.3 In ICRU Report 23, the chamber should be calibrated in terms of air kerma instead of exposure.

1.4 In ICRU Report 23, the F-factor should be replaced with its constituent components, therefore the equation used to determine absorbed dose to water will become equation 36 on page 133 of this thesis.

1.5 In ICRU Report 23, the value of W/e should be updated and the values of $(\bar{\mu}_{en}/\rho)_{w,a}$ given in IAEA TRS 277 should be adopted.

1.6 In both codes, for medium energy X-ray dosimetry the depth at which the absorbed dose to water is determined in water should be reduced from 5 cm to 2 cm, to maximize the measured dose.

1.7 The chamber correction factor is dependant on chamber type, field size and depth in the phantom. Therefore, both codes should quote the chamber correction factor for all of the conditions and types of chambers in common use.

1.8 For atypically designed chambers the codes should recommend a method of determining the chamber correction factor based on a chamber with a known chamber correction factor as given in chapter 3 of this thesis.

1.9 In both codes the characteristics of the waterproof sleeve should be given such as those outlined in section 3.6.2 of this thesis.

1.10 To reduce the effect of the waterproof sleeve on the chamber correction factor the chambers should be calibrated in air in their waterproof sleeves. In this situation the calibration in terms of air kerma would only be valid for the chamber placed in its own unique sleeve.

1.11 It has been shown in this thesis that the use of HVL as a beam quality specifier is inadequate. For medium energy X-rays HVL should be replaced with an index that is dependent on the slope of the depth dose curve in water, such as the ratio of absorbed dose to water at 2 cm deep to that at 5 cm deep.

2. DESIRABLE FEATURES OF AN IONIZATION CHAMBER USED TO MEASURE ABSORBED DOSE TO WATER

For an air equivalent ionization chamber the desirable features are given in ICRU Report 23 (see page 24 of this thesis). Additional characteristics have become apparent in this thesis and are listed below.

2.1 The chamber should be watertight to eliminate the need for a waterproof sleeve.

2.2 To reduce k_{stem}, the diameter of the chamber stem should be as small as possible and the material used to manufacture the stem should have as low an atomic number as possible. Materials with atomic number greater than that of aluminum should not be used.

2.3 The components used to construct the ionization chamber should have as low an atomic number as possible. Materials with atomic number greater than that of aluminum should not be used.

2.4 The size of the chamber volume is a compromise between as small as possible to reduce p_{rep} and large enough to produce a measurable ionization current.

2.5 The shape of the chamber cavity is a compromise between a chamber with good spatial resolution such as a parallel plate chamber and a spherical chamber that will minimize k_{α}.

2.6 The wall of the chamber should be just thick enough to ensure electrons entering the cavity originate in the wall of the cavity and not in the surrounding medium, wall thicknesses greater than these should never be used.

2.7 Any material that results in radiation backscattered into the cavity should not be used near the chamber, such as the housing of the PTW Grenz chamber.

2.8 For chambers to exhibit a flat (within ±5%) energy response in air some method of compensation is required. Chambers without any compensation such as those used for electron dosimetry should not be used for medium energy X-ray dosimetry.

Ideally to minimize the replacement correction in water all of the components, i.e. stem, wall and cavity of the chamber should be constructed of water equivalent material. In this case the chamber could only be used over the medium energy X-ray range as it is unlikely that the material would be water equivalent over a large energy range. If the water equivalent chamber were used as recommended in the two codes then the chamber correction factor would be simplified to the product of k_u and a replacement correction in air, assuming that the chamber was spherical and watertight.

However the measurement of absorbed dose to water using an ionization chamber could be simplified further. If initially the air kerma at a point in space (say point p) was determined using a free air chamber. The water equivalent chamber should then be placed at 2 cm deep in a full scatter water phantom, with its effective point of measurement at point p. The water equivalent chamber would now be measuring air kerma in water directly and only $(\bar{\mu}_{en}/\rho)_{w,a}$ would be required to determine absorbed dose to water.